PHOTOEMISSION FROM BIASED METAL SURFACES: QUANTUM EFFICIENCY, LASER HEATING, DIELECTRIC COATINGS, AND QUANTUM PATHWAYS INTERFERENCE

By

Yang Zhou

A DISSERTATION

Submitted to
Michigan State University
in partial fulfillment of the requirements
for the degree of

Electrical Engineering – Doctor of Philosophy

2022

ABSTRACT

Electron emission from metal surfaces due to the illumination of laser fields is of great interest due to its broad applications ranging from electron sources to quantum information processing to attosecond physics. It also offers fundamental insights into electron dynamics and electronic band structures of materials. This thesis analytically studies the effects of laser (wavelength or frequency, and field strength) and cathode surface conditions (with or without dielectric coatings) on photoemission from biased metal surfaces, by exactly solving one-dimensional (1D) time-dependent Schrödinger equation. Our study provides better understanding of photoemission dynamics, laser heating effects on photoemission, and two-color laser coherent control of photoemission with a dc bias, and it is useful for the design of more stable and efficient emitters.

First, we study photoemission from a metal surface using an analytical quantum model. It is found that shorter wavelength lasers can induce more photoemission from electron initial energy levels further below the Fermi level and, therefore, yield larger quantum efficiency (QE). The dc field increases QE, but it is found to have a greater impact on lasers with wavelengths close to the threshold (i.e., the corresponding photon energy is the same as the cathode work function) than on shorter wavelength lasers. When the laser field increases, QE increases with the laser field strength in the longer laser wavelength range due to the increased contributions from multiphoton absorption processes. The quantum model is compared with classical three-step model, the Fowler–DuBridge model, and the Monte Carlo simulation based on the three-step model. Even though those models have very different settings and assumptions, it is found that the scaling of QE of our quantum model agrees well with other models for low intensity laser fields.

Next, we study photoemission from metal surfaces with laser wavelengths from 200 to 1200 nm (i.e., ultraviolet to near infrared). It is found that QE can be increased nonlinearly by the non-equilibrium electron heating produced by intense sub-picosecond laser pulses. This increase of QE due to laser heating is the strongest near laser wavelengths where the cathode work function is an integer multiple of the corresponding laser photon energy. The quantum model, with laser heating effects included, reproduces previous experimental results, which further validates our quantum model and the importance of laser heating.

We then present an exact analytical theory for field emission from dielectric coated cathode

surfaces, by solving the 1D Schrödinger equation with a double-triangular potential barrier introduced by the coating. The condition under which the emission current density from the coated cathode can be larger than the uncoated case is identified. Our quantum model is also compared with a modified Fowler-Nordheim equation for a double barrier, showing qualitatively good agreement.

We further extend the exact quantum model for electron emission from metal surfaces coated with an ultrathin dielectric to photoemission. It is also found that a flat metal surface with a dielectric coating can photoemit a larger current density than the uncoated case when the dielectric has smaller relative permittivity and larger electron affinity. Resonant peaks in the photoemission probability and emission current are observed as a function of dielectric thickness or electron affinity due to the quantum interference of electron waves inside the dielectric. Our model is compared with the effective single-barrier quantum model and modified Fowler–Nordheim equation, for both 1D flat cathodes and pyramid-shaped nanoemitters. While the three models show quantitatively good agreement in the optical field tunneling regime, the present model may be used to give a more accurate evaluation of photoemission from coated emitters in the multiphoton absorption regime.

Finally, we analyze the quantum pathways interference in two-color coherent control of photoemission using exact analytical solutions of the time-dependent Schrödinger equation. The theory includes all possible quantum pathways and their interference terms. It is found that increasing the intensity ratio of the second harmonic (2ω) laser to fundamental (ω) laser results in less contribution from the ω pathway (absorption of ω photons only) and more contribution from multicolor pathway (simultaneous absorption of both ω and 2ω photons) and 2ω pathway (absorption of 2ω photons only), and therefore stronger pathways interference and increased visibility larger than 95%. Increasing bias voltages shifts the dominant emission to processes with lower-order photon absorption, which sequentially decreases the interference between the ω and the 2ω pathways, and between single-color and multicolor pathways, leading to two peaks in the visibility as a function of dc field.

ACKNOWLEDGEMENTS

It would not be possible to write this thesis without the kind help and firm support from all the people around me. Here, I would like to express my sincere gratitude to them.

I would like to first thank my advisor Prof. Peng Zhang for his help, support, and guidance over the past four years. It would not be possible to have this thesis without his help and guidance. He has always been patient and careful with every detail. I can still remember when he pointed out a punctuation error in slides just at his first glance. He has always been there whenever I need help. His advice really helps for both my academic work and personal life. I really appreciate it.

I would also like to thank all the committee members, Prof. Verboncoeur, Prof. Baryshev, Prof. Fan, and Prof. Ruan for their valuable time and helpful guidance. Professor Verboncoeur's expertise in vast fields is always valuable to my research during my PhD study. He has provided me fruitful suggestions. Thanks to him for his question and comments at IVEC 2022 in Monterey, CA, which really eased my nervousness at that moment.

Due to the supportive group members, Dr. Yangyang Fu, Dr. De-Qi Wen, Dr. Asif Iqbal, Dr. Janez Krek, Dr. Sneha Banerjee, Dr. Yi Luo, Faisal and Ayush, I really enjoy the past four years in MSU. Thanks to Dr. Luo for helping me with my research and for helping me settle down when I first came to MSU. I would like to thank all the friends and people I met in work and life for their help and support. Thanks to Xiangkai Feng for helping me all the time, from preparing TOEFL and GRE, to everyday life when I first came to the US. Thanks for their accompany when I was in depression and anxiety in 2020.

Finally, I would like to thank my parents and sisters for their support and encouragement all the time, especially my mother, who is a kind, persistent, and hard-working woman. Their love and care have always motivated me to move forward.

TABLE OF CONTENTS

CHAPTER 1 INTRODUCTION

1.1 Background

Electron emission from metal surfaces due to the illumination of laser fields has received considerable attention due to its broad applications and has provided fundamental insights into electron dynamics and electronic band structures of materials [1]–[7]. The recent development of tailored ultra-short and intense waveform-controlled laser fields [8]–[10] and the advances in fabrication of nanostructures have enabled the characterization of photoemission processes on attosecond timescale and on nanometer spatial scale [7], [11]–[13], which makes the spatiotemporally controllable electron sources possible. Therefore, emerging applications, such as ultrafast electron microscopy [14]–[19], time-resolved scanning transmission electron microscopy [7], free electron lasers (FELs) [20]–[22], ultrafast electron diffraction [1], [6], [23], carrier-envelope detection [24], [25], and ultrafast light-wave driven nano-electronics [26]–[32], are accessible.

The underlying processes of photoemission from metal surfaces have been investigated extensively. Multiphoton photoemission, above-threshold photoemission, photo-assisted field emission, and optical field emission are identified [33]–[39]. Laser-matter interaction is strongly affected by the frequency or wavelength of the oscillating light fields [40]. As wavelengths λ range from ultraviolet (UV, λ<380 nm) to terahertz (THz), different dominant emission processes and excited electron dynamics are observed. Single-photon photoemission has been observed in the broad UV wavelength range for various metallic cathodes [41]–[44]. With higher illumination intensities, electrons can be emitted by sub-work function energy photons ($\hbar\omega < W$, with W work function of emitters). In this case, minimum n photons ($n = \langle W/\hbar\omega + 1\rangle$, with $\langle\ \ \rangle$ denoting the integer part) have to be absorbed simultaneously in order to excite an electron to escape the material. Nanostructured metallic emitters have enabled multiphoton photoemission, above-threshold photoemission, and optical field emission to occur at a relatively low incident laser intensity and high pulse repetition rates without damaging the emitter, due to significant enhancement of the laser electric field on the nanotip by the so-called lightning rod effect and surface plasmonic effects [36], [37], [45]–[47]. Hommelhoff *et al.* [45] experimentally demonstrated continuously tuning between the photofield emission (or photo-assisted field emission) and optical field emission from tungsten nanotips by varying the driving laser intensity with a wavelength centered at ~810 nm. Long-wavelength few-cycle laser pulses are a powerful

tool to control and manipulate electron dynamics from nanostructures on femtosecond and attosecond timescales and on an atomic spatial scale. It is common to find that the Keldysh parameter $\gamma < 1$ and therefore strong field regime can be reached at a relatively low laser intensity in long wavelength range, especially for emitters designed to be plasmon coupling with optical fields [37]. With laser wavelengths from 1 μm to 1.5 μm, Park *et al.* [48] observed the narrowing of the emission cone angle of the fastest electrons when laser intensity increases, which is ascribed to field-induced steering of sub-cycle electrons. Few-cycle midinfrared (up to 8 μm) laser pulses are applied to single plasmonic nanotips, and it is found that the electrons can escape the local field within a fraction of an optical half-cycle and electron quiver motion can be quenched [49]. Single-cycle terahertz pulses have also been demonstrated to have their capacity to control nanotip photoemission electron dynamics [50]–[52].

Incident lasers act not only as a photon source, but also as a heat source. Photoelectron emission processes are always accompanied by heating of the emitter surface to some extent due to high laser intensities. The heating effect pushes the Fermi tail of the electron distribution closer to the vacuum level. Therefore, thermally enhanced multiphoton photoemission, thermionic emission and photon-assisted thermionic emission can occur during the process [42], [53]–[57]. For shorter laser pulses (several picoseconds to a few hundreds of femtoseconds), the action of laser can also lead to nonequilibrium between electron and lattice systems, which was predicted theoretically and demonstrated experimentally [58]–[61]. For femtosecond lasers (<100 fs), the *e*-*e* collision is not fast enough to reach the internal thermalization during the laser pulse. Therefore, two-temperature model (TTM) is inadequate, and microscopic kinetic approach, e. g., Boltzmann's equation [62], [63] and nonequilibrium Green's-function theory [64], is required.

Properties of the cathode materials also influence the fundamental mechanisms of photoemission. Metal cathodes, antimonide cathodes, and NEA (negative electron affinity) cathodes are commonly used as photocathodes for various applications, and each type has their own strengths and weaknesses [65], [66]. Metals are relatively robust, easy to prepare, and less sensitive to vacuum conditions. The metallic cathodes can be more attractive if they are designed with plasmon coupling to the optical field, which greatly enhances the local field at the metal-vacuum interface [67]. The emerging capabilities of tailoring composition and electronic structure of materials enable us to utilize heterostructure architectures, quantum wells, and

superlattices which consists of nanoscale structures, to design and fabricate photocathodes to satisfy the stringent requirements of high quantum efficiency, high brightness, and low emittance [68], [69]. Artificial coatings, such as, graphene, nano-diamond, silicon dioxide, and zinc dioxides, are proposed to be fabricated on cathodes to provide protection and improve quantum efficiency [70]–[75]. The work function of emitter is significantly altered by thin oxide films [76]. A reduction of >1 eV in the work function relative to Ag is observed for MgO monolayers on Ag [77]. Both theory and experiments have shown that the quantum efficiency can be improved with coatings [47], [70], [71], [75], [78], [79]. The cathode surface can be contaminated due to the bombardment by ions and electrons or can be oxidized under poor vacuum conditions. These modified surface conditions also influence the photoemission processes.

In addition to novel nanostructured emitter tips, coherent lights consisting of a strong fundamental laser and a weak second harmonic, provide another essential tool to tune and control photoemission from nanotips. It was first applied in the study of electron dynamics of atoms and molecules [80]–[83]. The Hommelhoff team [84]–[88] reported their experiments on coherent control of photoemission from nanotips using two-color lasers. By varying the mixture ratio and sweeping the relative phase between those two fields, substantial modulation of photoemission current has been demonstrated, with a modulation depth or visibility of up to 97.5% [84]–[88]. In addition to the n-photon photoemission induced by respective lasers with $n = \langle W/\hbar\omega + 1\rangle$ for ω-laser or $n = \langle W/\hbar(2\omega) + 1\rangle$ for 2ω-laser, multicolor quantum pathways are also introduced, in which photons of different colors are simultaneously absorbed [85], [89], [90]. The strong modulation is attributed to the interferences among those pathways. By checking electron emission energy spectra, above-threshold photoemission from tungsten nanotip is observed [84], and the strong field regime is approached by applying strong few-cycle laser pulses with a nearfield intensity of ~4 TW/cm^2 to a gold needle tip [88]. As another tuning knob, dc electric field suppresses high frequency terms, resulting in a reduced visibility [86]. Luo and Zhang developed an analytical quantum model by exactly solving the time-dependent Schrödinger equation, which includes multiphoton photoemission, above-threshold photoemission, photo-assisted field emission, and dc or optical field emission [91]–[93]. The model has shown good agreement with experiments and demonstrated the potential in measurement of time-resolved photoelectron energy spectra.

1.2 Fundamentals of Photoelectron Emission from Metals

1.2.1 Photoelectron Emission Mechanisms

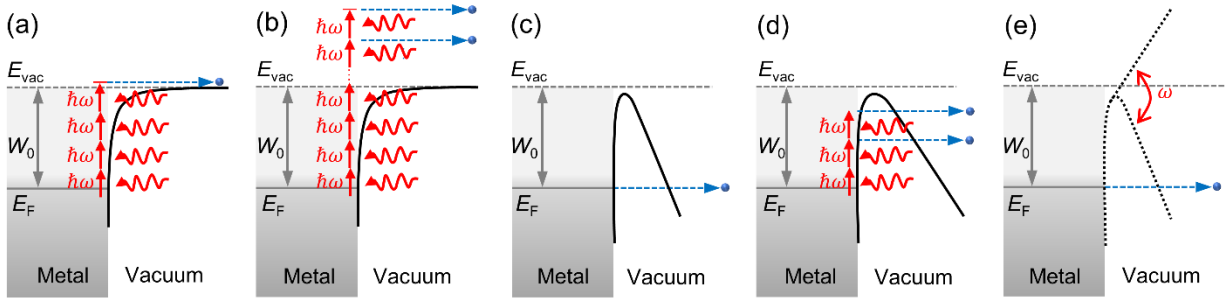

Figure 1.1 Mechanisms of photoemission from metal surfaces. (a) Multiphoton photoemission. An electron absorbs the minimum required number of photons to overcome the metal surface potential barrier to emit. (b) Above-threshold photoemission. An electron absorbs more than the minimum required number of photons to overcome potential barrier for photoemission. (c) Field emission. Direct tunneling of electrons through a narrowed potential barrier by dc field into vacuum. (d) Photo-assisted field emission. An electron is excited to a higher energy level by absorbing photons and tunnels through the narrowed potential barrier by dc field into vacuum. (e) Optical field emission. An electron tunnels through the periodically oscillating potential barrier induced by the strong laser field.

A. Multiphoton absorption and Above-threshold photoemission

In the multiphoton absorption process (see Fig. 1.1(a)), a single or several photons are absorbed, and the electron is elevated above the vacuum level. The minimum number n of photons required to overcome the potential barrier for electrons with initial energy at Fermi level is $\langle W/\hbar\omega + 1\rangle$, with $\langle\ \ \rangle$ denoting the integer part, W being the work function of the emitter, $\hbar$ being the reduced Planck constant, and ω being the angular frequency of the laser. The photoemission current in the multiphoton absorption regime follows a power scaling law [34], $J \propto I^n$ or $J \propto F_1^{2n}$, where I is the laser intensity and F_1 is the strength of the laser field perpendicular to the emitter surface [94]. Absorption of photons (with an energy smaller than work function of the emitter) is considered to occur simultaneously, and thus multiphoton absorption always requires relatively intense lasers. The above-threshold photoemission requires absorption of more than the minimum required number of photons (see Fig. 1(b)), which is characterized by a plateau in photoelectron energy spectra [33], [38]. The broadening of the spectra also signifies the back-propagation and rescattering of electrons [95], which has also been observed in atoms [96].

B. Field emission and Photo-assisted field emission

Field-induced emission exploits the quantum-mechanical tunneling process. Under a high

electrostatic field, the surface potential barrier of field emitters is bent down, electrons inside the emitter can tunnel through such a narrowed barrier into the vacuum, as shown in Fig. 1(c). Fowler and Nordheim first developed equations to predict the emission current by assuming the potential barrier under electric field as a triangular potential barrier [97]. The field emission current is found to depend on the dc field strength F and work function of the emitter W. Fowler-Nordheim (FN) equation takes the following form [97]–[99],

$$J = \frac{C_1(\beta F)^2}{W} \exp\left[-\frac{C_2 W^{\frac{3}{2}}}{\beta F}\right] \tag{1.1}$$

where $C_1 = 1.54 \times 10^{-6}$ A eV V^{-2}, $C_2 = 6.83 \times 10^{9}$ $\mathrm{eV}^{-3/2}\mathrm{V\,m}^{-1}$, W (in eV) is the work function of the emitter, β is the field enhancement factor, and F (in V/m) is the electric field strength.

Photo-assisted or laser-assisted electric field emission [45] is the process where electrons are first excited from their initial energy level to a higher energy level by absorbing photons, as shown in Fig. 1.1(d). The excited electrons see a much narrower potential barrier, and therefore, the tunneling probability is greatly improved.

C. Optical field emission

In the optical field emission or strong field tunneling regime (see Fig. 1(e)), the potential barrier is periodically narrowed down by the oscillating electric field of the laser such that electrons inside the metal can penetrate through the barrier in a fraction of optical half-cycle [49]. Therefore, a single electron beam with a duration of ~ half cycle of the incident laser can be generated, especially with the use of few-cycle, long-wavelength or low-frequency, and high-intensity laser pulses [50]. Optical field emission has been experimentally demonstrated for tungsten and gold nanotips [33], [45], [48], [100], [101], and tailored plasmonic nanostructures [36], [37], [46], [102].

D. Photo-assisted thermionic emission

Due to the incident laser intensity, photon-electron interaction processes are always accompanied by heating of the surface to some extent. The heating effect puts the tail of the electron distribution closer to the vacuum level. Electrons in the tail of this distribution can be emitted into the vacuum by absorbing one or multiple photons or directly through thermionic emission [53], [56], [57]. Photo-assisted thermionic emission and laser-induced thermionic

emission have strong dependence on the intensity and length of the laser pulses [58]. For the relative low laser intensity and long laser pulse, single temperature heat conduction equation can describe the heating process [103]. For laser pulses of several hundreds of femtoseconds to a few picoseconds, laser radiation may lead to nonequilibrium between electron and lattice systems, which was predicted theoretically and demonstrated experimentally [59]. For femtosecond laser pulses, laser heating effects may be negligible [45].

1.2.2 Keldysh Parameter

The Keldysh parameter γ is an indicator of transition from multiphoton absorption to optical field tunneling in photoemission. γ is estimated as the ratio of two time scales [104], [105],

$$\gamma = \frac{4\pi t_t}{T}, \tag{1.2}$$

where $T = 2\pi/\omega$ is the cycle of the optical field, and $t_t = l/v$ is the time of an electron with velocity $v = \sqrt{2W/m}$ tunneling through the potential barrier with a width l, W is the effective work function of the metal and m is the electron rest mass.

Multiphoton photoemission is characterized by $\gamma \gg 1$, while optical field emission is characterized by $\gamma \ll 1$. The exact transition point is difficult to determine, which is always accompanied by slope decrease in the plot of photoemission yield against laser intensity or field strength. The transition at $\gamma \approx 2$ was confirmed by the reduction of the nonlinear power order in the electron yield as a function of the incident laser pulse energy [101]. More discussion for the transition region between these two extremes is given as $1 < \gamma < n_0$ with $n_0 = \langle W/\hbar\omega + 1 \rangle$ [59].

1.3 Motivation and Organization of the Thesis

1.3.1 Motivation of the Thesis

As mentioned in Section 1.1, extensive studies on laser induced photoemission have been done over a broad range of wavelengths. Most studies use a single or several discrete laser wavelengths or a short range of laser wavelengths, which lacks a systematic analysis on the effects of laser wavelength and the accompanying laser heating effects on photoemission. Therefore, this thesis will first systematically investigate the photoemission current and quantum efficiency with a wide range of laser wavelength from 200 nm to 1200 nm, using a quantum model based on the exact solution of time-dependent Schrödinger equation, which is also

compared with classical models.

Coatings on cathodes have strong influences on electron emission. However, there is lack of systematic study on the parametric scaling of electron emission from coated cathode surfaces and comprehensive understanding of the interplay of various parameters. Thus, the second part of this thesis will focus on developing analytical quantum theory for electron emission from metal surfaces with dielectric coatings and using the model to investigate the effects of dielectric coatings on electron emission.

Two-color lasers and dc bias field can tune and control electron emission with great flexibility. Nevertheless, how the two-color lasers (fundamental and second harmonic laser fields, and their phase difference) and dc bias field influence the coherent control of photoemission is still not clearly understood. Therefore, the last part of this thesis will analyze the quantum pathway model using exact quantum theory for photoemission from biased metal surfaces under two-color lasers.

1.3.2 Organization of the Thesis

In this thesis, we develop analytical quantum models to study photoemission from metal surfaces with and without nanoscale dielectric coatings under a dc bias, by exactly solving time-dependent Schrödinger equation (TDSE). The model includes photoemission, field emission, and thermionic emission with laser heating effects considered. We validate the quantum model for photoemission from bare metal surfaces by comparing it with classical models, and we study the effects of laser wavelength and corresponding laser heating effects on photoemission quantum efficiency, the effects of dielectric coatings on both field emission and photoemission, and two-color laser coherent control of photoemission processes.

Chapter 2 presents a quantum model for photoemission from a metal surface due to the excitation of laser fields under a dc bias, by solving TDSE exactly. Quantum efficiency under various laser wavelengths ($\leq$ 300 nm, in UV) and dc fields ($\leq$ 0.1 V/nm) is studied. The model is compared with existing classical models, i.e., three-step model, Fowler-DuBridge model and three-step model based Monte Carlo simulation, for photoemission from both copper and gold metal surfaces.

Chapter 3 presents the study of photoemission from a metal surface with laser wavelengths from 200 nm to 1200 nm (i.e., ultraviolet (UV) to near infrared (NIR)), using the quantum model developed in Chapter 2. The dominant electron emission mechanism, from different multiphoton

emission processes to dc or optical field emission, under different combinations of laser field strength (or laser intensity), wavelength, and dc bias field, is investigated. The parametric dependence of the quantum efficiency (QE) is analyzed in detail. Laser heating is taken into consideration by using the two-temperature model, and its effects on photoemission are examined. The quantum model, with laser heating effects included, is also compared with previous experimental results with excellent agreement.

Chapter 4 presents an exact analytical theory for field emission from dielectric-coated cathode surfaces, by solving the 1D Schrödinger equation with a double-triangular potential barrier introduced by the coating. The effects of the cathode material (work function and Fermi energy), dielectric properties (dielectric constant, electron affinity and thickness), applied dc field strength, and cathode temperature are analyzed in detail. The quantum model is also compared with a modified double-barrier Fowler-Nordheim equation.

Chapter 5 presents an analytical quantum model for photoemission from metal surfaces coated with an ultrathin dielectric, by solving the 1D TDSE subject to an oscillating double-triangular potential barrier due to the combined dc and laser fields. The effects of dielectric properties (thickness, relative permittivity, and electron affinity), laser field strength, and dc field on photoemission are systematically investigated. The model is compared with the effective single-barrier quantum model and modified Fowler-Nordheim equation, for both 1D flat cathodes and pyramid-shaped nanoemitters.

Chapter 6 analyzes the quantum pathways interference in two-color coherent control of photoemission using exact analytical solutions of TDSE. The theory includes all possible quantum pathways and their interference terms. The effects of laser fields (the intensity mixture ratio of the second harmonic (2ω) to fundamental (ω) and their phase difference) and dc field on the weight of each pathway and the interference effects among them are analyzed in detail.

Chapter 7 gives a summary and an outlook for future works.

CHAPTER 2 AN ANALYTICAL QUANTUM MODEL FOR PHOTOEMISSION FROM METAL SURFACES

This chapter is based on the published journal paper "A quantum model for photoemission from metal surfaces and its comparison with the three-step model and Fowler–DuBridge model," *J. Appl. Phys.*, vol. 127, no. 16, p. 164903, Apr. 2020, doi: 10.1063/5.0004140, by **Yang Zhou** and Peng Zhang.

2.1 Introduction

Laser-driven photoelectron emission is important to photoinjectors in free electron lasers and accelerators [69], [106], ultrafast electron microscopes [15], X-ray sources [107], femtosecond electron diffraction [108], and novel vacuum nanoelectronics [27], [28], [109]. The mechanisms of laser-driven photoemission from metal surfaces have been studied extensively both theoretically and experimentally [106], [110]–[117]. For decades, the fundamental models of photoemission remain those of classical treatment models, such as the three-step model [43], [44], [114]–[117], and the Fowler–DuBridge model [110]–[113]. There have also been recent interests in multi-photon absorption induced over-barrier emission for weak laser fields, photon-assisted tunneling and optical field tunneling emission for strong laser fields [38], [45], [62], [101], [118]. Quantum treatments of photoemission from metal surfaces assume the free electrons inside the metal are confined by a step potential barrier, which can be modulated by a dc field or a laser field [119]. Recently, an analytical model for electron emission from metal surfaces due to arbitrary combination of dc electric field and laser electric field was constructed by solving the time-dependent Schrödinger equation exactly [38]. The model has been extended to two-color laser induced electron emission [91], [92]. It includes the effects of lasers (wavelength and intensity), dc electric field, and metal properties (work function and Fermi level). However, it only considers electrons with initial energy at the Fermi level, without considering the contribution of photoemission from electrons with other initial energies inside the cathode.

Here, we extend the quantum model for photoemission based on the exact solution of time-dependent Schrödinger equation, to include the effects of electron energy states distribution inside the metal, which is assumed to follow the Fermi–Dirac distribution. Electron emission mechanisms under various conditions are analyzed. The quantum efficiency (QE), defined as the number of emitted electrons per incident photon, is calculated from our quantum model. The

results are compared with the three-step model (both the Dowell's analytical model [43], [44] and a simple Monte Carlo simulation), and the Fowler–DuBridge model.

2.2 Analytical Quantum Model

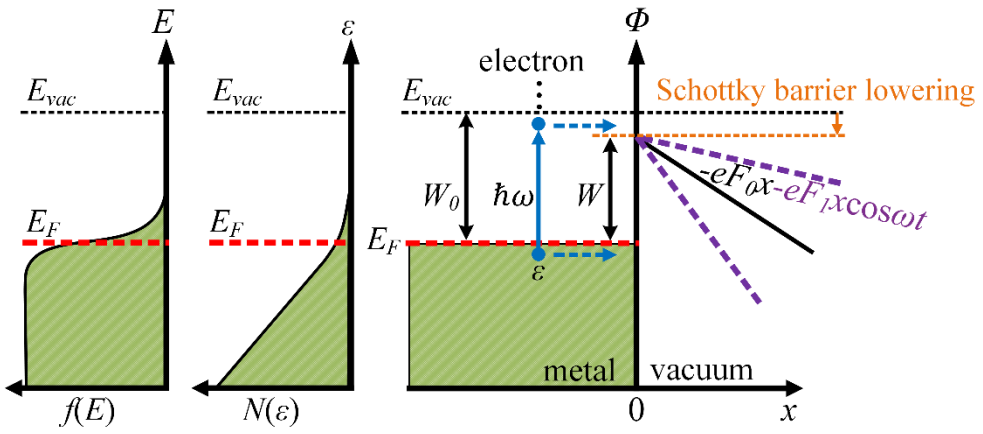

Figure 2.1 Energy diagram for laser-driven photoelectron emission from a metal surface with a dc bias. The metal has Fermi level E_F and original work function W_0. The dc field is F_0, and the laser electric field is $F_1 \cos \omega t$, both of which are assumed perpendicular to the metal surface. The effective work function $W = W_0 - 2\sqrt{e^3 F_0/16\pi\varepsilon_0}$ with the Schottky effect. Left: Electrons inside the metal are assumed to follow the three-dimensional Fermi–Dirac distribution $f(E)$; center: The corresponding 1D electron supply function with longitudinal energy $\varepsilon = E_x$ is $N(\varepsilon)$ (cf. Eq. (2.9) below); and right: the oscillating potential barrier due to laser and dc fields.

Consider a 1D model [38], [91], [92] as shown in Fig. 2.1, in which it is assumed that electrons with initial longitudinal energy ε are emitted from the metal-vacuum interface at $x = 0$, under the action of both a laser field $F_1 \cos \omega t$, and a dc field F_0, where F_1 is the magnitude of the laser field and ω is the angular frequency of the laser. The laser field is assumed to be perpendicular to the interface and cut off abruptly at the surface. This assumption may be justified by that the laser penetration depth is much smaller than the laser wavelength. Thus, the time-dependent surface potential barrier is [38],

$$\Phi(x,t) = \begin{cases} 0, & x < 0 \\ E_F + W - eF_0 x - eF_1 x \cos \omega t\,, & x \geq 0 \end{cases}, \tag{2.1}$$

where E_F is the Fermi level of the metal, $W = W_0 - 2\sqrt{e^3 F_0/16\pi\varepsilon_0}$ is the effective work function including the potential barrier lowering by the Schottky effect due to the dc electric field F_0, W_0 is the metal work function, e is the electron charge (positive), and ε_0 is the free space permittivity. Note that, though Eq. (2.1) assumes a linear potential in order to yield analytical solution, it has been verified in ref. [38] that this approach gives a very good

approximation of the more realistic nonlinear potential including image charge [120]. Due to the omission of the laser penetration inside the metal, the effects of electron-electron scattering and electron-photon scattering, which may happen when electrons inside the metal move to the surface, are also ignored in this model.

The electron wave function $\psi(x,t)$ can be solved from the time-dependent Schrödinger equation,

$$i\hbar\frac{\partial\psi(x,t)}{\partial t} = -\frac{\hbar^2}{2m}\frac{\partial^2\psi(x,t)}{\partial x^2} + \Phi(x,t)\psi(x,t), \tag{2.2}$$

where $\hbar$ is the reduced Planck's constant, m is the electron mass, and $\Phi(x,t)$ is the laser field modulated surface potential barrier given in Eq. (2.1).

For $x < 0$, the solution to Eq. (2.2) is

$$\psi(x,t) = e^{-i\frac{\varepsilon}{\hbar}t + ik_0x} + \sum_{n=-\infty}^{\infty} R_n e^{-i\frac{\varepsilon+n\hbar\omega}{\hbar}t - ik_nx}, \tag{2.3}$$

where ε is the electron initial energy, R_n is the reflection coefficient of the incident electron wave after absorption ($n > 0$) or emission ($n < 0$) of n photons. Equation (2.3) is the superposition of incident electron wave with the wave vector of $k_0 = \sqrt{2m\varepsilon/\hbar^2}$, and reflected electron waves from the metal-vacuum interface with the wave vector of $k_n = \sqrt{2m(\varepsilon + n\hbar\omega)/\hbar^2}$.

Taking the Truscott transformation [121], the exact solution to Eq. (2.2) for $x \geq 0$ is found to be [38], [91], [92],

$$\psi(x,t) = \begin{cases} \sum_{n=-\infty}^{\infty} T_n e^{i\sqrt{\frac{2mE_n}{\hbar^2}}\xi}\Theta(x,t), & F_0 = 0; \\ \sum_{n=-\infty}^{\infty} T_n G_n(x,t)\Theta(x,t)e^{-i\frac{e^2F_0F_1\sin\omega t}{\hbar m\omega^3}}, & F_0 \neq 0, \end{cases} \tag{2.4}$$

where T_n is the electron wave transmission coefficient, $\xi = x + \left(\frac{eF_1}{m\omega^2}\right)\cos\omega t$, $E_n = \varepsilon + n\hbar\omega - E_F - W - U_p$ with $U_p = e^2F_1^2/4m\omega^2$, $\Theta(x,t) = \exp\left(-i\frac{\varepsilon+n\hbar\omega}{\hbar}t + i\frac{eF_1\sin\omega t}{\hbar\omega}x + i\frac{e^2F_1^2\sin 2\omega t}{8\hbar m\omega^3}\right)$, $G_n(x,t) = Ai(-\eta_n) - iBi(-\eta_n)$ with $\eta_n = (E_n/eF_0 + \xi)(2emF_0/\hbar^2)^{1/3}$, and Ai and Bi are the Airy function of the first and second kind. Equation (2.4) is the transmitted electron wave traveling to the vacuum side, and it is the superposition of electron waves with the energy of $\varepsilon + n\hbar\omega$ induced by different emission mechanisms, namely multiphoton absorption ($n > 0$),

tunneling ($n = 0$) and multiphoton emission ($n < 0$) [38], [91], [92].

Using boundary conditions that both $\psi(x,t)$ and $\partial\psi(x,t)/\partial x$ are continuous at $x = 0$, and taking the Fourier transform, we obtain, in the normalized form,

$$2\sqrt{\bar{\varepsilon}}\delta(l) = \sum_{n=-\infty}^{\infty} T_n\left(\sqrt{\bar{\varepsilon} + l\bar{\omega}}P_{n(n-l)} + Q_{n(n-l)}\right), \tag{2.5}$$

where δ is the Dirac delta function, $P_{nl} = 1/2\pi \times \int_0^{2\pi} p_n(\bar{\omega}\bar{t})e^{-il\bar{\omega}\bar{t}}d(\bar{\omega}\bar{t})$ and $Q_{nl} = 1/2\pi \times \int_0^{2\pi} q_n(\bar{\omega}\bar{t})e^{-il\bar{\omega}\bar{t}}d(\bar{\omega}\bar{t})$ are the Fourier transform coefficients, with

$$p_n(\bar{\omega}\bar{t}) = e^{i\frac{\bar{F}_1^2}{4\bar{\omega}^3}\sin 2\bar{\omega}\bar{t}}e^{i\frac{2\bar{F}_1}{\bar{\omega}^2}\sqrt{\bar{E}_n}\cos\bar{\omega}\bar{t}}, \qquad q_n(\bar{\omega}\bar{t}) = p_n(\bar{\omega}\bar{t})\left[\sqrt{\bar{E}_n} + \frac{\bar{F}_1}{\bar{\omega}}\sin\bar{\omega}\bar{t}\right], \tag{2.6a}$$

for $F_0 = 0$, and

$$p_n(\bar{\omega}\bar{t}) = z(\bar{\omega}\bar{t})s(\alpha_n), \qquad q_n(\bar{\omega}\bar{t}) = z(\bar{\omega}\bar{t})\left[\frac{\bar{F}_1\sin\bar{\omega}\bar{t}}{\bar{\omega}}s(\alpha_n) + \bar{F}_0^{\frac{1}{3}}r(\alpha_n)\right], \tag{2.6b}$$

for $F_0 \neq 0$, with $z(\bar{\omega}\bar{t}) = \exp\left(-i\frac{2\bar{F}_0\bar{F}_1\sin\bar{\omega}\bar{t}}{\bar{\omega}^3} + i\frac{\bar{F}_1^2\sin 2\bar{\omega}\bar{t}}{4\bar{\omega}^3}\right)$, $s(\alpha_n) = Ai(\alpha_n) - iBi(\alpha_n)$, $r(\alpha_n) = iAi'(\alpha_n) + Bi'(\alpha_n)$, and $\alpha_n = -\left[\bar{E}_n/\bar{F}_0 + (2\bar{F}_1/\bar{\omega}^2)\cos(\bar{\omega}\bar{t})\right]\bar{F}_0^{\frac{1}{3}}$. A prime denotes the derivative with respect to its argument. The quantities with a bar are in their normalized form, defined as $\bar{\varepsilon} = \varepsilon/W$, $\bar{\omega} = \hbar\omega/W$, $\bar{t} = tW/\hbar$, $\bar{x} = x/\lambda_0$, $\lambda_0 = \sqrt{\hbar^2/2mW}$, $\bar{F}_0 = F_0 e\lambda_0/W$, $\bar{F}_1 = F_1 e\lambda_0/W$, $\bar{E}_F = E_F/W$, $\bar{U}_p = U_p/W$, and $\bar{E}_n = E_n/W = \bar{\varepsilon} + n\bar{\omega} - \bar{E}_F - 1 - \bar{U}_p$. Therefore, the electron wave transmission coefficient T_n can be obtained from Eq. (2.5).

The probability of electron transmission can be calculated by $w(\varepsilon,x,t) = J_t(\varepsilon,x,t)/J_i(\varepsilon)$, where $J(\varepsilon,x,t) = (i\hbar/2m)(\psi\nabla\psi^* - \psi^*\nabla\psi)$, J_i and J_t are the incident and transmitted electron probability current density respectively. The time-averaged probability of electron transmission from initial energy of ε after n-photon process, $\langle w_n(\bar{\varepsilon})\rangle$, is,

$$\langle w_n(\bar{\varepsilon})\rangle = \begin{cases} \mathrm{Im}\left(i\dfrac{\sqrt{\bar{E}_n}}{\sqrt{\bar{\varepsilon}}}|T_n|^2\right), & F_0 = 0, \\ \dfrac{\bar{F}_0^{1/3}}{\pi\sqrt{\bar{\varepsilon}}}|T_n|^2, & F_0 \neq 0, \end{cases} \tag{2.7}$$

and the total electron transmission probability $D(\bar{\varepsilon})$ from initial energy ε is the sum of $\langle w_n(\bar{\varepsilon})\rangle$,

$$D(\bar{\varepsilon}) = \sum_{n=-\infty}^{\infty} \langle w_n(\bar{\varepsilon}) \rangle . \tag{2.8}$$

The emission current density can thereby be obtained by,

$$J = e \int_0^{\infty} D(\varepsilon) N(\varepsilon) d\varepsilon , \tag{2.9}$$

where $D(\varepsilon)$ is given in Eq. (2.8), and $N(\varepsilon) = \frac{mk_BT}{2\pi^2\hbar^3} \ln\left(1 + e^{\frac{E_F - \varepsilon}{k_BT}}\right)$ is the supply function, with $N(\varepsilon)d\varepsilon$ being the flux of electrons inside the metal impinging on the metal surface with longitudinal energy between ε and $\varepsilon + d\varepsilon$ across a unit area per unit time, calculated from free-electron theory of metal [122]–[124].

The quantum efficiency (QE) is defined as the ratio of the number of emitted electrons to that of incident photons,

$$QE = \frac{J/e}{I/\hbar\omega}, \tag{2.10}$$

where I is the intensity of the incident laser, which is related to the laser electric field as I [W/cm^2] $= \varepsilon_0 c F_1^2/2 = 1.33 \times 10^{11} \times (F_1[\mathrm{V/nm}])^2$ for linearly polarized plane waves.

2.3 Results and Discussion

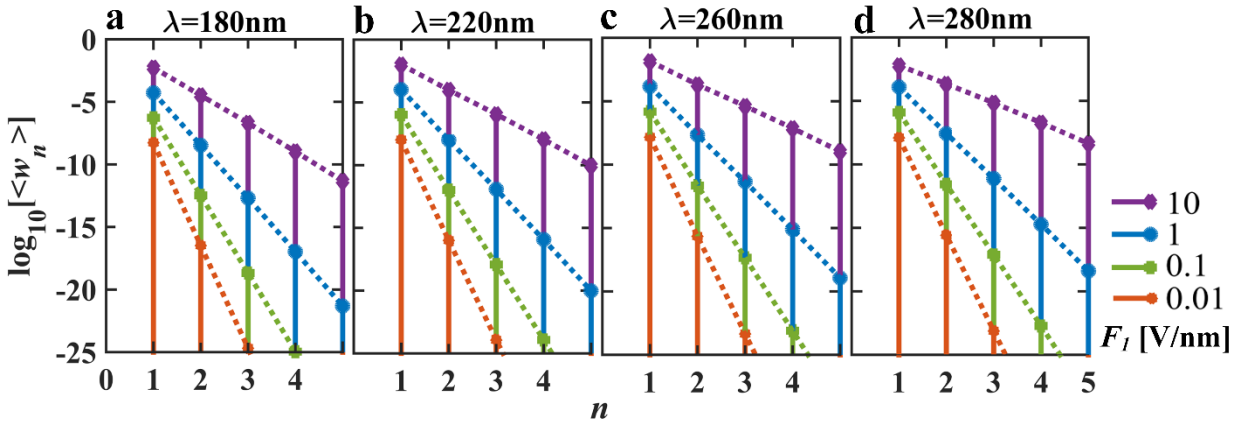

Figure 2.2 Time-averaged electron transmission probability $\langle w_n(\varepsilon) \rangle$ through nth channel (or n-photon process) from electron initial energy $\varepsilon = E_F$, under various combinations of laser wavelengths λ and laser fields F_1, with dc field $F_0 = 0$. The metal is assumed to be copper, with $E_F = 7$ eV and $W_0 = 4.31$ eV. The laser intensity corresponding to laser field F_1 (V/nm) is I [W/cm^2] $= \varepsilon_0 c F_1^2/2 = 1.33 \times 10^{11} \times (F_1[\mathrm{V/nm}])^2$.

Figure 2.2 shows the time-averaged electron transmission probability $\langle w_n(\varepsilon) \rangle$ through the n-photon process from copper, under various combinations of laser fields and wavelengths. The

laser wavelengths for Figs. 2.2(a) – 2.2(d) are 180 nm, 220 nm, 260 nm and 280 nm, corresponding to the photon energy of 6.89 eV, 5.64 eV, 4.77 eV and 4.43 eV, respectively. The applied dc field is 0. The laser fields F_1 for lines in colors of purple, blue, green and orange, are 10 V/nm, 1 V/nm, 0.1 V/nm and 0.01 V/nm, corresponding to the laser intensity of 1.33×10^{13}, 1.33×10^{11}, 1.33×10^{9} and 1.33×10^{7} W/cm^2, respectively. The electron initial energy ε is assumed to be at the Fermi level E_F.

It is clear that the electron transmission probability through the *n*th channel increases when the laser field increases. The dominant emission process is through the single photon absorption induced over-barrier emission ($n = 1$). Calculations with applied dc fields F_0 of up to 0.1 V/nm, show F_0 has little effects on the transmission probability spectrum, indicating that the Schottky effect is negligible for such a small dc bias in the laser wavelength range of 180 nm – 280 nm on copper cathodes.

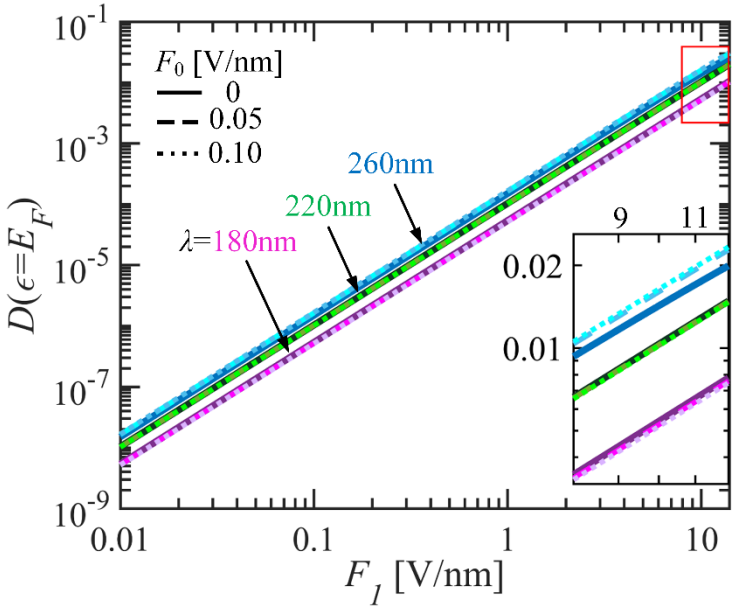

Figure 2.3 The electron transmission probability $D(\varepsilon)$ at initial energy of E_F as a function of laser electric field F_1, for various laser wavelengths λ and dc fields F_0. The metal is assumed to be copper, with $E_F = 7$ eV and $W_0 = 4.31$ eV.

The effects of laser fields F_1 (or laser intensity I), dc fields F_0, and laser wavelengths λ on the total electron transmission probability $D(\varepsilon)$ from initial energy of E_F is shown in Fig. 2.3. For the relatively small applied dc field (up to 0.1 V/nm), the electron transmission probability is well scaled as $D(\varepsilon) \propto F_1^2$ for wavelengths shown in Fig. 2.3, indicating the dominant single-photon process. This is consistent with the characterization based on the Keldysh parameter $\gamma =$

$\sqrt{W/2U_p} = \omega\sqrt{2mW}/eF_1$, which is used to characterize the transition from multiphoton absorption ($\gamma \gg 1$) to strong field emission ($\gamma \ll 1$). The smallest Keldysh parameter is $\gamma = 4.04$ when $F_1 = 12$ V/nm, $F_0 = 0.1$ V/nm at $\lambda = 260$ nm, implying that strong-field emission can be neglected. When the laser wavelength increases from 180 nm to 260 nm, the corresponding photon energy decreases from 6.89 eV to 4.77 eV and becomes closer to the potential barrier seen by the electrons (i.e., $W \cong 4.31$ eV), leading to an increasing transmission probability $D(\varepsilon)$. This is consistent with our previous study that the maximum transmission occurs when the photon energy equals to the potential barrier, $\hbar\omega/W \approx 1$ (cf. Fig. 6c of [38]). When the dc field increases, the potential barrier becomes narrower (Fig. 2.1), thus increasing the electron tunneling probability. In the meantime, the effective work function decreases because of the Schottky effect. The effects of dc field are more pronounced for the larger laser wavelength (or smaller photon energy) of $\lambda = 260$ nm, as shown in the inset of Fig. 2.3. When the dc field is strong, e.g., $F_0 = 5$ V/nm, the dominant emission process becomes dc field emission ($n = 0$) when laser field is small, and electron transmission probability $D(\varepsilon = E_F)$ is independent of the laser wavelengths (not shown).

The electron transmission probability $D(\varepsilon)$ at different initial electron energy ε is shown in Fig. 2.4. The solid curves, which give $D(\varepsilon)$ as a function of ε at various laser fields, show a stair-like behavior. Each "stair" indicates a specific *n*-photon absorption for electrons with initial energy in that range. The energy between step points corresponds to the laser photon energy $\hbar\omega$. Take Figs. 2.4a(ii), (v) and (viii) for $\lambda = 220$ nm as an example, whose projections in the $D - \varepsilon$ plane and in the $D - F_1$ plane for a few selected curves are shown in Figs. 2.4b and 2.4c respectively. When $F_0 = 0$, the first step point is at $\varepsilon = 5.67$ eV (Fig. 2.4b), which equals $E_F + W_0 - \hbar\omega$, representing the electron initial energy threshold for one-photon emission. The second step point is near the bottom of the energy state. The difference between the two step points is 5.64 eV, which is the photon energy of the 220 nm laser. Electrons with initial energy in this range emit through two-photon absorption. The transmission probability $D(\varepsilon)$ of electrons with initial energy ε in the same stair range keeps almost constant under the same laser field F_1, only with a slight decrease as ε increases in that stair range. The difference in $D(\varepsilon)$ between stairs decreases when F_1 increases. For a given F_1, when the applied dc field F_0 increases, the step point shifts to smaller ε, because the surface potential barrier (or effective work function) is lowered by the applied dc field. The transition between stairs becomes gradual when there is dc

field instead of a sharp transition when there is no dc field. Figure 2.4c shows $D(\varepsilon)$ as a function of laser field F_1 with various electron initial energies when the laser wavelength is 220 nm. When the electron is with initial energy of 2 eV and 4 eV, $D(\varepsilon)$ is well scaled as $D(\varepsilon) \propto F_1^{2n} = F_1^4$ for the applied dc field up to 0.1 V/nm, indicating the dominant two-photon absorption process. When the electron is with initial energy of 5 eV, the dominant emission is through two-photon absorption for dc field smaller than 0.05 V/nm. When the applied dc field $F_0 = 0.1$ V/nm, which induces an effective work function of $W = 3.93$ eV, the effective potential barrier seen by an electron at $\varepsilon = 5$ eV becomes $E_F + W - \varepsilon$ =5.93 eV (compare to photon energy of 5.64 eV for 220 nm laser). The electron is emitted through single photon assisted tunneling ($n = 1$) in the laser field range from $F_1 = 0.001$ V/nm to 1 V/nm. The dominant emission process shifts to high order channels ($n = 2$) when the laser field gets larger in the range from $F_1 = 1$ to 10 V/nm, as shown in Fig. 2.4(c), which is consistent with our previous observation (cf. Fig. 2 of [38]).

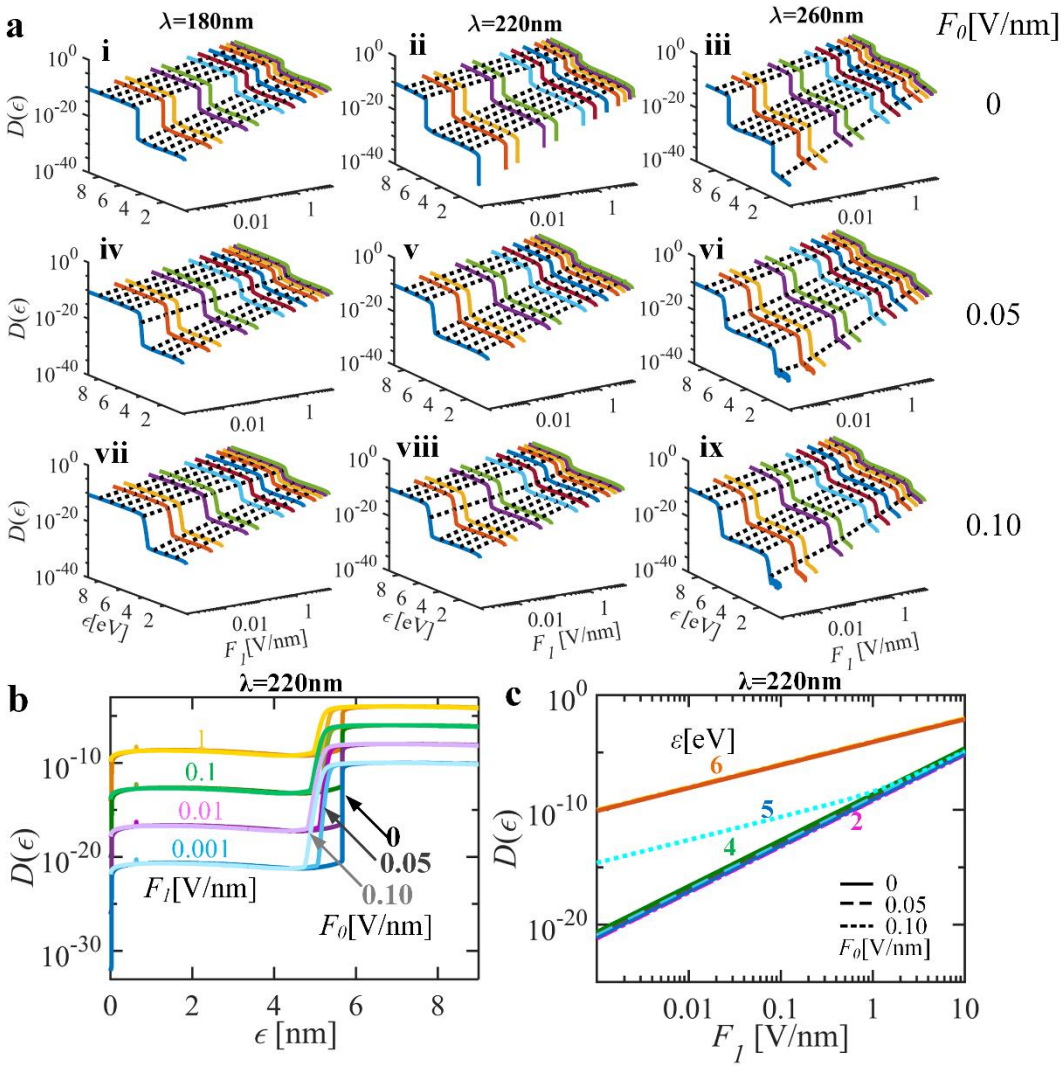

Figure 2.4 Electron transmission probability $D(\varepsilon)$ as a function of electron initial energy ε, for different laser field F_1, dc field F_0, and laser wavelength λ. The metal is assumed to be copper, with $E_F = 7$ eV and $W_0 = 4.31$ eV.

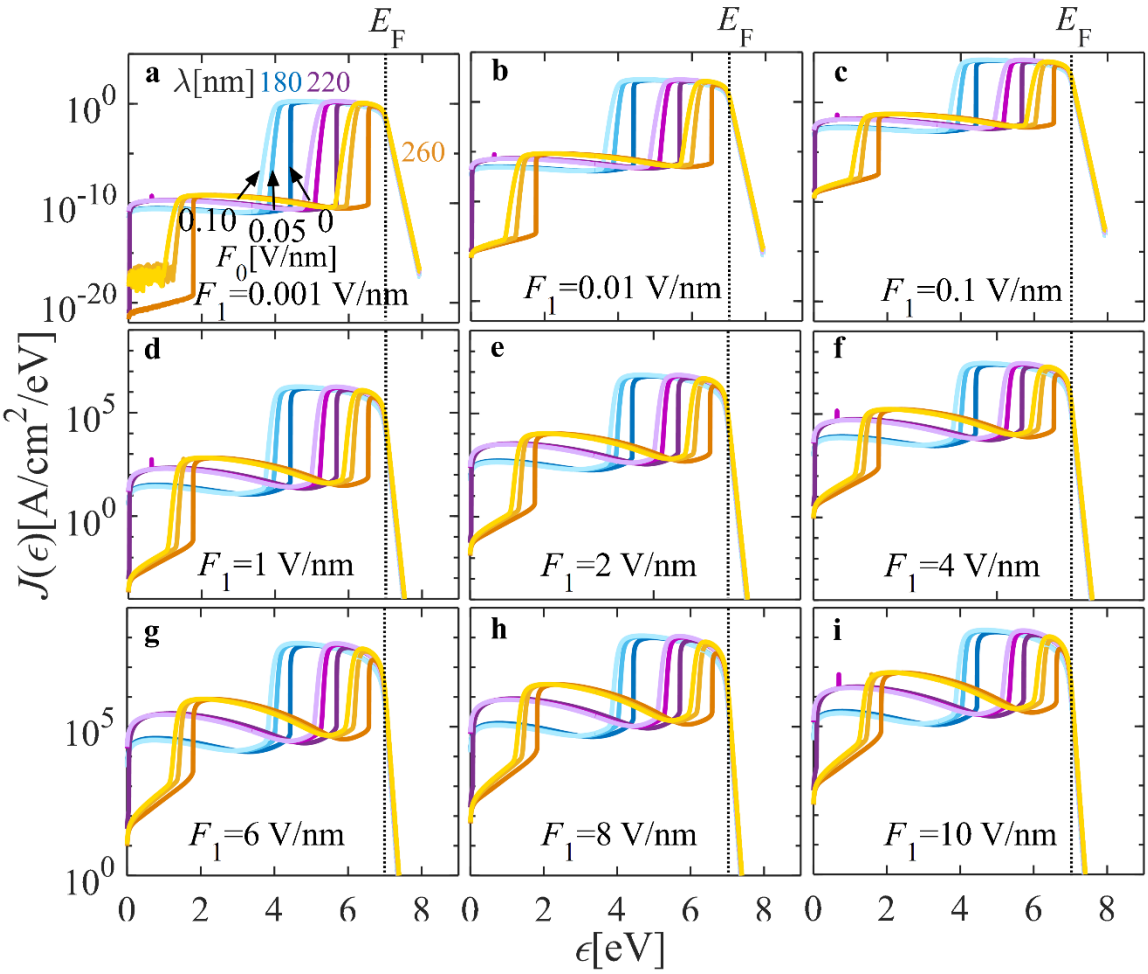

Figure 2.5 Electron emission current density per electron initial energy $J(\varepsilon) = eD(\varepsilon)N(\varepsilon)$ as a function of electron initial energy ε under various combinations of laser fields, dc fields and wavelengths. The metal is assumed to be copper, with $E_F = 7$ eV and $W_0 = 4.31$ eV. The temperature is assumed at $T = 300$ K. **Erratum**: in ref. [125], y-axis label should be $J(\varepsilon)[\mathrm{A}/\mathrm{cm}^2/J]$ as for the scale in Fig. 5; here it has be converted to $J(\varepsilon)[\mathrm{A}/\mathrm{cm}^2/eV]$.

Figure 2.5 presents the electron emission current density per energy $J(\varepsilon) = eN(\varepsilon)D(\varepsilon)$ as a function of electron initial energy ε under various combinations of laser fields, dc fields and laser wavelengths. Most electrons are emitted from electron initial energy of a few eVs below the Fermi level, through single photon absorption. The range of the electron initial energy of single photon emission is determined by the incident laser photon energy. The shorter the laser wavelength, the larger the range, therefore, more electrons are emitted. Few electrons above the Fermi level are emitted, because there are fewer electrons distributed in that energy range at room temperature. The dc field extends the dominant electron emission range to a lower value, and therefore more electrons with smaller initial energy are able to emit. The electron emission

current density per energy $eN(\varepsilon)D(\varepsilon)$ also shows stair-like dependence on the electron initial energy ε, indicating different n-photon absorption process for electrons with initial energy in different "stairs". The step points correspond to the initial energy threshold for an electron to emit after absorption of integer number of photons $E_F + W - n\hbar\omega$. When the laser field F_1 increases, the electron emission current density also increases, but the difference of emission current density between stairs gets smaller, especially for longer laser wavelength, which means multi-photon absorption process contributes more significantly to the electron emission. When the laser field F_1 is small, as in Figs. 2.5(a)–2.5(c), the "stairs" are flat. When F_1 increases, $eN(\varepsilon)D(\varepsilon)$ from larger initial energy becomes smaller than that from smaller initial energy in the same "stair", which is similar to the transmission probability $D(\varepsilon)$ observed in Fig. 2.4.

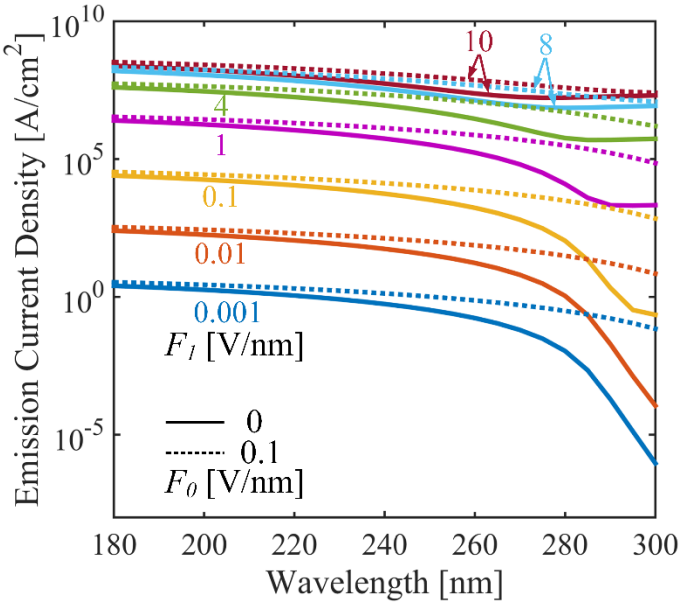

Figure 2.6 Total electron emission current density as a function of laser wavelength under various laser fields F_1 and dc fields F_0. The metal is assumed to be copper, with $E_F = 7$ eV and $W_0 = 4.31$ eV. The electron temperature is assumed at $T = 300$ K.

Figure 2.6 shows the total electron emission current density J as a function of laser wavelength under various laser fields, as calculated from Eq. (2.9). It is clear that when laser field increases, the total emission current density also increases, especially in the longer wavelength. When the laser field is small ($F_1 < 0.1$ V/nm), there is an obvious drop in the current density at a longer wavelength. When the laser field is larger, the electron emission current density becomes less sensitive to the laser wavelength. The application of dc field increases the total electron emission current density, due to both narrowing and lowering of the

potential barrier. The increase of the emission current density due to the dc field is more significant for longer laser wavelengths.

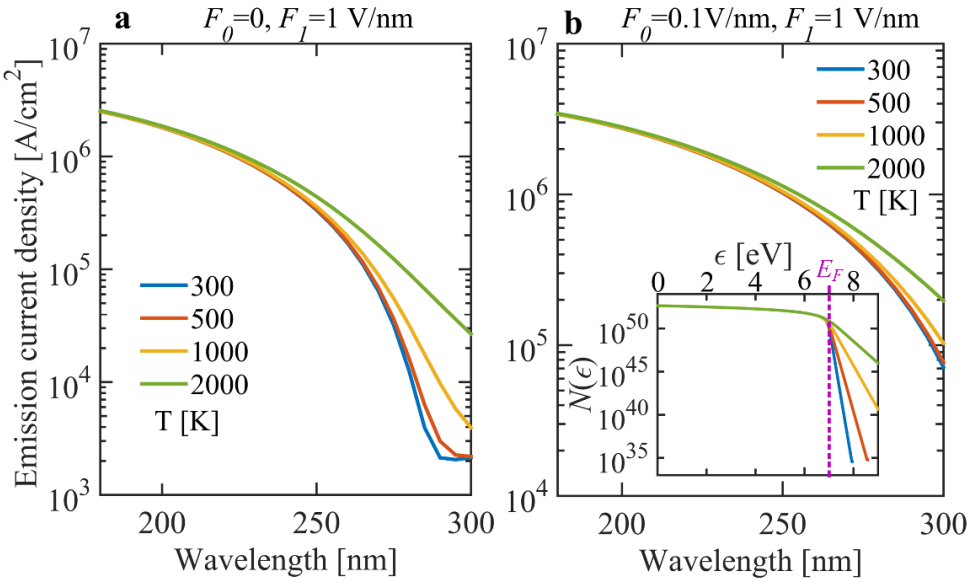

Figure 2.7 Total electron emission current density as a function of laser wavelength with different temperatures. The laser field $F_1 = 1$ V/nm, and dc field $F_0 = 0$ for (a) and $F_0 = 0.1$ V/nm for (b). The inset in (b) is the supply function $N(\varepsilon)$ under various temperatures. The metal is assumed to be copper, with $E_F = 7$ eV and $W_0 = 4.31$ eV.

Regarding the high power of the laser used for photoemission, the temperature near the surface of the metal could increase substantially. The effects of temperature on the emission current are shown in Fig. 2.7. The laser field F_1 is 1 V/nm, and the temperature in the Fermi-Dirac function is set to be $T = 300$, 500, 1000 and 2000 K. It is clear that higher temperature can increase the emission current density in the longer laser wavelength range. As the electron temperature increases, there are more electrons near or above the Fermi level which are able to emit and induce a larger emission current density. Electrons with initial energy above the Fermi level can emit through single photon absorption in the longer laser wavelength range, whose transmission probability is several orders higher than electrons with lower energy (cf. Fig. 2.4). Therefore, the electron emission current density is greatly enhanced in the longer laser wavelength range. In the shorter laser wavelength range, electrons mostly emit through single photon absorption over a wider range of initial energy around the Fermi level, therefore, the emission current density is insensitive to temperature.

Figure 2.8 shows quantum efficiency (QE) as a function of laser wavelength and laser field for different dc fields, as obtained from Eq. (2.10). For smaller laser wavelength in the range of

180 nm – 260 nm, QE changes little when the laser field F_1 increases from 0 to 10 V/nm, for a fixed dc field F_0. In this wavelength range, the electron emission is dominated by single photon absorption, giving the scaling of the emission electron current density as $J \propto F_1^2$, or $J \propto I$, thus, a constant QE $\propto J/I$ independent of F_1, as seen from Figs. 2.8(c) and 2.8(f). For laser wavelength in 260 nm – 300 nm, QE increases when the input laser field F_1 increases. This is due to the increase in electron emission through multiphoton absorption ($n > 1$), as shown in Fig. 2.2. For the case of 300 nm, QE is increased by at least four orders of magnitude when F_1 increases from 0.001 V/nm to 10 V/nm (cf. Fig. 2.8c with $F_0 = 0$), indicating that multiphoton absorption contributes significantly in this case. Applying a dc field will increase QE, as shown in Figs. 2.8d – 2.8f. The increase of QE due to the dc field is more profound in the longer laser wavelength range for small laser field (e.g., λ in the range of 260 nm – 300 nm with $F_1 < 1$ V/nm). It is also found that QE becomes less sensitive to the laser field F_1 when dc field F_0 is increased, especially for longer laser wavelength in 260 nm – 300 nm.

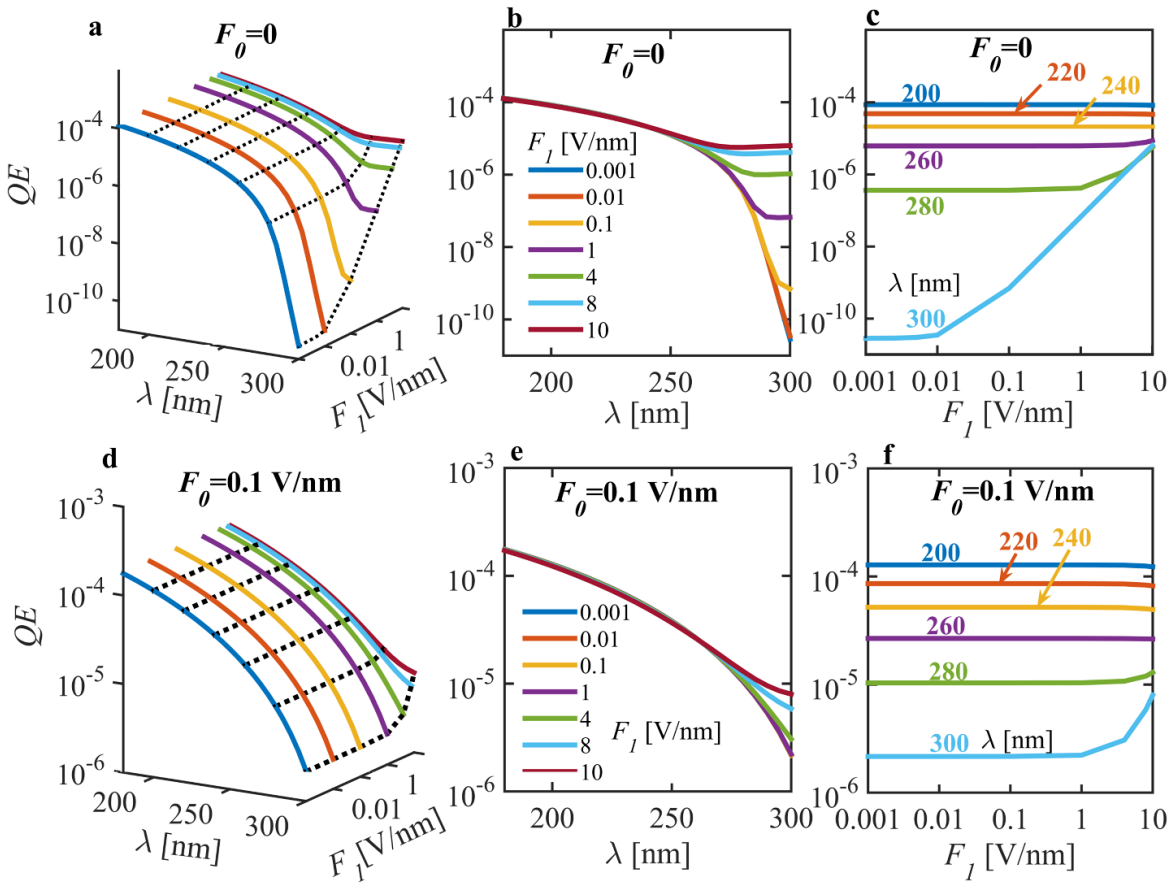

Figure 2.8 Quantum efficiency calculated from the quantum model under various laser fields in the laser wavelength range of 180 – 300 nm for dc field F_0 of (a) – (c) 0 V/nm, and (d) – (f) 0.1 V/nm. The metal is assumed to be copper, with $E_F = 7$ eV and $W_0 = 4.31$ eV. The temperature is assumed at $T = 300$ K.

2.4 Comparison with Classical Models

In this section, we compare our quantum model with the widely used three-step model (TSM) [43], [44], [114]–[117] and Fowler-DuBridge (FD) model [110]–[113]. A brief summary of those two classical models is provided below.

2.4.1 Three-step Model

Photoemission from metal surfaces is described in three sequential independent steps. First, electrons are excited to states of higher energies after absorption of photons. Next, the excited electrons move to the surface, which involves physical processes such as electron-electron scattering in metals. Finally, electrons overcome the surface potential barrier and escape into the vacuum, with a probability depending on their momentum and the surface potential. The quantum efficiency of photoemission from metal surfaces, defined as the ratio of the number of emitted electrons to that of the incident photons, is the product of the probability of those three

steps [43], [44],

$$QE = [1 - R(\omega)] \times \frac{\int_{E_F+W-\hbar\omega}^{\infty} dE[1 - f_{FD}(E + \hbar\omega)]f_{FD}(E) \int_{\cos\theta_{max}(E)}^{1} d(\cos\theta)\, F_{e-e}(E, \omega, \theta) \int_0^{2\pi} d\phi}{\int_{E_F-\hbar\omega}^{\infty} dE[1 - f_{FD}(E + \hbar\omega)]f_{FD}(E) \int_{-1}^{1} d(\cos\theta) \int_0^{2\pi} d\phi}, \quad (2.11)$$

where $R(\omega)$ is the reflectivity at frequency of ω, the laser is assumed incident perpendicular to the metal surface; $f_{FD}(E) = 1/(1 + \exp[(E - E_F)/k_B T])$ is the Fermi-Dirac function, describing the electron energy states distribution inside the metal; W is the effective work function, including the Schottky effect, which is the maximum of the Schottky potential composed of both image charge field and applied dc field F_0; $F_{e-e}(E, \omega, \theta)$ is the probability that electrons survive the e-e scatterings to reach the surface; θ is the angle between the velocity of the electron and the surface normal, and ϕ is the azimuthal angle on the surface. $\cos[\theta_{max}(E)] = \sqrt{(E_F + W)/(E_F + \hbar\omega)}$ gives the maximum angle of the electron velocity with respect to the normal of the surface, at which an electron can reach the surface and may eventually escape.

There are assumptions made to simplify the model. First, the metal is assumed to be at low temperature. Therefore, the Fermi-Dirac function can be approximated as a step function, with fully occupied states below E_F and empty states above E_F. Second, the photon energy of input laser is assumed to be near the threshold of photoemission, so that most of the emitted electrons are with velocity normal to the surface, and therefore the θ dependence of $F_{e-e}(E, \omega, \theta)$ can be ignored. Implied in Eq. (2.11) is that electrons with the momentum normal to the surface greater than the critical barrier momentum may escape, which satisfies $p_\perp^2/2m > E_F + W$, where $p_\perp$ is the momentum normal to the surface. Thus, the model in Eq. (2.11) can be simplified as [43], [44]

$$QE = [1 - R(\omega)]F_{e-e}\frac{(E_F + \hbar\omega)}{2\hbar\omega}\left[1 + \frac{E_F + W}{E_F + \hbar\omega} - 2\sqrt{\frac{E_F + W}{E + \hbar\omega}}\right], \quad (2.12)$$

where $F_{e-e}(\omega) = 1/\left(1 + \frac{\lambda_{opt}(\omega)}{\lambda_{e-e}(\omega)}\right)$, $\lambda_{opt}(\omega) = \lambda/4\pi k(\omega)$ is the optical penetration depth, λ is the laser wavelength and $k(\omega)$ is the imaginary part of the refractive index, and $\lambda_{e-e}(\omega) = \frac{2\lambda_m E_m^{3/2}}{\hbar\omega\sqrt{W}}\frac{1}{1+\sqrt{W/\hbar\omega}}$ is the mean free path of electron-electron scattering, with λ_m being a known value of electron-electron scattering mean free path for electrons at energy E_m above the Fermi level. Note that Eq. (2.12) is only a limiting case of TSM and is valid when the photon energy

$\hbar\omega$ is close to the work function W. When $\hbar\omega$ is not close to W, scattered electrons with transverse energies and multiphoton processes may contribute greatly to the total emission and have to be considered in a more general three-step formalism [126].

2.4.2 Fowler-DuBridge Model

Fowler-DuBridge model for photoemission [110]–[113] are based on the following assumptions: (a) electrons inside a metal follow Fermi-Dirac distribution, and electrons are distributed uniformly in the momentum space; (b) the probability of a photon absorbed by an electron is independent of the electron's initial energy state; (c) only the electron momentum component normal to the surface is increased by the absorption of photon; (d) an electron can escape from the surface, if the electron momentum normal to the surface is greater than the threshold determined by the metal work function; (e) the quantum efficiency is proportional to the number of electrons impinging on the surface, per unit area per unit time, whose kinetic energy associated with the momentum normal to the metal surface is greater than the work function of the metal. For the laser wavelength shorter than the threshold wavelength, the single photon emission is dominant and multiphoton processes are ignored, which yields [110],

$$QE = a_1(1-R)\frac{2}{h^3}\int_{-\infty}^{\infty} dp_x \int_{-\infty}^{\infty} dp_y \int_{p_1}^{\infty} dp_z \frac{p_z/m}{\exp\left(\frac{{p_x}^2+{p_y}^2+{p_z}^2}{2mk_BT}-\frac{E_F}{k_BT}\right)+1}, \qquad (2.13)$$

where p_x and p_y are the momentum along the metal surface, p_z is the momentum normal to the surface, $p_1 = \sqrt{2m(W+E_F-\hbar\omega)}$ is the minimum momentum normal to the surface required for an electron to overcome the potential barrier to emit, h is the Planck's constant, k_B is the Boltzmann constant, T is the electronic temperature, E_F is the Fermi energy, R is the metal surface reflectivity, $R = [(n_0-1)^2+k^2]/[(n_0+1)^2+k^2]$ when the laser is incident normal to the surface, n_0 is the real part of the refractive index, k is extinction coefficient or the imaginary part of the refractive index, α_1 is a constant, which can be experimentally determined, $a_1 = 5\times10^{-18}$ m^2/A [127] for copper, and $a_1 = 7\times10^{-18}$ m^2/A for gold, which is obtained by fitting with TSM results.

By performing the integral in Eq. (2.13), the quantum efficiency can be expressed as [110]–[113]

$$QE = a_1(1-R)AT^2F\left(\frac{\hbar\omega-W}{k_BT}\right), \qquad (2.14)$$

where A=120 A/cm^2/K^2 is Richardson's constant, $F(x)$ is Fowler's function, which is [110]–[112]

$$F(x)=\begin{cases} e^{x}-\dfrac{e^{2x}}{2^2}+\dfrac{e^{3x}}{3^2}-\cdots, & x<0, \\ \dfrac{\pi^2}{6}+\dfrac{1}{2}x^2-\left[e^{-x}-\dfrac{e^{-2x}}{2^2}+\dfrac{e^{-3x}}{3^2}-\cdots\right], & x>0. \end{cases} \tag{2.15}$$

2.4.3 Comparison Results

Figures 2.9 (a) and 2.9(b) show QE as a function of laser wavelength calculated by the quantum model (Eq. 2.10), TSM (Eq. 2.12), FD model (Eq. 2.14), and Monte Carlo (MC) simulation based on TSM, for both copper and gold. In the calculation, the photon energy of the laser is chosen to be larger than the work function of the metal, such that the dominant electron emission mechanism is single-photon absorption. The laser field F_1 in the quantum model is assumed to be 0.01V/nm. Though the absolute values for the QE from the quantum model are about one order smaller than those of the other models, their scalings are in remarkable agreement. In fact, by multiplying the QE from the quantum model with a constant C ($= 13.963$ and 19.142 for copper and gold respectively), it matches the TSM and FD model results very well, as shown in Figs. 2.9a and 2.9b.

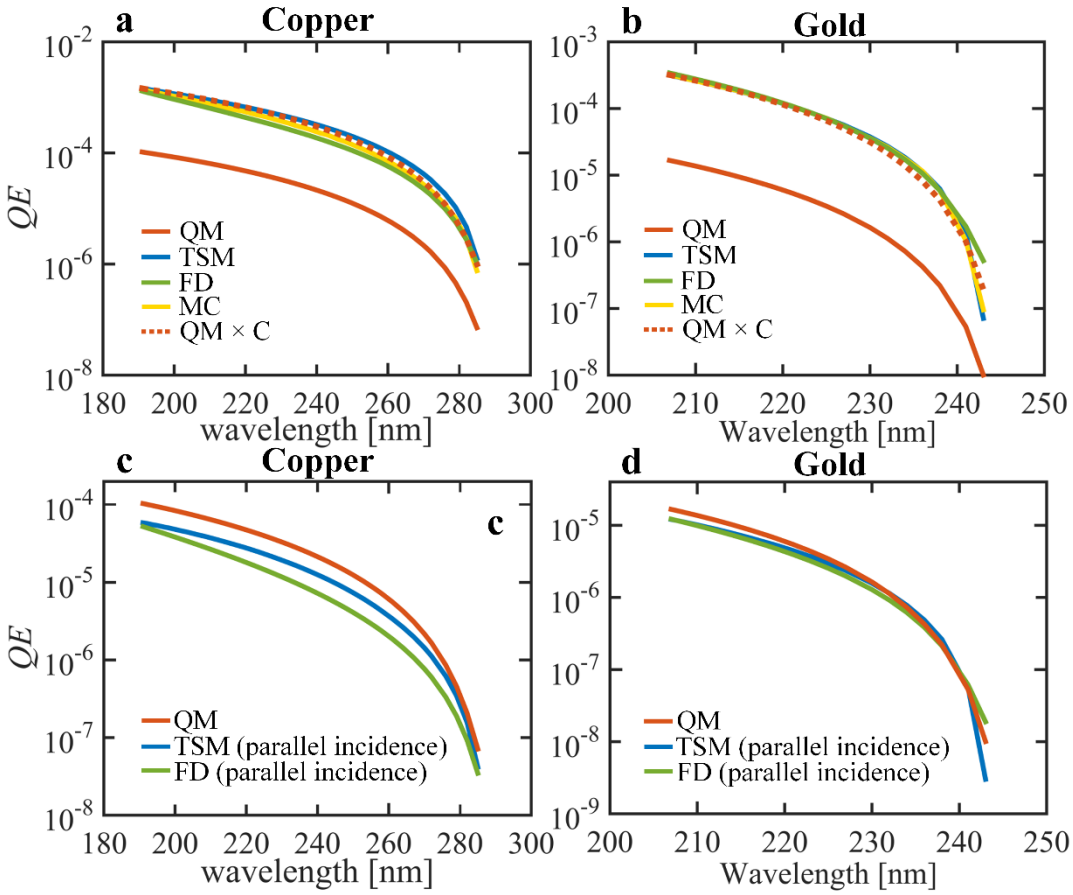

Figure 2.9 (a), (b) Quantum efficiency (QE) from quantum model (QM) (Eq. 2.10), Three-step model (TSM) (Eq. 2.12), Monte Carlo (MC) simulation based on TSM, and Fowler-DuBridge model (FD model) (Eq. 2.14), and the fitted QM $\times\, C$ (= 13.963 and 19.142 for copper and gold respectively); (c), (d) QE from QM (Eq. 2.10), and TSM (Eq. 2.16) and FD model (Eq. 2.17) for parallel incidence. In all the calculations, we assume the dc field $F_0 = 0$. For copper, $E_F = 7$ eV and $W_0 = 4.31$ eV [43], [44]; and for gold, $E_F = 5.53$ eV and $W_0 = 5.1$ eV [38], [91], [92]. In the QM, the laser field $F_1 = 0.01$ V/nm. In both MC simulation and TSM, $E_m = 8.6$ eV and the corresponding $\lambda_m = 2.2$ nm are used, for both copper [116], and gold [117]. In FD model, $a_1 = 5 \times 10^{-18}$ m^2/A [127] for copper, and $a_1 = 7 \times 10^{-18}$ m^2/A for gold (by fitting to TSM). The temperature is assumed at $T = 300$ K.

Difference between the quantum model and TSM as well as the FD model, however, is expected, due to the very different settings of the models. In the quantum model, the laser field is assumed to be perpendicular to the metal surface, whereas in the other models, the laser incidence (i.e., Poynting vector) is perpendicular to the metal surface. The laser power absorption in the latter case is expected to be significantly higher [128], [129], and therefore can induce more photoelectron emission.

The case of laser field perpendicular to the metal surface may be realized when a linearly

polarized laser, of transverse electromagnetic (TEM) mode, propagates along the metal surface (i.e., parallel incidence). In this case, the laser power absorption coefficient is found to be $P_{absorption}/P_{incident} = \pi\delta_s/\lambda$ [128]–[130], where λ is the laser wavelength in vacuum, and $\delta_s = \sqrt{2/\sigma\omega\mu_0}$ is the skin depth, with σ being the conductivity of the metal, and μ_0 the vacuum permeability. By replacing $(1-R)$ with $\pi\delta_s/\lambda$ in Eqs. (2.12) and (14), the TSM and FD model for parallel incidence become, respectively,

$$QE = \left(\frac{\pi\delta_s}{\lambda}\right) F_{e-e} \frac{E_F + \hbar\omega}{2\hbar\omega} \left(1 - \sqrt{\frac{E_F + W}{E_F + \hbar\omega}}\right)^2, \qquad \text{TSM for parallel incidence,} \qquad (2.16)$$

$$QE = a_1 \left(\frac{\pi\delta_s}{\lambda}\right) AT^2 F\left(\frac{\hbar\omega - W}{k_B T}\right), \qquad \text{FD model for parallel incidence,} \qquad (2.17)$$

where the resulted QE from both models is very close to that of the quantum model, Eq. (2.10), as shown in Figs. 2.9c and 2.9d. The difference between the quantum model and the other models for parallel incidence could be partially explained by the assumption in the quantum model that the laser field is terminated abruptly on the metal surface, where the finite penetration of the laser field and the electron-electron scattering effect inside the metal are ignored. These volume effects become important when the laser photon energy is larger than the work function of the metal [131]. It is important to note that the QE calculation from the quantum model in Fig. 2.9 is only for a relatively small laser field (0.01 V/nm). Larger laser field increases QE in the longer laser wavelength range, as already displayed in Fig. 2.8, which cannot be predicted from either TSM or the FD model.

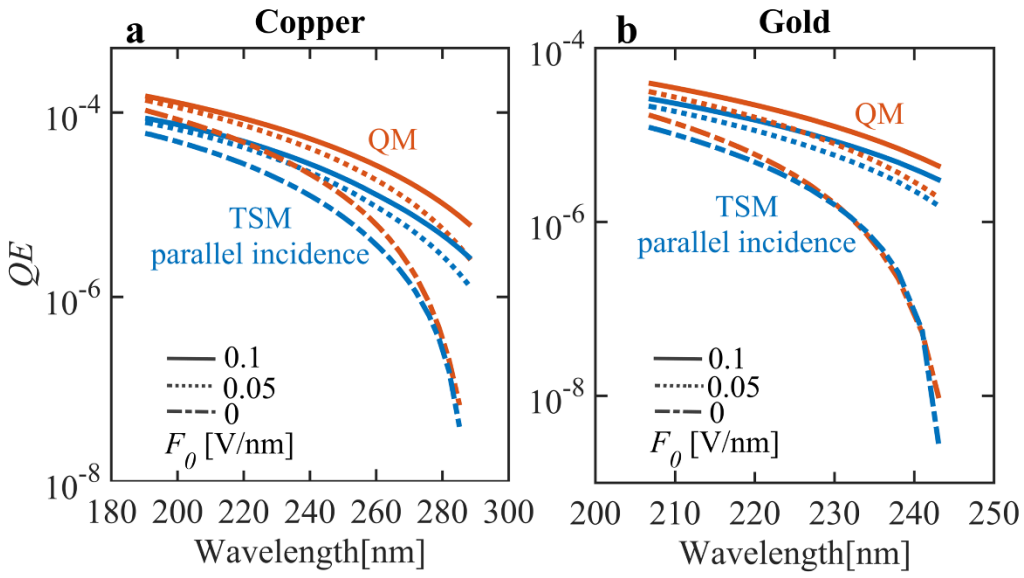

Figure 2.10 Quantum efficiency (QE) from QM (Eq. 2.10) and TSM for parallel incidence (Eq. 2.16) under different dc fields F_0. The other parameters are the same as in Fig. 2.9.

Figure 2.10 shows the comparison of QE from our quantum model and from the TSM for parallel incidence, for both copper and gold under small dc fields (i.e., $F_0 = 0.05$ V/nm and 0.1 V/nm, respectively). The scaling of the results is in good agreement. Similar to Figs. 2.6 and 2.8, QE increases as dc field increases, especially in the longer laser wavelength, due to the combined effects of potential barrier lowering and narrowing by the dc bias. Both effects are captured in the quantum model, but only the barrier lowering effect (or Schottky effect) is included in the TSM model, leading to a higher QE from the quantum model.

2.5 Concluding Remarks

In this chapter, we present a quantum model for photoemission from biased metal surfaces under the excitation of a perpendicular laser field, by solving the time-dependent Schrödinger equation exactly. The electron energy states distribution inside the metal are assumed to follow the Fermi-Dirac distribution.

When the laser photon energy is larger than the work function of the metal, the electron emission process is dominated by single photon absorption. Electrons are predominantly emitted from the initial energy levels in the range within one photon energy below the Fermi level. When the laser field is small, QE is independent of the laser field strength. However, when the laser field increases ($\geq$ 0.1 V/nm), QE increases with laser field strength in the longer laser wavelength range, which is due to the increased contributions from multiphoton absorption processes. This laser field- (or intensity-) dependent QE are not predicted by the pre-existing

photoemission models, such as the three-step model or Fowler-DuBridge model. It is also found that applying a dc field can increase photoelectron emission, especially in the longer laser wavelength range, which agrees with previous studies [38], [43], [44], [91], [92].

A comparison of QE by the quantum model and the existing classical models, i.e., the three-step model, the Fowler-DuBridge model and the Monte Carlo simulation, shows the scaling of the QE by those models agrees well, despite the very different settings and assumptions used in the quantum model and the classical models. The QE from the quantum model can be fitted to that of the three-step model by a constant of proportionality, which counts mainly for the different laser (or photon) absorption coefficient under different configurations. By using the laser power absorption coefficient for parallel incidence on the cathode surface, the QE from the classical models and the quantum model are in good agreement.

We would like to emphasize again that the calculation presented in this chapter is only for a limited range of laser wavelengths when the photon energy is close to the work function of the metal, so that single photon absorption dominates the electron emission process. The work may be extended to the multiphoton emission and optical field emission regimes [38], [49], [132] in a much wider range of laser wavelengths. In these regimes, our model will be compared with the more general formalism of TSM [126] to examine the increasingly important effects of multiple scattering, transverse energies, and multiphoton absorption processes.

For the single photon dominated electron emission studied here, it is found that higher temperature increases the emission current only in the longer wavelength ranges under steady state. It is important to note that, however, laser heating of electron gas and the cathodes is a time-dependent process. Also, high laser intensities (or laser fields) are often realized using femtosecond laser pulses without damaging the metal sample [132]–[134]. Due to the large difference between heat capacity of electrons and phonons, as well as picosecond-scaled electron-phonon scattering, there is a thermal nonequilibrium between electrons and the lattice [58], [135], [136], where the temperature of the electrons can reach up to thousands of kelvin [136], [137]. It also takes as long as ~1 ps for the electrons to reach a thermal equilibrium by electron-electron scattering, depending on the incident laser intensities [60]. Therefore, the electron system consists of both thermal electrons and non-thermal electrons [60], where the Fermi-Dirac electron distribution may not be valid. This in turn is expected to change the step-like characteristics in electron distribution (e.g., Fig. 2.5) by having the photo-excitation occur

from a significantly heated electron gas [136]. Consistent calculations of the time-evolved temperature of the electrons and lattice, electron distribution, and electron emission will be the subject of future study.

CHAPTER 3 EFFECTS OF LASER WAVELENGTH AND LASER HEATING ON PHOTOEMISSION FROM BIASED METAL SURFACES

This chapter is based on the published journal paper "Quantum efficiency of photoemission from biased metal surfaces with laser wavelengths from UV to NIR," *J. Appl. Phys.*, vol. 130, no. 6, p. 064902, Aug. 2021, doi: 10.1063/5.0059497, by **Yang Zhou** and Peng Zhang.

3.1 Introduction

Photoemission processes have been studied extensively over a wide range of laser wavelengths, both experimentally and theoretically. Single-photon photoemission process and the nonlinearity in strong laser intensity range due to the laser heating effect have been observed in the ultraviolet (UV) wavelength range for various metallic cathodes [41]–[44], [138]. Laser of wavelength around 800 nm has been widely used, and multiple photoemission mechanisms, including multiphoton absorption, above-threshold photoemission, photo-assisted field emission, and optical field tunneling [33], [38], [45], [91], [120], [139], [140] have been reported. With laser wavelengths from 1 μm to 1.5 μm, Park *et al.* [48] observed the narrowing of the emission cone angle of the fastest electrons when laser intensity increases, which is ascribed to field-induced steering of sub-cycle electrons. Few-cycle midinfrared (up to 8 μm) laser pulses are applied to single plasmonic nanotips, and it is found that electrons can escape the local field within a fraction of an optical half-cycle [49]. Single-cycle terahertz pulses have also been demonstrated to have their capacity to control nanotip photoemission electron dynamics [50].

Classical models, such as, the three-step model and the Fowler-DuBridge model [43], [44], [110]–[112], [114]–[117], mainly focus on single-photon (or photon energy $\hbar\omega >$ work function W, mostly in UV) photoemission. Fowler-DuBridge model has also been extended to include multiphoton emission and photo-thermionic emission processes [113], [141]–[144], however, the multiphoton emission coefficients typically require empirical fitting, and the model's validity is questionable when applying to strong-field regimes [104]. Yalunin et al. [119] theoretically treat photoemission from metal surfaces, by perturbation theory, the Floquet method, and the Crank-Nicolson numerical approach. Despite extensive studies on photoemission by lasers of a wide wavelength range, there is still lack of systematic analysis on the effects of laser wavelength on photoemission and the corresponding quantum efficiency.

In this chapter, we study the photoemission current and quantum efficiency over a wide range of laser wavelengths from 200 nm to 1200 nm, using a recent quantum model based on the

exact solution of time-dependent Schrödinger equation [125], which has been presented in chapter 2. We examine the laser heating effects on photoemission by using the two-temperature model (TTM) [58], [145], in which electrons and the lattice are treated in separate thermal equilibrium and are characterized by their own temperatures. TTM is found to be suitable for laser pulses on a time scale of a few hundreds of femtoseconds to tens of picosecond [41], [42], [146]–[149]. Our results show that the laser heating induced electron redistribution can enhance photoemission quantum efficiency, especially at laser wavelengths where the ratio of work function of cathode to photon energy is close to an integer.

3.2 Effects of Laser Wavelength on Photoemission

Figure 3.1 shows the time-averaged transmission probability $w_n(\varepsilon = E_F)$ through the *n*th channel (or *n*-photon process), under various combinations of dc electric field F_0, laser electric field F_1, and laser wavelength λ $(= 2\pi c/\omega)$. The metal is assumed to be gold, with Fermi energy of $E_F = 5.53$ eV and work function of $W_0 = 5.1$ eV. Unless specified otherwise, these are the default cathode properties in this chapter. The laser wavelengths are 200, 400, 800, and 1200 nm, corresponding to the photon energy of 6.20, 3.10, 1.55, and 1.03 eV, respectively. The laser fields F_1 for lines in red, green, blue, and purple are 0.1, 1, 3, and 6 V/nm, corresponding to the local laser intensity of 1.33×10^9, 1.33×10^{11}, 1.20×10^{12}, and 4.79×10^{12} W/cm^2, respectively. The electron initial longitudinal energy is assumed to be at the Fermi level, *i.e.*, $\varepsilon = E_F$. It is obvious that the electron transmission probability $w(E_F)$ increases when the laser field increases. For $F_1 = 6$ V/nm, there is more contribution from the large values of *n*th channel to the total transmission probability, especially for the cases of $\lambda = 800$ and 1200 nm. When $F_0 = 0$, the dominant emission process for $\lambda = 200$, 400, 800, and 1200 nm are one-, two-, four-, and five-photon absorption processes, respectively. This is consistent with the integer value of $\langle W/\hbar\omega + 1\rangle$, with $\langle\ \ \rangle$ denoting the integer part of the expression. It is interesting to observe that the dominant channel shifts from $n = 5$ to $n = 6$ for $\lambda = 1200$ nm, when F_1 increases to 3 and 6 V/nm (Fig. 3.1(d)), due to the channel closing effect [150], where the to-be-liberated electrons have to overcome not only the potential barrier but also the ponderomotive energy $U_p = e^2F_1^2/4m\omega^2$ in the laser field [33] such that the electron drift kinetic energy $E_n = \varepsilon + n\hbar\omega - E_F - W - U_p$ is larger than zero. A small dc field $F_0 = 0.1$ V/nm has little effect on the transmission probability for $\lambda = 200$ and 400 nm (Figs. 3.1(e) and 3.1(f)). However, it shifts the

dominant channel from $n = 4$ to $n = 3$ for $\lambda = 800$ nm when $F_1 = 0.1$, 1, and 3 V/nm (Fig. 3.1(g)), and also shifts the dominant channel from $n = 6$ to $n = 5$ for $\lambda = 1200$ nm when $F_1 = 3$ and 6 V/nm (Fig. 3.1(h)). This is due to the lowering of the surface potential barrier by the dc electric field, and therefore lowering the number of photons required to overcome the barrier. When $F_0 = 1$ V/nm, more *n*th channels of lower order are opened up, and the dominant channel is further shifted to smaller value of *n*th channels, especially for $\lambda = 400$, 800, and 1200 nm (Figs. 3.1(j) – 3.1(l)). When $F_0 = 5$ V/nm, the dominant emission process is direct field tunneling, *i.e.*, through $n = 0$, regardless of the laser wavelength.

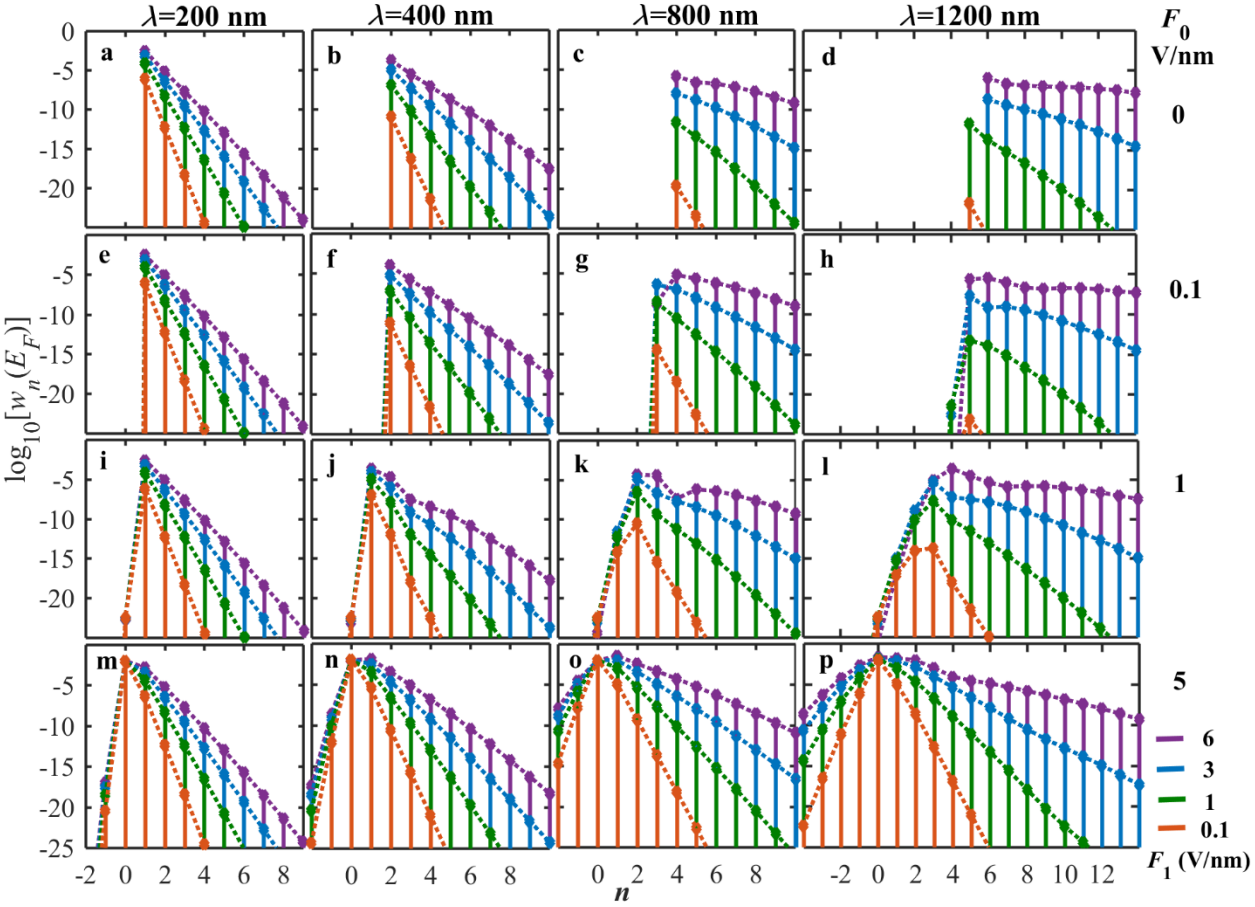

Figure 3.1 Electron transmission probability from $\varepsilon = E_F$ through *n*th channel, under various combinations of dc electric field F_0, laser field F_1 and laser wavelength λ. (a) – (d) $F_0 = 0$ V/nm; (e) – (h) $F_0 = 0.1$ V/nm; (i) – (l) $F_0 = 1$ V/nm; and (m) – (p) $F_0 = 5$ V/nm. In each column, (a), (e), (i), (m) $\lambda = 200$ nm; (b), (f), (j), (n) $\lambda = 400$ nm; (c), (g), (k), (o) $\lambda = 800$ nm; and (d), (h), (l), (p) $\lambda = 1200$ nm. F_1 corresponding to lines in red, green, blue, and purple, are 0.1, 1, 3, and 6 V/nm, respectively. The metal is gold, with $E_F = 5.53\ eV$ and $W_0 = 5.1\ eV$.

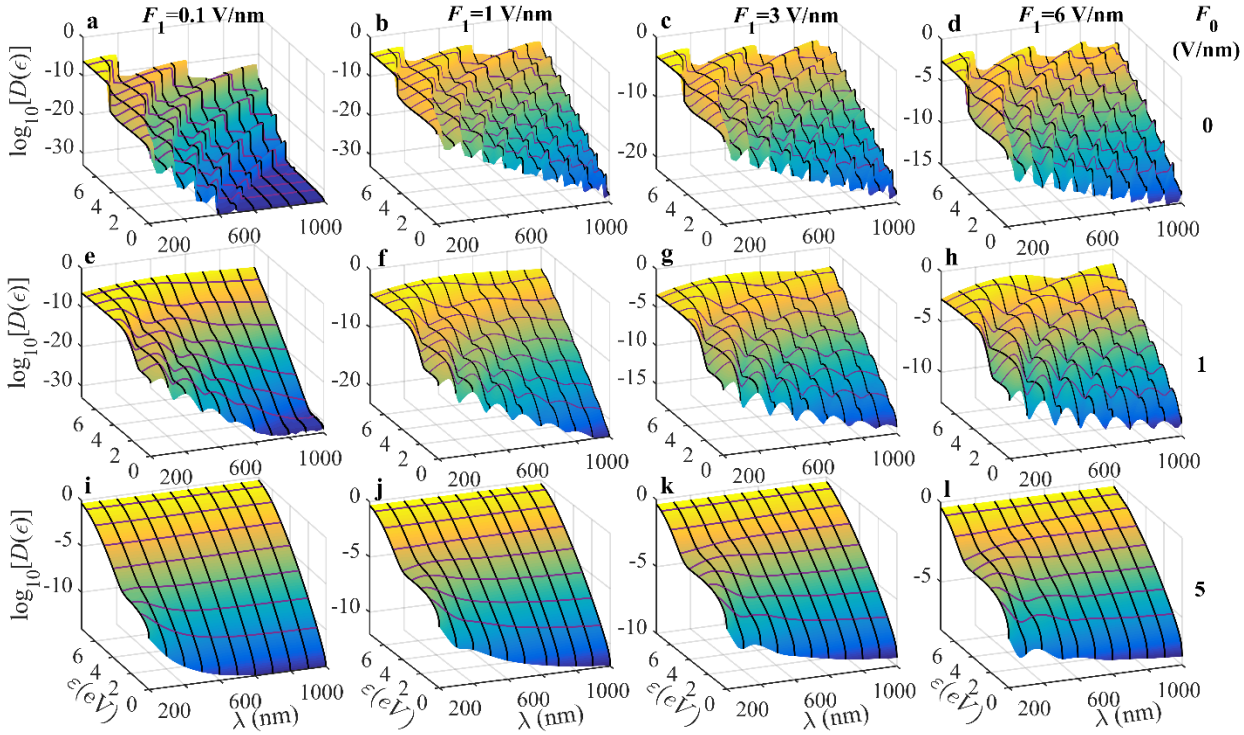

Figure 3.2 Electron transmission probability $D(\varepsilon)$ as a function of electron initial energy ε and laser wavelength λ, for various combinations of laser field F_1 and dc electric field F_0. (a) – (d) $F_0 = 0$ V/nm; (e) – (h) $F_0 = 1$ V/nm; (i) – (l) $F_0 = 5$ V/nm. In each column, (a), (e), (i) $F_1 = 0.1$ V/nm; (b), (f), (j) $F_1 = 1$ V/nm; (c), (g), (k) $F_1 = 3$ V/nm; (d), (h), (l) $F_1 = 6$ V/nm.

The electron transmission probability $D(\varepsilon)$ as a function of electron longitudinal energy ε and laser wavelength λ, under various combinations of dc electric field F_0 and laser field F_1, is shown in Fig. 3.2. When $F_0 = 0$, the three-dimensional (3D) surface plot shows stair-like behavior as a function of ε for a given λ (Figs. 3.2(a)–3.2(d)). Each stair corresponds to *n*-photon absorption process, with *n* increasing as ε decreases, for a given λ. As F_1 increases, the electron transmission probability increases and more "stairs" clearly appear at the bottom right region, *i.e.*, the "smaller initial energy"-"longer laser wavelength" region. When $F_0 = 1$ V/nm, the electron transmission probability is increased due to the lowering of the surface potential barrier. The step edge between "stairs" is not as steep as that with zero dc field but becomes gradual (Figs. 3.2(e)–3.2(h)). Dc electric field has a greater enhancement on the emission induced by a longer wavelength laser [125]. This can be explained by the change of the dominant emission process, which shifts to smaller *n*-photon absorption process due to the lowering of the surface potential barrier by the applied dc field. From Figs. 3.1(a)–3.1(d), it can be observed that the (*n*+1)-photon absorption process has a probability orders of magnitude lower than the *n*-photon absorption

process, for a given λ. When $F_0 = 5$ V/nm, the 3D surface plot of $D(\varepsilon)$ becomes smooth (Figs. 3.2(i)-3.2(l)). At each electron initial longitudinal energy ε, $D(\varepsilon)$ is almost constant for all different laser wavelengths, which implies that the dominant emission process is due to the dc field tunneling, consistent with Figs. 3.1(m)-3.1(p). In Figs. 3.2(i)–3.2(l), as the laser field F_1 increases from 0.1 V/nm to 6 V/nm, $D(\varepsilon)$ increases and the stair shape of the surface in the shorter wavelength range becomes more obvious. The shape of the 3D surfaces is determined by the relative strength of laser and dc electric fields.

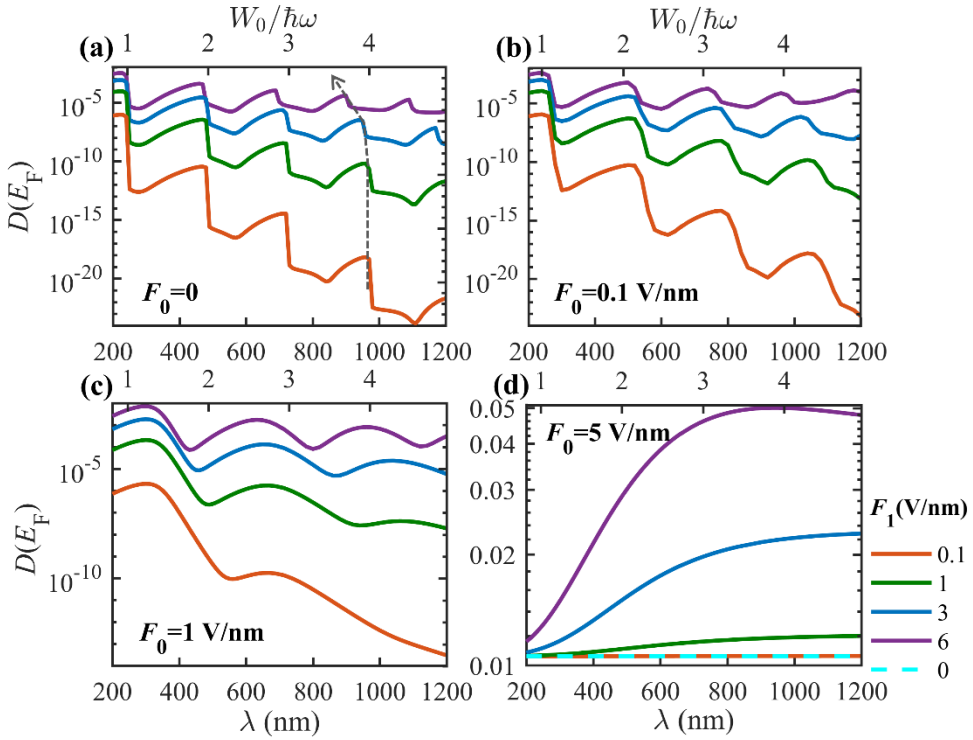

Figure 3.3 Electron transmission probability $D(\varepsilon = E_F)$ with the initial energy of E_F, as a function of laser wavelength λ, for various combinations of dc electric field F_0 and laser field F_1. (a) $F_0 = 0$; (b) $F_0 = 0.1$ V/nm; (c) $F_0 = 1$ V/nm; (d) $F_0 = 5$ V/nm. The laser fields F_1 corresponding to solid lines in red, green, blue, purple, and the dashed line in cyan, are 0.1, 1, 3, 6, and 0 V/nm, respectively.

Figure 3.3 shows the electron transmission probability $D(\varepsilon = E_F)$ as a function of laser wavelength under various combinations of dc and laser electric fields, which is the projection of $D(\varepsilon)$ in the $D - \lambda$ plane with $\varepsilon = E_F$ in Fig. 3.2. When $F_0 = 0$, the curves display distinct stair shape, though each step is not flat, especially for $\lambda > 486$ nm, *i.e.*, $n = W_0/\hbar\omega > 2$. For small F_1, $D(E_F)$ has its maximum value at the step point in each step, corresponding to an integer value of the ratio of $\langle W_0/\hbar\omega + 1\rangle$. As the laser field F_1 increases, $D(E_F)$ is enhanced greatly, especially for $\lambda > 486$ nm. This is because $D(\varepsilon = E_F) \propto F_1^{2n}$ in the n-photon photoemission

regime. Meanwhile, the step points shift to smaller laser wavelength when F_1 gets larger, which is indicated by the dashed arrow line in Fig. 3.3(a). This shift is due to the channel closing effect, which is more pronounced for longer laser wavelengths. When there is a dc electric field but small ($F_0 = 0.1$ V/nm), the "stair" becomes smoother. The step points shift to larger wavelength (i.e., smaller photon energy) due to the lowering of the surface potential barrier by the applied dc electric field. As F_0 increases to 1 V/nm, the "stairs" still exist but the number of the "stairs" decreases and the magnitude difference between them gets smaller. When $F_1 = 0.1$ V/nm, there are two distinct "stairs" observed. Most of the emission is due to photon-assisted tunneling (*cf.* Figs. 3.1(k) and 3.1(l)) for relatively long laser wavelength. When $F_0 = 5$ V/nm, the electron transmission probability becomes almost independent of laser wavelength for $F_1 = 0.1$ V/nm. The dashed curve is for dc field emission without laser electric field with $F_0 = 5$ V/nm, which overlaps with the curve for $F_1 = 0.1$ V/nm. For $F_1 \geq 1$ V/nm, the dominant emission process is still direct tunneling, as shown in Figs. 3.1(m) – 3.1(p). The laser electric field F_1 can modulate the emission process through photo-assisted field emission and above-threshold photoemission. It can be observed that, with a large dc field, $D(E_F)$ is larger in the relatively longer laser wavelength range, as shown in Fig. 3.3(d).

The emission current density J, calculated from Eq. (2.9), as a function of laser wavelength λ, is presented in Fig. 3.4. It should be pointed out that the laser heating effect is not considered here, with the temperature T in Eq. (2.9) set to 300 K. Figure 3.4 shares similar trends as in Fig. 3.3, since the majority of emitted electrons originate from the vicinity of the Fermi level [33], [125]. However, the curves for J vs λ are smoother than those for $D(\varepsilon = E_F)$ vs λ, due to the combined emitted electrons with different initial longitudinal energies. Including a dc field will make the step edge smoother and the step point shift towards longer laser wavelength. When $F_0 = 5$ V/nm, the electron emission is increased by 1 ~ 21 orders of magnitude compared with the case of no applied dc electric field, for different combinations of laser wavelength λ and laser field F_1. The dominant emission process of field emission ($n = 0$) for $F_0 = 5$ V/nm makes the emission current insensitive to the laser wavelength.

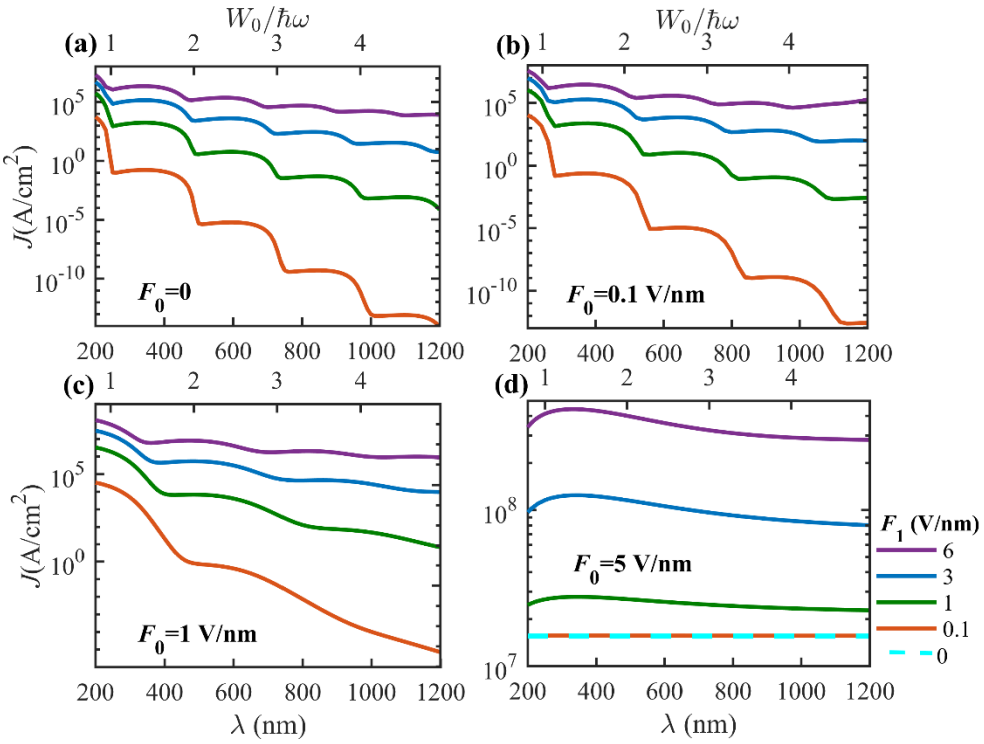

Figure 3.4 Electron emission current density, calculated from Eq. (2.9) as a function of laser wavelength λ, for various combinations of dc electric field F_0 and laser field F_1. The temperature T is set to be constant at 300 K, without considering laser heating. (a) $F_0 = 0$; (b) $F_0 = 0.1$ V/nm; (c) $F_0 = 1$ V/nm; (d) $F_0 = 5$ V/nm. The laser fields F_1 corresponding to solid lines in red, green, blue, purple, and the dashed line in cyan, are 0.1, 1, 3, 6, and 0 V/nm, respectively.

Figure 3.5 shows quantum efficiency (QE) as a function of laser wavelength λ under various laser field strengths F_1 and dc field strengths F_0, which is calculated from Eq. (2.10). It is obvious that the curves for QE vs λ shares similar trends as those for J vs λ in Fig. 3.4. For $F_0 \leq 1$ V/nm, QE is almost independent of F_1 for different laser fields $0.1\ \mathrm{V/nm} \leq F_1 \leq 6\ \mathrm{V/nm}$ in the smaller laser wavelength regime (or $W/\hbar\omega < 1$), which is indicated by the yellow shaded area in Figs. 3.5(a)-(c). This is because the dominant single-photon photoemission in this regime follows $J \propto I$. Therefore, the quantum efficiency is independent of the laser field as $QE \propto J/I$. Note the majority of existing studies on QE focus only on this single-photon regime [43], [44], [125]. For $W_0/\hbar\omega > 1$, the photoemission is due to n-photon process, which scales as $J \propto I^n$ ($n \geq 2$), with n determined by rounding $W/\hbar\omega$ up to the nearest integer number. As a result, $QE \propto I^{n-1}$, and the quantum efficiency increases greatly as F_1 increases. As dc field increases, QE is enhanced and the step points are shifted towards longer laser wavelengths (i.e., smaller photon energy), due to the lowering of the surface potential barrier by the dc field. As a result, increasing F_0 from 0 to 1 V/nm, also extends the single-photon absorption regime from ~250 nm

to ~320 nm, where QE is independent of laser field F_1, as indicated by the yellow shaded area in Figs. 3.5(a)-(c). When $F_0 = 5$ V/nm (Fig. 3.5(d)), QE can be larger than 1, due to the dominant contribution of dc field emission.

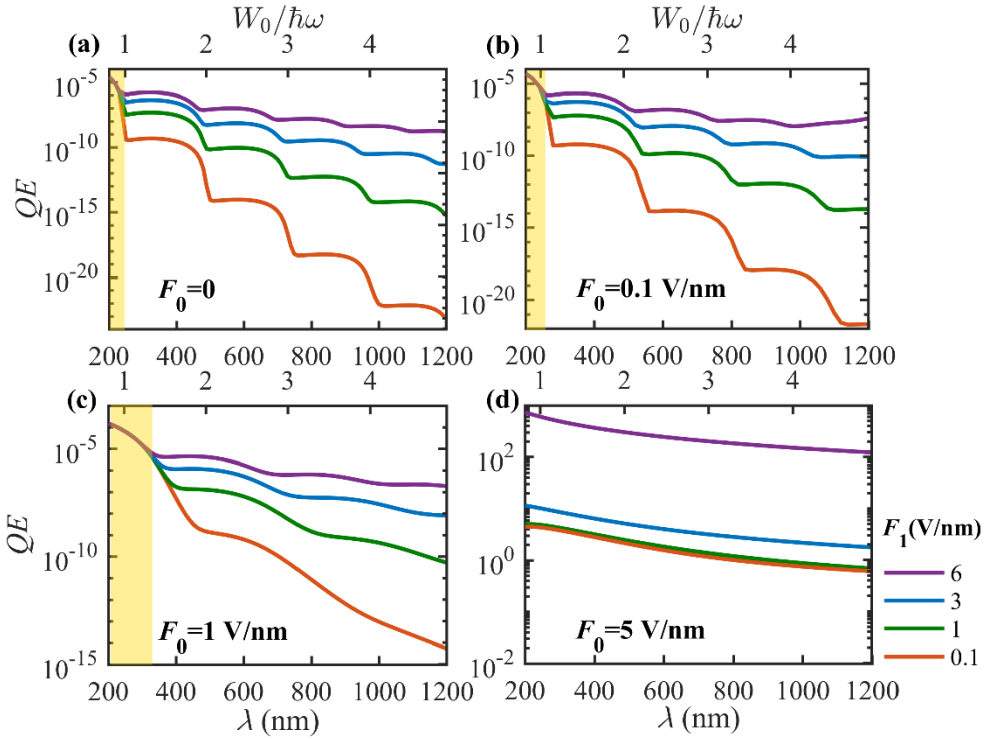

Figure 3.5 Quantum efficiency (QE), calculated from Eq. (2.10) as a function of laser wavelength λ, for various combinations of dc electric field F_0 and laser field F_1. The temperature is set to be constant at 300 K, without considering laser heating. (a) $F_0 = 0$; (b) $F_0 = 0.1$ V/nm; (c) $F_0 = 1$ V/nm; (d) $F_0 = 5$ V/nm. The laser fields F_1 corresponding to solid lines in red, green, blue, and purple are 0.1, 1, 3, and 6 V/nm, respectively.

3.3 Laser Heating Effects

3.3.1 Two-Temperature Model

It is known that electron energy distribution function (EEDF) and its dynamic due to laser heating have strong influence on photoelectron emission current and emission electron energy spectrum [41], [42], [63], [125], [145]. Electrons can be excited to higher energy levels by absorbing the laser energy. The excited electrons can come into thermal equilibrium with other electrons by electron-electron scatterings, and can transfer energy to the lattice by electron-phonon scatterings. The microscopic kinetic approach, such as Boltzmann's equation, can provide an accurate estimation of internal thermalization process and electron and phonon energy distribution, especially for femtosecond laser pulses [62], [120], [151]. However, the classical two-temperature model (TTM) still works well for a laser pulse of ~500 fs duration [41], [42],

[146]–[149], but with much lower computational complexity. We use TTM to estimate the laser heating effects in photoemission. In TTM [58], [135], electrons and lattice are considered as two separate equilibrium subsystems, characterized by their own temperatures T_e and T_l,

$$C_e(T_e)\frac{\partial T_e(x,t)}{\partial t} = \frac{\partial}{\partial x}\kappa\frac{\partial T_e(x,t)}{\partial x} - g(T_e - T_l) + G(x,t), \tag{3.1a}$$

$$C_l(T_l)\frac{\partial T_l(x,t)}{\partial t} = g(T_e - T_l). \tag{3.1b}$$

In Eq. (3.1), the electron heat capacity $C_e(T_e) = \gamma T_e / \left[1 + \frac{7}{40}\left(\frac{\pi k_B T_e}{E_F}\right)^2\right]$ with k_B being the Boltzmann's constant, $\gamma = \frac{1}{3}\pi^2 k_B^2 B(\varepsilon = E_F)$ with $B(\varepsilon) = 8\pi\frac{m\eta}{(2\pi\hbar)^3}\sqrt{2m\varepsilon}$ and η an effective thermal mass term. When $k_B T_e \ll E_F$, $C_e(T_e) \approx \gamma T_e$. The lattice heat capacity $C_l(T_l) = 3Nk_B / \left[1 + \frac{1}{20}\left(\frac{T_D}{T_l}\right)^2\right]$, where N is the number density of the atoms in metal, $T_D = \frac{\hbar v_s}{k_B}(6\pi^2 Nr)^{1/3}$ is the Debye temperature, with v_s the speed of sound inside the metal and r the number of atoms per unit cell. When $T_D \ll T_l$, C_l is a constant. $g = \frac{\pi\lambda_0}{9\hbar}k_B k_F^3 m v_s^2$ is the electron-lattice coupling coefficient, where k_F is determined by the Fermi momentum $\hbar k_F = \sqrt{2mE_F}$, λ_0 is a dimensionless electron-phonon coupling constant, which is characteristic of the metal and on the order of 0.1 to 1. $g(T_e - T_l)$ gives the amount of energy per unit volume per unit time transferred between electron and lattice systems. $G(x,t) = I(t)P_{abs}\alpha\exp(-\alpha x)$ is the energy absorbed by the metal, where $I(t)$ is the laser intensity temporal profile, $\alpha = 4\pi k/\lambda$ is the absorption coefficient with k the extinction coefficient, $P_{abs} = \pi\delta_s/\lambda$ is the laser power absorption coefficient for the parallel-to-surface incident laser [128]–[130], with λ the laser wavelength in the vacuum and $\delta_s = \sqrt{2/\sigma\omega\mu_0}$ the skin depth, σ the conductivity of the metal, and μ_0 the vacuum permeability, or $P_{abs} = 1 - R$ for the incident laser tilted to the metal surface, with R the reflectivity of the laser at the metal surface. $\kappa = \frac{2E_F}{3m}C_e(T_e)\tau$ is the thermal conductivity, with τ the electron scattering time and m the electron rest mass. According to Matthiessen's rule, $\frac{1}{\tau} = \frac{1}{\tau_{e-e}} + \frac{1}{\tau_{e-ph}}$, with $\tau_{e-e} = \frac{\hbar E_F}{A_0 k_B^2}\frac{1}{T_e^2}$ and $\tau_{e-ph} = \frac{\hbar}{2\pi k_B\lambda_0}\frac{1}{T_i}$ the electron-electron and electron-phonon scattering times respectively, and A_0 a dimensionless, material-specific quantity.

3.3.2 Electron Temperature T_e

The time-dependent evolution of the electron temperature in response to an incident laser pulse with full width at half maximum (FWHM) $\tau_{FWHM} = 450$ fs under various laser wavelengths and field strengths is shown in Figs. 3.6(a) and 3.6(b). In Fig. 3.6(a), the laser field strength is kept constant as $F_1 = 1$ V/nm for laser wavelengths ranging from 200 nm to 1200 nm. The maximum of the electron temperature lags behind that of the incident laser intensity (dotted curve), which is centered at $t = 0$. It is interesting to find that as the laser wavelength decreases, the time delay between the maximum of the temperature and that of the laser intensity increases, and the temperature gets larger, which is due to larger laser energy absorption $G \sim k/\lambda^{3/2}$ inside the metal for parallel incidence (extinction coefficient k vs λ shown in Fig. 3.6(c)). For a fixed laser wavelength ($\lambda = 800$ nm), the electron temperature increases with the laser field strengths, as shown in Fig. 3.6(b). In addition, the time delay between the maximum of the electron temperature and that of the laser intensity increases. The electron temperature at $t = 0$, which corresponds to the peak of the laser intensity, and the peak electron temperature T_e^{peak}, as a function of laser wavelength are shown in Fig. 3.6(d) for $F_1 = 1$ V/nm. The temperature decreases with the laser wavelength, which is due to the increased time delay and less absorption of the laser energy as laser wavelength increases. The obtained electron temperature T_e is then used in Eq. (2.9) by setting $T = T_e$ to calculate the photoemission current density.

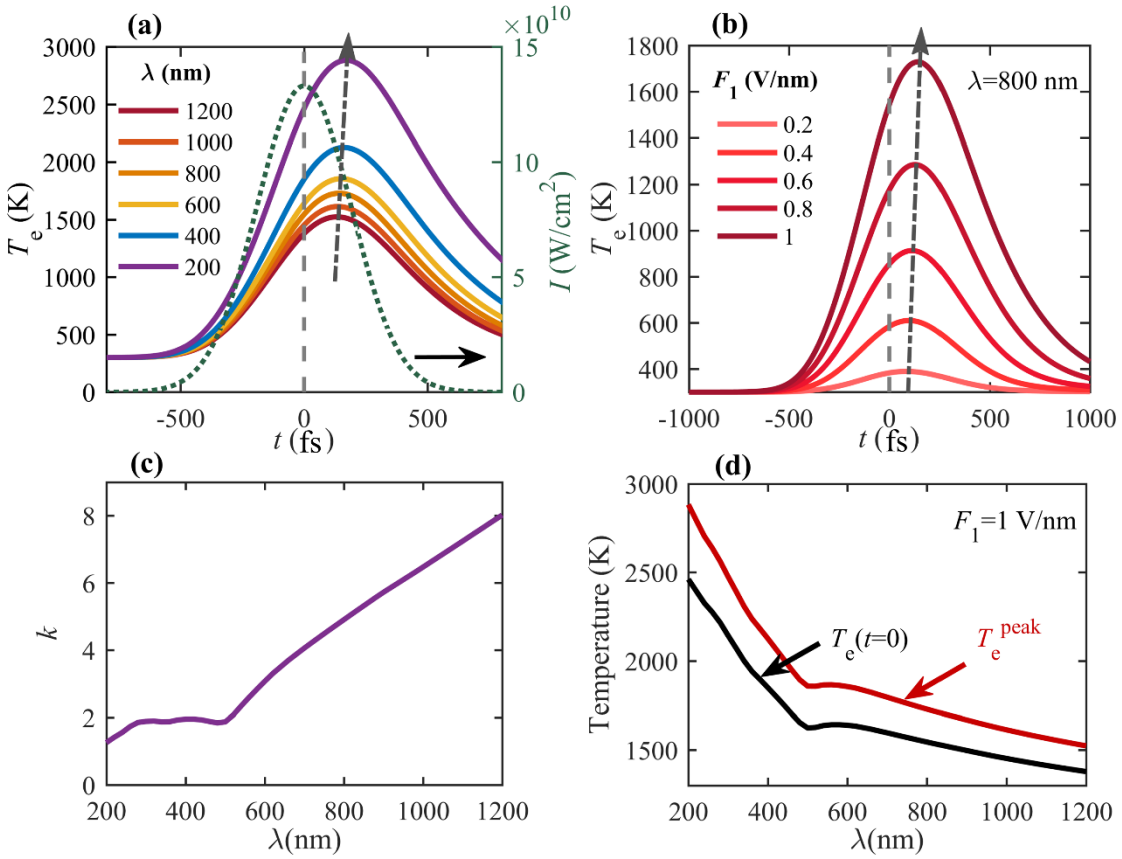

Figure 3.6 Electron temperature varies with incident laser wavelength λ and laser field strength F_1 calculated from Eq. (3.1). (a) Electron temperature temporal profile for λ from 200 nm to 1200 nm with peak laser field $F_1 = 1$ V/nm and the corresponding peak laser intensity of 1.33×10^{11} W/cm^2. The dotted curve is the laser intensity temporal profile $I(t)$. (b) Electron temperature temporal profile for peak laser field F_1 from 0.2 V/nm to 1 V/nm with $\lambda = 800$ nm. (c) Optical constant extinction coefficient k as a function of λ [152]. (d) Electron temperature at $t = 0$ (black curve), which corresponds to the time instant of peak laser intensity, and peak electron temperature T_e^{peak} (red curve), as a function of λ. Parameters in Eq. (3.1) for gold are $\eta = 1.08$, $C_l = 2.35 \times 10^6$ J/m^3/K (assumed constant), $v_s = 3240$ m/s, $\sigma = 4.11 \times 10^7$ S/m, $A_0 = 17$, $\lambda_0 = 0.1548$ [41], [145]. **Erratum**: in ref. [153], *x*-axis label should be *t* (fs) instead of *t* (ps).

3.3.3 Current Density and Quantum Efficiency with Laser Heating

A comparison of photoemission with laser heating effects (red curves) and without laser heating effects (blue curves, with $T = T_e \equiv 300$K) is shown in Fig. 3.7. The results are taken at *t* = 0, which corresponds to the laser intensity peak (cf. the dotted curve in Fig. 3.6(a)). The peak laser field strength is taken to be 1 V/nm. The electron emission current density per electron initial energy, calculated as $J(\varepsilon) = eD(\varepsilon)N(\varepsilon)$ from Eq. (2.10), extends to energy levels above the Fermi level as the laser heating effect is considered, as shown in Fig. 3.7(a) for λ = 200 nm,

600 nm, and 1000 nm. This is because more electrons are thermalized to energy levels above the Fermi level by absorbing the laser energy. The electron emission from initial energy levels above the Fermi energy accounts for 7.84%, 6.85%, and 91.1% of the total emission for $\lambda = 200$ nm, 600 nm, and 1000 nm, respectively, with laser heating effects, compared to 0.13%, 0.015%, and 0.73% without laser heating. Figure 3.7(b) shows the emission current density as a function of the laser wavelength. The steep step point, which is the transition point between different n-photon processes, becomes smooth. This is because more electrons above the Fermi level can be emitted through smaller n-photon process, which has an emission probability orders of magnitude higher than larger n-photon process (see Figs. 3.1(a)-(d) and its description in section 3.2). The difference between the red and blues curves shows that laser heating effect has a greater impact on longer wavelength laser-induced photoemission. The quantum efficiency as a function of laser wavelength is shown in Fig. 3.7(c), showing the same trend as J vs λ in Fig. 3.7(b). In summary, the increase of QE due to laser heating is the strongest near the step points (i.e., $W_0/\hbar\omega =$ integer) and is more profound for longer laser wavelengths.

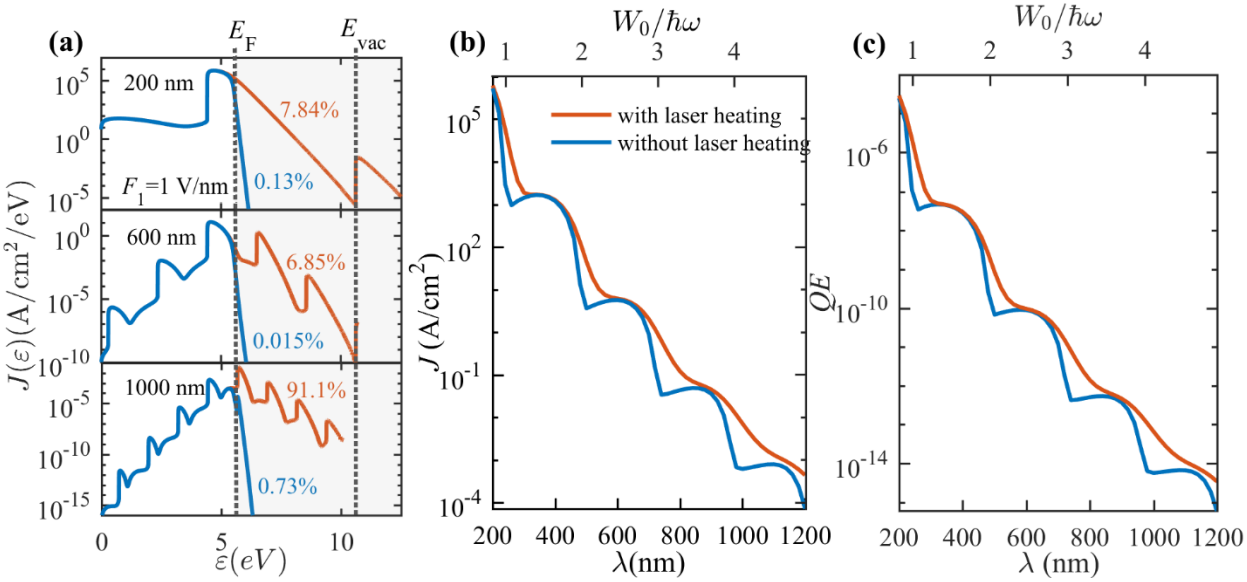

Figure 3.7 Laser heating effects on photoemission. (a) Electron emission current density per electron initial energy at $t = 0$ for $\lambda = 200$ nm, 600 nm, and 1000 nm, with $F_1 = 1$ V/nm and $F_0 = 0$; (b) Electron emission current density and (c) QE at $t = 0$ as a function of laser wavelength for $F_1 = 1$ V/nm and zero dc field $F_0 = 0$.

3.3.4 Comparison with Experimental Results

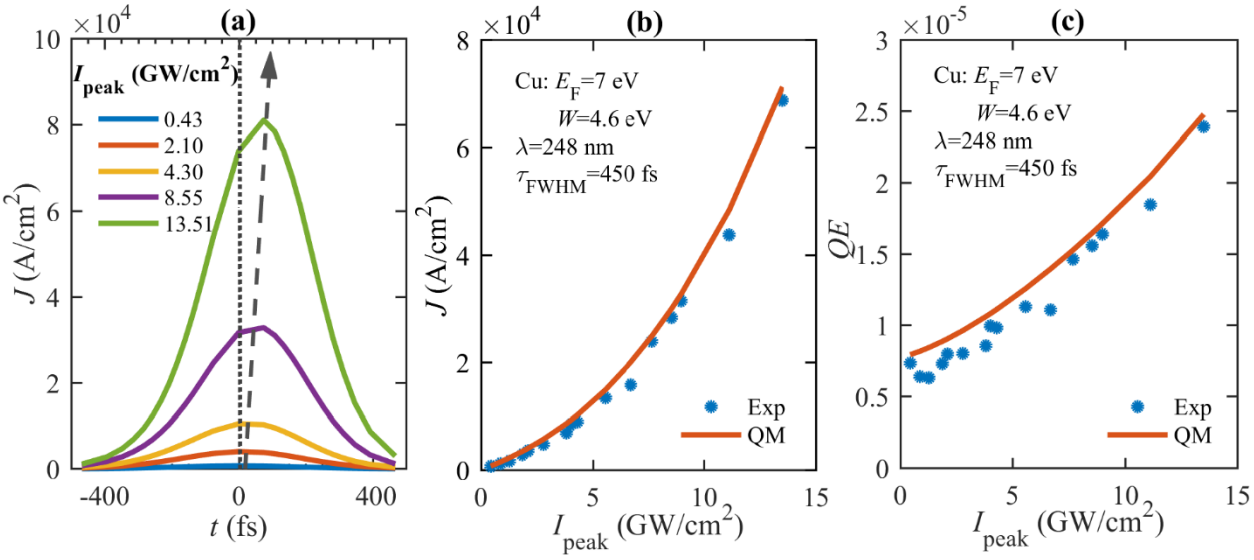

Figure 3.8 Comparison with experimental results. (a) Calculated emission current density temporal profile for various laser intensities used in the experiment [41]. (b) Emission current density as a function of the peak laser intensity. Scatters are experimental data extracted from [41]. The red curve is calculated from Eq. (3.2) with $J(t)$ calculated by our quantum model. (c) Quantum efficiency as a function of the peak laser intensity. Parameters in Eq. (3.1) for copper are $\gamma = 96.6\ \mathrm{J/K^2/m^3}$, $C_l = 3.5\times10^6\ \mathrm{J/m^3/}K$ (assumed constant), $v_s = 5010\ \mathrm{m/s}$, $\sigma = 5.96\times10^7\ \mathrm{S/m}$, $A_0k_B^2/\hbar E_F = 2.3\times10^7/(\mathrm{K^2 s})$, $2\pi k_B\lambda_0/\hbar = 1.1\times10^{11}/(\mathrm{K^2 s})$ [41], [42], [145].

We demonstrate the validity of the above quantum model with laser heating, by comparing it with experimental results in Ref. [41]. In the experiment, a laser pulse of 450 fs duration at 248 nm is used. The metal is copper, with Fermi energy $E_F = 7$ eV and work function $W_0 = 4.6$ eV. The emission current density per pulse based on our quantum model [93], [125] is given as,

$$J_p = \frac{1}{\tau_{FWHM}}\int_{-\infty}^{\infty} J(t)dt\,, \tag{3.2}$$

where $J(t)$ is the emission current density at t calculated from Eqs. (2.8) and (2.9), and τ_{FWHM} is the full-width-half-maximum of the intensity of the laser pulse. Note that though Eq. (2.8) is the time-averaged transmission probability for continuous wave laser excitation, it is found to be an excellent approximation for laser pulses of longer than 10 cycles [38]. Thus, it is expected to be applicable for laser pulses of 450 fs (~ 544 laser cycles) at 248 nm considered here. The temporal profile of the emission current density is shown in Fig. 3.8(a). As the laser intensity increases, the emission current density increases, and the current density peak lags behind the laser intensity peak. This is due to the delay between the temperature peak and the laser intensity peak,

as shown in Figs. 3.6(a) and 3.6(b), which has also been observed in [154]. The calculated current density by the quantum model from Eq. (3.2) is shown as red curve in Fig. 8(b), which is in good agreement with the experimental measured current density shown as blue scatter points in Fig. 3.8(b). The small difference can be ascribed to the different settings of the experiment and our quantum model. In the experiment, the laser field is incident onto the metal surface with an angle of 80° to the normal. However, in our model, the laser field is perpendicular to metal surface (i.e., parallel incidence). For *n*-photon absorption process, the emission current density $J \propto (F_1 \cos\theta)^{2n}$ with θ being the angle between field polarization and the normal of the cathode surface [139]. Therefore, our model slightly overestimates the photoemission. The quantum efficiency is plotted in Fig. 3.8(c). To be consistent with the current density Eq. (3.2), the laser intensity I in Eq. (2.10) is calculated by $I = \int_{-\infty}^{\infty} I(t)\, dt/\tau_{FWHM}$ in order to calculate QE. It is clear that QE increases with the laser intensity instead of being constant (yellow shaded area) as shown in Figs. 3.5(a)–3.5(c), which is ascribed to the laser heating induced electron redistribution.

3.4 Concluding Remarks

In this chapter, we have analyzed photoemission from metal surfaces with the laser wavelength from 200 nm to 1200 nm (i.e., UV to NIR), based on an analytical quantum model by solving the time-dependent Schrödinger equation. The photoemission mechanisms vary from multiphoton absorption to dc or optical field emission, depending on the laser wavelength and intensity, and dc electric field. When $F_0 \leq 0.1$ V/nm, which is much smaller than the typical dc field used in static field emission, the emission current density and quantum efficiency (QE) are characterized by different *n*-photon absorption processes. Channel closing effects and more above-threshold photoemission ($n > W/\hbar\omega$) are observed as the laser field increases, especially for longer wavelengths. It is found that QE in the short wavelength regime (or single-photon regime, $n = 1$) is insensitive to the laser field strength for $F_0 \leq 1$ V/nm. When $F_0 = 5$ V/nm, the static field emission ($n = 0$) becomes dominant, regardless of the laser wavelength ($200\ \text{nm} \leq \lambda \leq 1200\ \text{nm}$) and the laser field strength ($0.1\ \text{V/nm} \leq F_1 \leq 6\text{V/nm}$).

Laser heating induced electron dynamics is considered by using two-temperature model (TTM), which is applicable for sub-picosecond laser pulses. The electron temperature rise shows a strong dependence on the laser wavelength. It is found that QE increases nonlinearly with the laser intensity for sub-picosecond laser pulses. The increase is the strongest near wavelengths

where the work function of the metal is integer multiple of the corresponding photon energy. The quantum model with the laser heating included also reproduces previous experimental results, which further validates our quantum model and the importance of laser heating.

CHAPTER 4 FIELD EMISSION FROM METAL SURFACES WITH NANOSCALE DIELECTRIC COATINGS

This chapter is based on the published journal paper "Theory of field emission from dielectric coated surfaces," *Phys. Rev. Research,* vol. 2, no. 4, p. 043439, Dec. 2020, doi: 10.1103/PhysRevResearch.2.043439, by **Yang Zhou** and Peng Zhang.

4.1 Introduction

Electron field emission [97], [106] attracts intensive attention in many applications, such as, flat panel display [155]–[157], electron microscopes [19], [158], [159], vacuum micro-electronics [160], [161] and emerging nano-devices [27], [28], [109], [162], [163], X-ray sources [164], and high power microwave sources and amplifiers [165]–[172], for its high brightness, low emittance and miniaturized device size [173], [174]. Common challenges of field emission include the operation requirement of high vacuum condition and current instabilities [175], [176]. To overcome these problems, ultra-thin coatings, such as graphene, graphene oxide and zinc oxide [70], [177]–[179], are fabricated onto the emitter to provide chemical and mechanical protection. Coated emitters are demonstrated to not only have longer current stability, but also smaller turn-on electric field (i.e., field at which the cathode starts appreciable electron emission) and enhanced emission current due to the lowering of the effective potential barrier [47], [70], [178]–[181]. In addition to the artificially fabricated coatings, native oxides or foreign adsorbates can be easily formed on the surface of the emitter at low vacuum condition [182]. The thin oxide film or the coated dielectric layer on the cathode surface forms a double-layer potential barrier, which strongly influences the field emission properties. The heterostructure in the emission barrier introduced by the coating also has its potential to change the electrons' mean transverse energy behavior that affects beam quality, which makes it an active area for photoinjectors for future X-ray free electron lasers (XFELs) [69], [78]. A modified Fowler-Nordheim equation was constructed to account for the double-barrier field emission scenario [183], [184]. However, there is still lack of systematic analysis on the parametric scaling of field emission from coated surfaces and comprehensive understanding on the interplay of various parameters to optimize the design of coated field emitters.

In this chapter, we develop a quantum analytical solution for field emission from the dielectric-coated cathode surface, by solving the one-dimensional (1D) time-independent Schrödinger equation subject to the double-barrier introduced by the coating layer. The solution

is applicable for arbitrary electric dc field, cathode properties (i.e., work function and Fermi level) and dielectric coating properties (i.e., dielectric constant, electron affinity and thickness). It includes not only field emission but also thermionic emission. The model predicts that for 1D flat surfaces, coatings of small dielectric constant and large electron affinity tend to enhance the field emission current, which provides insights for the design of a stable and efficient field emitter.

4.2 Analytical Model

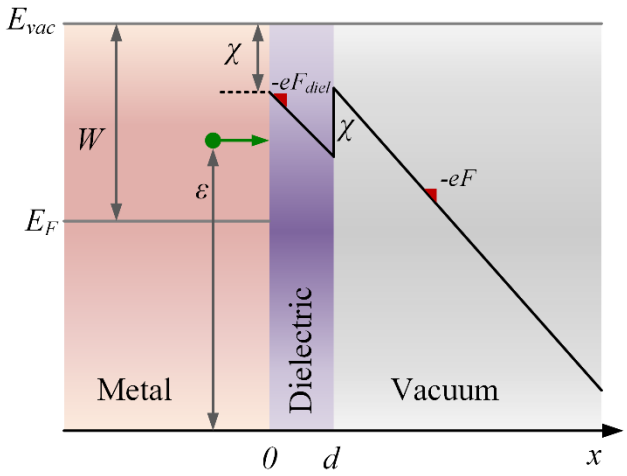

Figure 4.1 Field emission from a metal surface coated with a dielectric. The metal-dielectric interface is located at $x = 0$, and the coating's thickness is d. The metal has Fermi level E_F and work function W. The dielectric has electron affinity of χ and dielectric constant of ε_{diel}. The electron initial longitudinal energy is ε. The external dc field of F (in the vacuum) is applied to the emitter surface. The field in the dielectric is $F_{diel} = F/\varepsilon_{diel}$.

The energy diagram for electron emission from a 1D dielectric-coated metal surface is shown in Fig. 4.1. Electrons inside the metal would see a double-triangular potential barrier,

$$V(x) = \begin{cases} 0, & x < 0, \\ V_0 - \chi - eF_{diel}x, & 0 \le x < d, \\ V_0 + e(F - F_{diel})d - eFx, & x \ge d, \end{cases} \tag{4.1}$$

where $V_0 = W + E_F$, with W and E_F being the work function and Fermi level of the metal, respectively; χ is the electron affinity of the dielectric; e is the elementary charge (positive); F is the applied dc electric field in the vacuum; $F_{diel} = F/\varepsilon_{diel}$ is the dc electric field inside the dielectric with ε_{diel} the dielectric constant of the coating layer; and d is the thickness of the dielectric coating layer.

To calculate the probability of electron tunneling through the barrier, we solve the 1D time-independent Schrödinger equation,

$$-\frac{\hbar^2}{2m}\frac{\partial^2}{\partial x^2}\psi(x) + [V(x) - \varepsilon]\psi(x) = 0, \tag{4.2}$$

where $\psi(x)$ is the complex electron wave function, $\hbar$ is the reduced Planck's constant, m is the electron mass, $V(x)$ is the potential given in Eq. (4.1), and ε is the initial longitudinal energy of electrons incident on the metal surface. Here, for simplicity, the electron mass m in all the three regions (i.e., metal, dielectric, and vacuum) is set equal to the electron rest mass.

For $x < 0$, the solution to Eq. (4.2) is

$$\psi_I(x) = e^{ik_0 x} + R_1 e^{-ik_0 x}, \tag{4.3}$$

where $k_0 = \sqrt{2m\varepsilon/\hbar^2}$, R_1 is the reflection coefficient at the metal-dielectric interface. Equation (4.3) represents the superposition of an incident wave and a reflected wave.

For $0 \le x < d$, Eq. (4.2) can be solved by transforming it into the form of $d^2\psi/d\eta_1^2 + \eta_1\psi = 0$ [97], [185]–[187], and the solution is expressed in terms of Airy functions as

$$\psi_{II}(x) = aAi(-\eta_1) + bBi(-\eta_1), \tag{4.4}$$

where $\eta_1 = \left(\frac{2meF_{diel}}{\hbar^2}\right)^{1/3}\left(x + \frac{\varepsilon - V_1}{eF_{diel}}\right)$, with $V_1 = V_0 - \chi$, Ai and Bi are the Airy functions of the first kind and second kind, respectively. ψ_{II} represents the superposition of the transmitted wave from the metal-dielectric interface and the reflected wave from the dielectric-vacuum interface.

For $x \ge d$, the Schrödinger equation, Eq. (4.2), is transformed into $d^2\psi/d\eta_2^2 + \eta_2\psi = 0$, whose solution is

$$\psi_{III}(x) = T_3[Ai(-\eta_2) - iBi(-\eta_2)], \tag{4.5}$$

where $\eta_2 = \left(\frac{2meF}{\hbar^2}\right)^{1/3}\left(x + \frac{\varepsilon - V_2}{eF}\right)$, with $V_2 = V_0 + e(F - F_{diel})d$. Equation (4.5) represents an outgoing wave traveling into the vacuum.

The imposition of the boundary conditions that ψ and $d\psi/dx$ are continuous at both the metal-dielectric interface $x = 0$ and the dielectric-vacuum interface $x = d$ gives

$$1 + R_1 = aA_1 + bB_1, \tag{4.6a}$$

$$1 - R_1 = \zeta(aA_1' + bB_1'), \tag{4.6b}$$

$$aA_2 + bB_2 = T_3(A_3 - iB_3), \tag{4.6c}$$

$$aA_2' + bB_2' = \xi T_3(A_3' - iB_3'), \tag{4.6d}$$

where $A_1 = Ai\left(-\eta_1(x=0)\right)$, $B_1 = Bi\left(-\eta_1(x=0)\right)$, $A_1' = Ai'\left(-\eta_1(x=0)\right)$, $B_1' = Bi'\left(-\eta_1(x=0)\right)$, $A_2 = Ai\left(-\eta_1(x=d)\right)$, $B_2 = Bi\left(-\eta_1(x=d)\right)$, $A_2' = Ai'\left(-\eta_1(x=d)\right)$,

$B_2' = Bi'\left(-\eta_1(x=d)\right)$, $A_3 = Ai\left(-\eta_2(x=d)\right)$, $B_3 = Bi\left(-\eta_2(x=d)\right)$, $A_3' = Ai'\left(-\eta_2(x=d)\right)$, $B_3' = Bi'\left(-\eta_2(x=d)\right)$, Ai' and Bi' are the first derivative of Ai and Bi with respect to their arguments, $\zeta = \frac{i}{k_0}\left(\frac{2meF_{diel}}{\hbar^2}\right)^{1/3}$, and $\xi = (F/F_{diel})^{1/3}$. The transmission coefficient T_3 is

$$T_3 = \frac{2}{\pi[P(U+\zeta Y) - \xi Q(V+\zeta Z)]}, \tag{4.7}$$

where $P = A_3 - iB_3$, $Q = A_3' - iB_3'$, $U = A_1B_2' - B_1A_2'$, $V = A_1B_2 - B_1A_2$, $Y = A_1'B_2' - B_1'A_2'$, and $Z = A_1'B_2 - B_1'A_2$. Note that the heterostructure in Fig. 4.1 can be easily solved numerically using transfer matrix approaches [106], [188]. Here, we expand such a set up analytically.

The transmission probability, defined as $D(\varepsilon) = J_3(\varepsilon)/J_i(\varepsilon)$, is the ratio of the transmitted probability current density in the vacuum to the incident probability current density in the metal, with probability current density $J = i\hbar/2m(\psi\nabla\psi^* - \psi^*\nabla\psi)$, given by

$$D(\varepsilon) = \frac{1}{\pi}\frac{1}{k_0}\left(\frac{2meF}{\hbar^2}\right)^{1/3}|T_3|^2 = \frac{4\alpha\xi}{\pi^3}\frac{1}{\Gamma^2+\Delta^2}, \tag{4.8}$$

where $\Gamma = A_3U + \alpha B_3Y - \xi(A_3'V + \alpha B_3'Z)$, and $\Delta = B_3U - \alpha A_3Y + \xi(\alpha A_3'Z - B_3'V)$, with $\alpha = |\zeta| = \frac{1}{k_0}\left(\frac{2meF_{diel}}{\hbar^2}\right)^{1/3}$.

The electron emission current density can therefore be obtained by

$$J = e\int_0^\infty D(\varepsilon)N(\varepsilon)d\varepsilon, \tag{4.9}$$

where $D(\varepsilon)$ is given in Eq. (4.8) and $N(\varepsilon) = \frac{mk_BT}{2\pi^2\hbar^3}\ln\left[1+\exp\left(\frac{E_F-\varepsilon}{k_BT}\right)\right]$ is the supply function as used in Eq. (2.9) of chapter 2, with k_B the Boltzmann's constant and T the temperature.

4.3 Results and Discussion

Figure 4.2 shows the tunneling probability for electrons with initial longitudinal energy of $\varepsilon = E_F$, as a function of dielectric thickness d and dielectric constant ε_{diel}, under various combinations of dc electric field F and dielectric electron affinity χ, calculated from Eq. (4.8). The metal is assumed to be gold, with work function $W = 5.1\ eV$ and Fermi energy $E_F = 5.53\ eV$. Unless stated otherwise, these values are the default cathode metal properties in this chapter. When $F = 1$ V/nm, as shown in Figs. 4.2(a) – 4.2(c), the electron tunneling probability $D(E_F)$ decreases with the dielectric constant ε_{diel} for a given d. For $\varepsilon_{diel} > 2$, $D(E_F)$ decreases as d increases; however, for $\varepsilon_{diel} < 2$, $D(E_F)$ increases as d increases. As the dc electric field

increases to $F = 5$ V/nm or $F = 10$ V/nm, as shown in Figs. 4.2(d) – 4.2(i), it is obvious that the tunneling probability $D(E_F)$ increases, due to the narrowing of the surface potential barrier by the dc electric field. More importantly, there appear strong resonant peaks in $D(E_F)$. For a given F and χ, the resonant peaks shift to a larger value of ε_{diel} as d increases. The resonant peaks extend to a larger area in the $d - \varepsilon_{diel}$ domain as either F or χ increases.

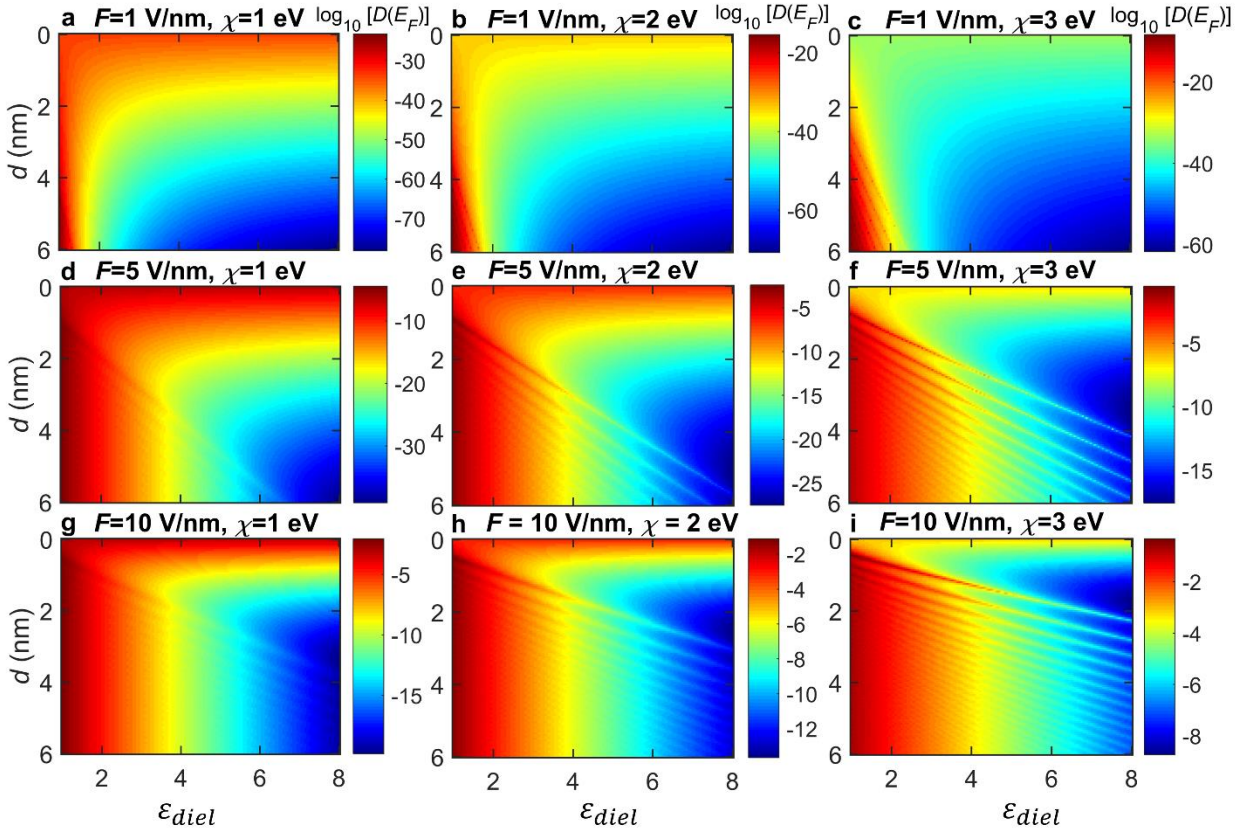

Figure 4.2 Electron tunneling probability $D(\varepsilon = E_F)$ as a function of the dielectric thickness d and dielectric constant ε_{diel}, under various combinations of dc electric field F and the dielectric electron affinity χ: (a) - (c) $F = 1$ V/nm, (d) - (f) $F = 5$ V/nm, (g) - (i) $F = 10$ V/nm; with $\chi = 1$ eV in (a), (d), (g); $\chi = 2$ eV in (b), (e), (h); and $\chi = 3$ eV in (c), (f), (i). The electron initial longitudinal energy is assumed to be Fermi energy $\varepsilon = E_F$. The metal is assumed to be gold, with work function $W = 5.1\ eV$ and Fermi energy $E_F = 5.53\ eV$.

The effects of dielectric thickness d, dielectric constant ε_{diel}, and dielectric electron affinity χ on the electron tunneling probability $D(E_F)$ are further shown in line plots in Fig. 4.3. The solid curves, which give $D(E_F)$ as a function of d in Figs. 4.3(a) – 4.3(c), show a parabola-like shape when $0 < d < d_0$, with a rough estimation of $d_0(\text{nm}) \sim \varepsilon_{diel} W/eF$. When $d > d_0$, $D(E_F)$ oscillates around a constant and the oscillation amplitude decays with d. For a given set of ε_{diel} and χ as in Fig. 4.3(a), when F increases, the tunneling probability increases, due to the

narrowing of the potential barrier by the dc electric field. The resonance peaks shift towards smaller dielectric thickness values as F increases, indicated by the dash line in Fig. 4.3(a). For fixed F and χ as in Fig. 4.3(b), the tunneling probability decreases with increasing ε_{diel}, due to the smaller dc electric field $F_{diel} = F/\varepsilon_{diel}$ inside the dielectric. The dash line in Fig. 4.3(b) indicates that the resonance peaks shift to a large dielectric thickness value as ε_{diel} increases, which is also consistent with the rough estimation of $d_0(\text{nm}) \sim \varepsilon_{diel} W/eF$. For a given combination of F and ε_{diel} as in Fig. 4.3(c), the tunneling probability increases with electron affinity χ, due to the lowering of the potential barrier at metal-dielectric interface. It is shown that increasing χ makes the oscillation stronger; meanwhile, the resonance peaks slightly shift to a small dielectric thickness.

It is interesting to find that the tunneling probability from coated cathodes can be larger than that from the uncoated ones. Some specific cases are highlighted by the yellow blocks in Figs. 4.3(b) and 4.3(c). For these cases, the dielectric-coated cathode has larger electron tunneling probability than the uncoated one, regardless of the thickness of the coating. Figures 4.3(b) and 4.3(c) show that the dielectric coating with small ε_{diel} and large χ tends to enhance field emission from 1D flat cathode surfaces.

Figures 4.3(d) – 4.3(f) show $D(E_F)$ as a function of ε_{diel} for various F, d, and χ. It is obvious that the tunneling probability decreases with dielectric constant, for a given combination of F, d and χ, due to the smaller dc electric field inside the dielectric. For fixed F and χ in Fig. 4.3(e), as d increases, there appear more resonance peaks for $D(E_F)$ as a function of ε_{diel}. The curves for dielectric thickness $d > 2$ nm start to overlap. That is because $D(E_F)$ gradually becomes constant against d for a given combination of ε_{diel}, χ, and F, which has been shown in Figs. 4.3(a) – 4.3(c). Increasing χ results in more and stronger resonance peaks on curves for $D(E_F)$ vs ε_{diel}, and extends those resonance peaks to large ε_{diel} values, as shown in Fig. 4.3(f).

$D(E_F)$ as a function of χ is shown in Figs. 4.3(g) – 4.3(i) for various F, ε_{diel}, and d. The tunneling probability increases with χ, for a given set of F, ε_{diel}, and d, due to the lowering of the potential barrier at the metal-dielectric interface. When ε_{diel} increases, $D(E_F)$ decreases, as shown in Fig. 4.3(h), due to the smaller dc electric field inside the dielectric and therefore wider potential barrier for an electron to tunnel through. When $F = 6$ V/nm and $\varepsilon_{diel} = 4$ in Fig. 4.3(i), the slope of the curves increases with d. It can be observed that the tunneling probability for cases of $d = 2$ nm and 4 nm are larger than that for cases of $d = 0.5$ nm and 1 nm for larger χ,

which has also been shown in Figs. 4.3(a) – 4.3(c). Additionally, more resonance peaks are observed on curves for $D(E_F)$ as a function of χ, when d increases.

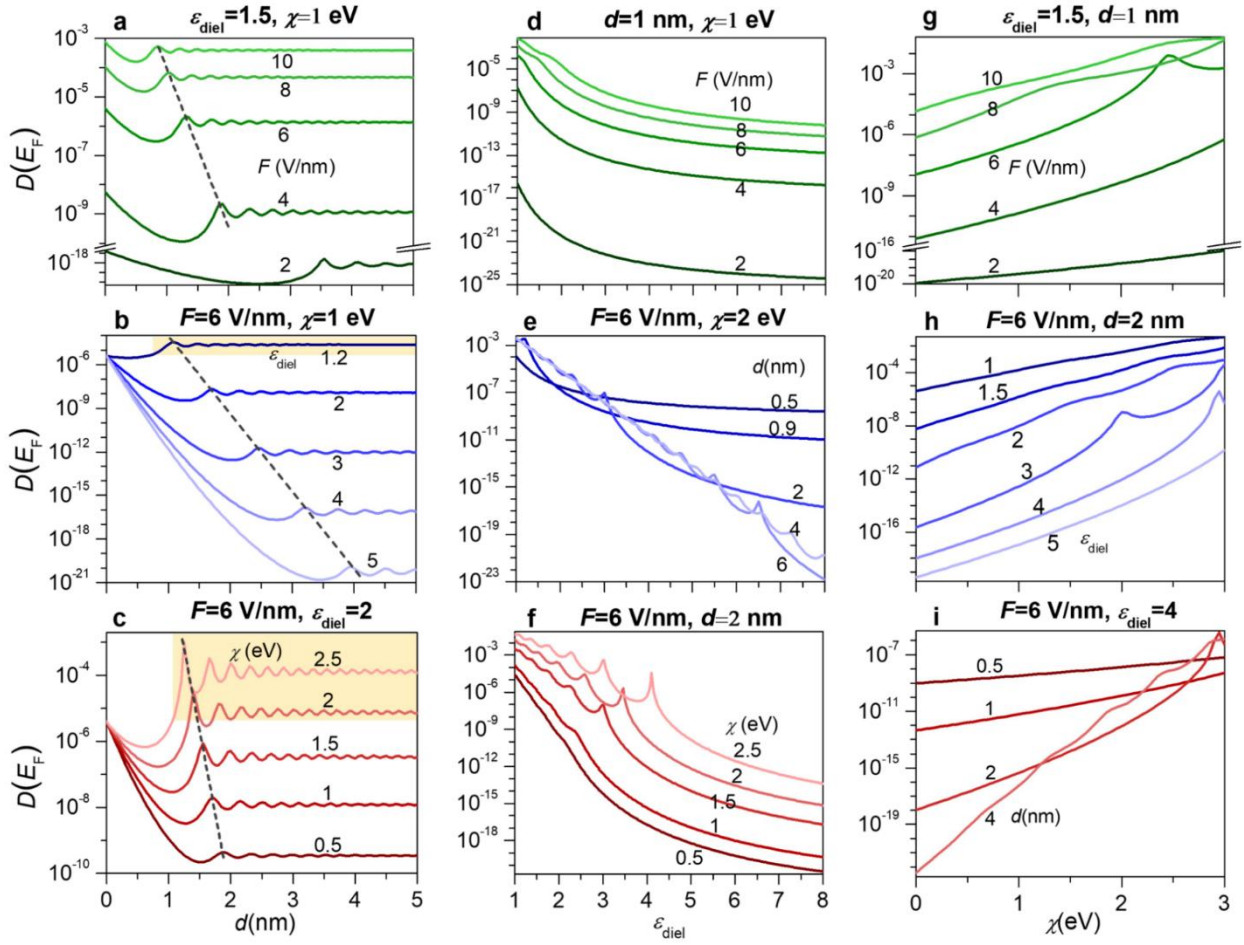

Figure 4.3 Effects of dielectric thickness d, dielectric constant ε_{diel}, dielectric electron affinity χ, and dc electric field F on the electron tunneling probability $D(\varepsilon = E_F)$ from dielectric-coated metal surface. $D(\varepsilon = E_F)$, calculated from Eq. (4.8), as a function of (a) – (c) dielectric thickness d; (d) – (f) dielectric constant ε_{diel}; and (g) – (i) dielectric electron affinity χ. The electron initial energy is assumed to be Fermi level E_F. The metal is assumed to be gold, with work function $W = 5.1\ eV$ and Fermi energy $E_F = 5.53\ eV$.

Figure 4.4(a) shows the electron tunneling probability $D(\varepsilon)$ as a function of electron initial longitudinal energy ε, for various combinations of dielectric coating thickness d, dielectric constant ε_{diel} and electron affinity χ, with the applied dc electric field $F = 7$ V/nm. The tunneling probability increases as ε becomes larger, due to the lower potential barrier seen by electrons with larger ε. Resonances appear at certain electron initial longitudinal energies, e.g., at $\varepsilon \approx E_F$, 7 eV and 9 eV for the case of $d = 1$ nm, $\varepsilon_{diel} = 1.5$, and $\chi = 2\ eV$ (orange curve in Fig. 4.4(a)). It is interesting to note that similar resonance behavior is also observed in previous

studies in electron tunneling through the metal-oxide-semiconductor structures [189], double-barrier semiconductors [190], metal surfaces with closely positioned positive ions [191], and nanostructured semiconductor film cathodes [192]. Figure 4.4(b) shows the electron emission current density per energy $J(\varepsilon) = eN(\varepsilon)D(\varepsilon)$ as a function of ε for three temperatures at $T =$ 100, 300, and 2000 K. It is obvious that when $T = 2000\ K$, more electrons with initial energies above the Fermi level are emitted, since more electrons are populated above the Fermi level at higher temperature. The contribution due to thermionic emission (i.e., emission of electrons with ε above the vacuum level) can be observed for $T = 2000\ K$, as indicated in the red shaded area. The total emission current density (calculated from Eq. (4.9)) is $J =$ 3389, 3497, and 21150 A/cm^2 at $T =$ 100, 300, and 2000 K, respectively.

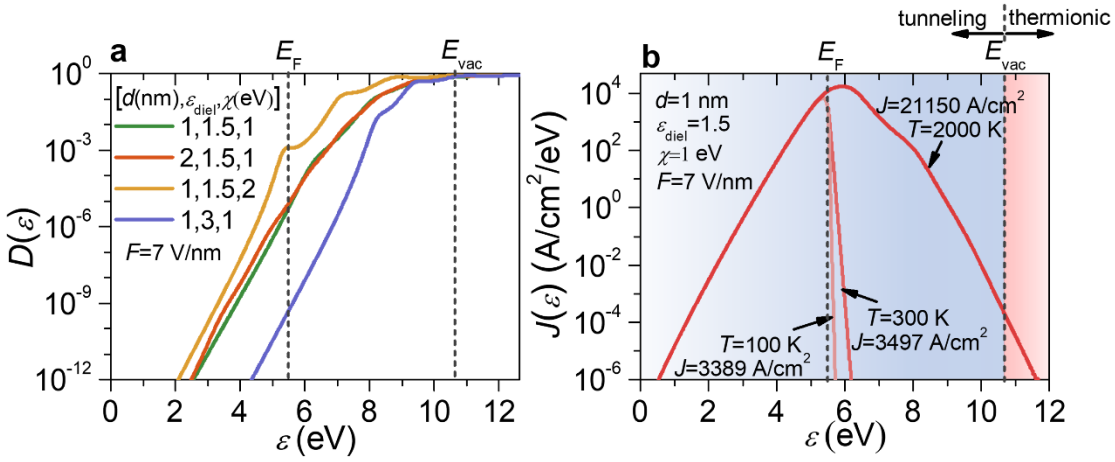

Figure 4.4 (a) Electron tunneling probability $D(\varepsilon)$ as a function of electron initial longitudinal energy ε, for various combinations of dielectric thickness d, dielectric constant ε_{diel} and electron affinity χ, at the applied dc field of 7 V/nm; (b) the emission current density per energy $J(\varepsilon) = eN(\varepsilon)D(\varepsilon)$ under various temperatures T=100, 300, 2000 K, for fixed $d = 1$ nm, $\varepsilon_{diel} = 1.5$, $\chi = 1$ eV, and $F = 7$ V/nm.

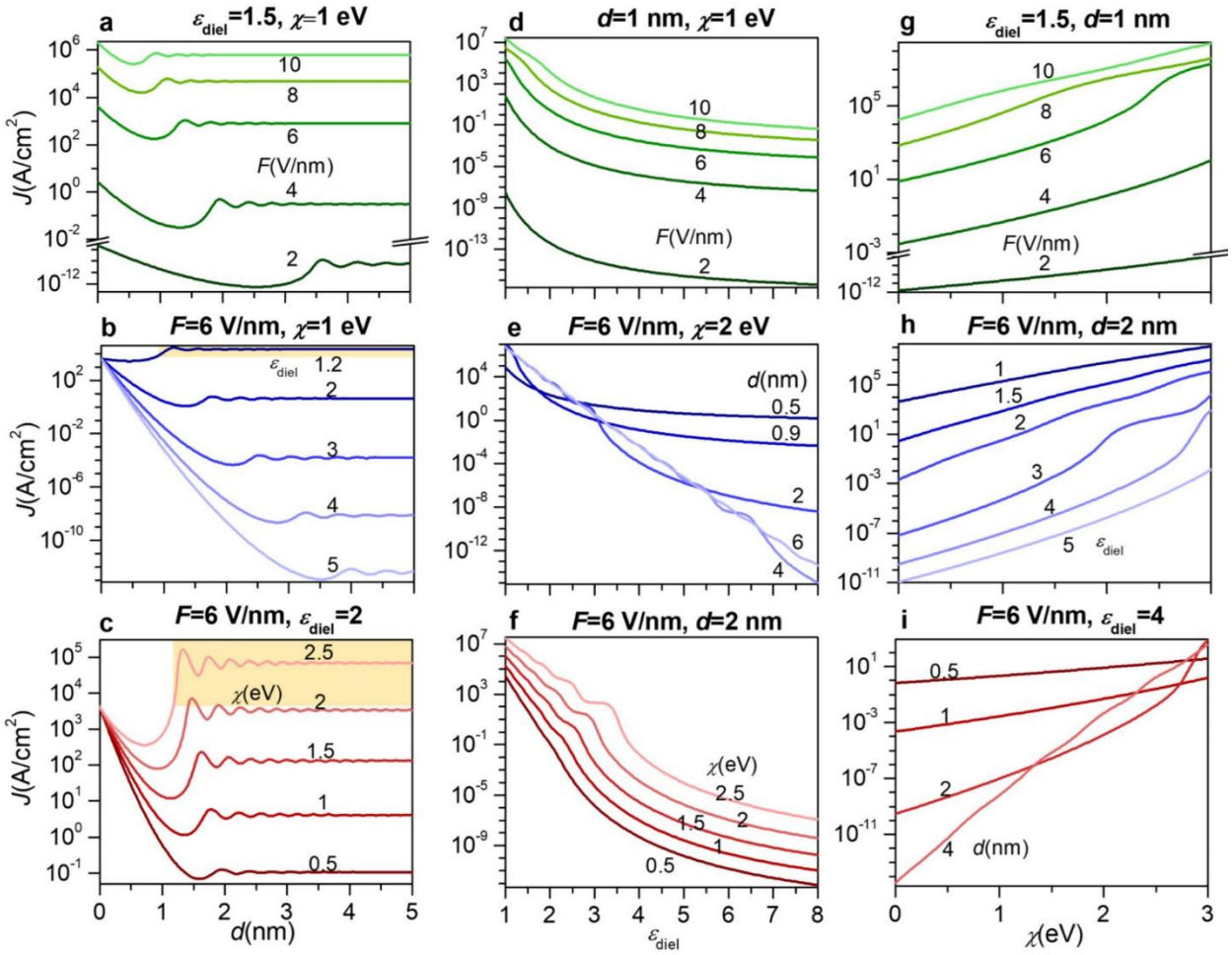

Figure 4.5 Effects of dielectric thickness d, dielectric constant ε_{diel}, dielectric electron affinity χ, and dc electric field F on the electron emission current density from dielectric-coated metal surfaces. The electron emission current density, calculated from Eq. (4.9), as a function of (a) – (c) dielectric thickness d; (d) – (f) dielectric constant ε_{diel}; and (g) – (i) dielectric electron affinity χ. The metal is assumed to be gold, with work function $W = 5.1\ eV$ and Fermi energy $E_F = 5.53\ eV$.

Figure 4.5 shows effects of dielectric thickness d, dielectric constant ε_{diel}, electron affinity χ, and dc electric field F, on the emission current density J calculated from Eq. (4.9). Since most of the emitted electrons are with initial energies near Fermi level at room temperature, indicated in Fig. 4.4(b), the emission current density follows similar trends as the tunneling probability $D(E_F)$ in Fig. 4.3. The emission current density as a function of dielectric thickness, shows a parabola-like shape in the range of $0 < d \lesssim d_0[\text{nm}] = \varepsilon_{diel} W/eF$. When $d \gtrsim d_0$, J oscillates around a constant. The behavior where the emission current density settles to a constant value for thick dielectric coatings under a fixed electric field is because the potential in the vacuum region drops below the electron initial energy, which does not contribute to the potential barrier for

electron tunneling. As a result, the emission current is determined by the barrier inside the dielectric region only and does not depend on the dielectric thickness, when the thickness is large. The oscillation can be ascribed to the interference between incident electron waves and reflected waves inside the dielectric layer [189]. It is found that resonance peaks on the curves for emission current density J in Fig. 4.5 is not as sharp as those on electron tunneling probability $D(E_F)$ in Fig. 4.3. This can be explained by the emission of electrons with different initial energies, which, in combination, smooths the curve. The possible physical cause is the broadening of the resonances associated with the interference between reflected and transmitted waves for different initial energy of the electrons [188]. As F increases, the emission current density increases, and resonance peaks shift towards smaller dielectric thickness d, as shown in Fig. 4.5(a). When the dielectric constant ε_{diel} increases, the emission current density becomes smaller, due to the smaller dc electric field in the dielectric so that the barrier inside the dielectric is less narrowed. Meanwhile, an increased ε_{diel} shifts the resonance peaks to a large thickness d, as shown in Fig. 4.5(b). When the electron affinity χ of the dielectric increases, the emission current density increases because of the lowering of the potential barrier at the metal-dielectric interface, and resonance peaks shift slightly to small thickness values. Similar to the tunneling probability in Fig. 4.3, a relatively small ε_{diel} or a larger χ may induce a larger emission current density than the bare metal, as highlighted by the yellow blocks in Figs. 4.5(b) and 4.5(c). For the case of $F = 6$ V/nm, $\varepsilon_{diel} = 2$, and $\chi = 2\ eV$ in Fig. 4.5(c), J is larger than that of the uncoated case only near a few resonant peaks, whereas $D(E_F)$ for this case in Fig. 4.3(c) is almost continuously larger than the uncoated case for $d > 1.5$ nm. It can be explained by the fact that more electrons are emitted with initial longitudinal energies below Fermi level at room temperature, as shown in Fig. 4.4(b). For electrons with $\varepsilon < E_F$, the tunneling probability from coated metals with dielectric thickness d highlighted in Fig. 4.3(c) can be smaller than that from bare metal, thus yielding a smaller emission current density.

The electron emission current density J as a function of dielectric constant ε_{diel} is shown in Figs. 4.5(d) – 4.5(f). When ε_{diel} increases, J decreases. As shown in Fig. 4.5(e), for the case of $F = 6$ V/nm and $\chi = 2\ eV$, the curves for $d > 2$ nm start to get overlapped, since the emission current density becomes almost constant as d becomes large, as shown in Figs. 4.5(a) – 4.5(c). When χ increases in Fig. 4.5(f), more resonance peaks appear and extend towards larger value of ε_{diel}.

Figures 4.5(g) – 4.5(i) show the electron emission current density as a function of dielectric electron affinity χ. When χ increases, the emission current density increases. There is a sharp increase of the slope at $\chi \approx 2.5\ eV$ for $F = 6$ V/nm in Fig. 4.5(g). The sharp increases of the slope are also shown in Fig. 4.5(h) at $\chi \approx 1.8\ eV$ and $\chi \approx 2.8\ eV$ for the case of $\varepsilon_{diel} = 3$, and at $\chi = 2.6\ eV$ for the case of $\varepsilon_{diel} = 4$. These features are consistent with the resonant peaks of $D(E_F)$ observed in Figs. 4.3(g) and 4.3(h). When the dielectric thickness increases, the slope of the curves in Fig. 4.5(i) increases. At $\chi = 3\ eV$, the emission current density with $d = 2$ nm and 4 nm exceeds that with $d = 0.5$ nm and 1 nm in Fig. 4.5(i). This shows that at large χ where surfaces with thicker dielectric become better emitters, which is because a higher χ would lower the surface barrier, and a thicker dielectric layer would provide an overall smaller tunneling barrier (see, e.g., the barriers in Fig. 4.7).

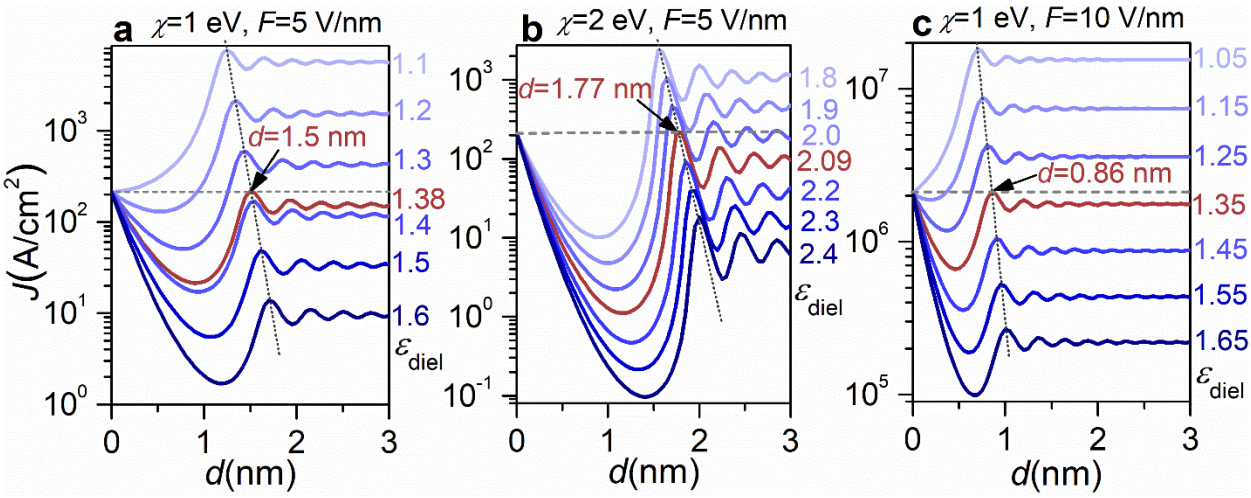

Figure 4.6 Emission current density as a function of dielectric thickness d under various dielectric constants ε_{diel} for (a) $\chi = 1\ eV$ and $F = 5$ V/nm; (b) $\chi = 2\ eV$ and $F = 5$ V/nm; and (c) $\chi = 1\ eV$ and $F = 10$ V/nm. The metal is assumed to be gold, with work function $W = 5.1\ eV$ and Fermi energy $E_F = 5.53\ eV$.

As already seen in Figs. 4.3 and 4.5, coating with a relatively small ε_{diel} or a larger χ may induce a larger emission current density than the uncoated cathode. Figure 4.6 provides more calculations to determine the threshold values of dielectric thickness d_{th} and dielectric constant ε_{diel}^{th}, at which the emission current density J is equal to that from the bare metal, for a given dielectric electron affinity χ and dc electric field F. When $\chi = 1$ eV and $F = 5$ V/nm, the thresholds are found to be $d_{th} = 1.5$ nm and $\varepsilon_{diel}^{th} = 1.38$, as shown in Fig. 4.6(a). A dielectric constant smaller than ε_{diel}^{th} would enhance the electron emission compared to the uncoated case,

with thicknesses corresponding to the curves above the horizontal dash line. When the dielectric electron affinity increases to $\chi = 2\ eV$, the dielectric thickness and dielectric constant thresholds becomes larger, i.e., $d_{th} = 1.77$ nm and $\varepsilon_{diel}^{th} = 2.09$ in Fig. 4.6(b). When the dc field increases to 10 V/nm, the dielectric thickness and dielectric constant threshold shift towards smaller values, i.e., $d_{th} = 0.86$ nm and $\varepsilon_{diel}^{th} = 1.35$ in Fig. 4.6(c). Although it is difficult to give an exact expression to determine the dielectric constant and thickness thresholds, it is found that all three cases in Fig. 4.6 roughly follow the empirical relation at room temperature,

$$d_{th}[\text{nm}] = \frac{\varepsilon_{diel}^{th} W}{eF}, \tag{4.10}$$

whose physical origin will become clear from the analysis of the potential barrier profiles in Fig. 4.7.

Figures 4.7(a) – 4.7(c) show the potential profile induced by the dc electric field $F = 5$ V/nm, for the coated metal with various dielectric thicknesses. The dielectric constants for Figs. 4.7(a) – 4.7(c) are $\varepsilon_{diel} = 1.2$, 1.38, and 1.5, respectively, where $\varepsilon_{diel} = 1.38$ is the dielectric constant threshold for the case of $\chi = 1\ eV$ and $F = 5$ V/nm in Fig. 4.6(a). In the dielectric layer, the slope of the potential profile is F/ε_{diel}. To evaluate how the potential barrier affects the tunneling probability, the potential barrier width $w(\varepsilon)$, indicated by the double-arrow line at initial energy ε in Fig. 4.7(a), and the corresponding tunneling probability $D(\varepsilon)$ at $\varepsilon = E_F$ are plotted as a function of dielectric thickness d in Figs. 4.7(d) – 4.7(f). The potential barrier width $w(E_F)$ increases with the dielectric thickness d when $d < \varepsilon_{diel}(W - \chi)/eF$ (for arbitrary ε, this is $\varepsilon_{diel}(W + E_F - \varepsilon - \chi)/eF$), due to the smaller electric field in the dielectric than that in the vacuum. $w(E_F)$ decreases in the dielectric thickness range of $\varepsilon_{diel}(W - \chi)/eF < d < \varepsilon_{diel}W/eF$, where electrons need to tunnel through two separate barriers—one in the dielectric and the other in the vacuum. When $d > \varepsilon_{diel}W/eF$ (this is $\varepsilon_{diel}(W + E_F - \varepsilon)/eF$ for arbitrary ε), electrons with initial longitudinal energy of E_F can be emitted by tunneling through only the barrier in the dielectric, and therefore the barrier width $w(E_F)$ reaches a constant for the same applied dc electric field.

The corresponding electron tunneling probability, shown as blue curves in Figs. 4.7(d) – 4.7(f), decreases as $w(E_F)$ increases, and increases when $w(E_F)$ decreases. $D(E_F)$ reaches its first resonance peak at $d \approx \varepsilon_{diel}W/eF$, where electrons only need to tunnel through one potential barrier to emit. The red dash lines in Figs. 4.7(d) – 4.7(f) indicate that the maximum

resonance peak of $D(E_F)$ is roughly at the same thickness $d = \varepsilon_{diel}W/eF$ (cf. Eq. (4.10)), where $w(E_F)$ starts to become a constant. More calculations (not shown) for various combinations of F and χ show that the maximum resonance peak of $D(E_F)$ can deviate but remain close to $d = \varepsilon_{diel}W/eF$. The oscillation in $D(E_F)$ after the maximum is due to the interference between the incident waves and reflected wave at the dielectric-vacuum interface. It is also observed that when $\varepsilon_{diel} = 1.38$, $D(E_F)$ by the coated metal with the dielectric thickness $d = \varepsilon_{diel}W/eF = 1.41$ nm is larger than that by the bare metal, although potential barrier width of the coated case is larger than that of the bare one. By observing the potential profiles in Figs. 4.7(a) – 4.7(c), it is expected that the average constant value around which $D(E_F)$ oscillates at large d may be estimated by,

$$D(\varepsilon) = \frac{4\alpha}{\pi}\frac{1}{(A_1 + \alpha B_1')^2 + (\alpha A_1' - B_1)^2}, \tag{4.11}$$

with all the terms as defined in Sec. 4.2 [in Eqs. (4.6) and (4.8)], which is the electron tunneling probability due to a single triangular barrier (i.e., Fowler-Nordheim field emission [187], [193]) with potential barrier height $W - \chi$ and electric field F_{diel}. Equation (4.11) is plotted as blue dotted lines in Figs. 4.7(d) – 4.7(f).

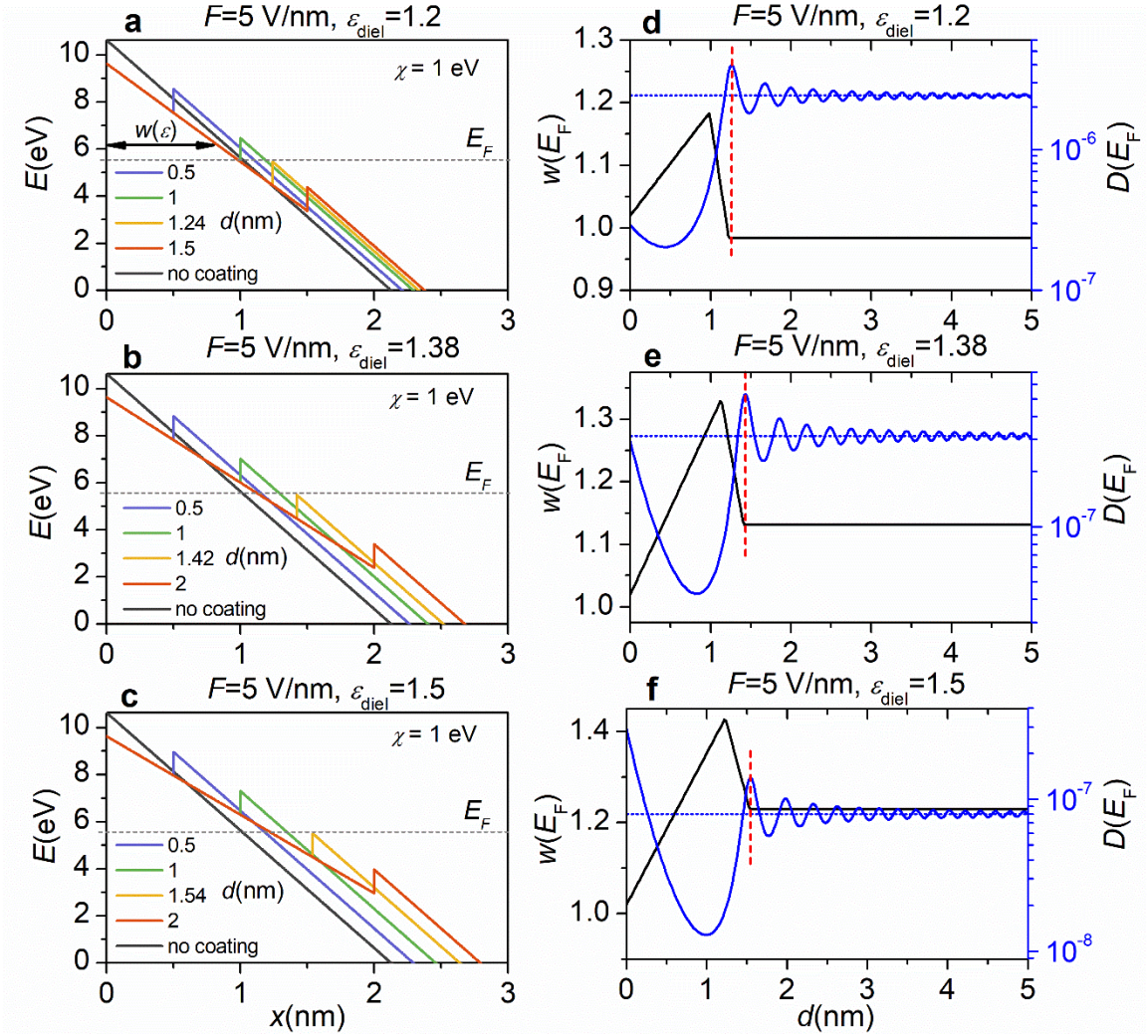

Figure 4.7 (a) – (c) Potential profile for coated metal with dielectric constants of (a) $\varepsilon_{diel} = 1.2$; (b) $\varepsilon_{diel} = 1.38$; (c) $\varepsilon_{diel} = 1.5$ for various dielectric thicknesses d (nm). (d) – (f) Barrier width w seen by the electron with initial longitudinal energy of $\varepsilon = E_F$, and the corresponding electron tunneling probability D as a function of dielectric thickness d for coatings with dielectric constants of (d) $\varepsilon_{diel} = 1.2$; (e) $\varepsilon_{diel} = 1.38$; (f) $\varepsilon_{diel} = 1.5$. The applied dc electric field $F = 5$ V/nm. Blue dotted lines are from Eq. (4.11).

Thus, by comparing Eq. (4.11) and the tunneling probability from the uncoated cathode, one may determine the threshold value of dielectric constant ε_{diel}, which is then used in Eq. (4.10) to give the threshold value of dielectric constant d_{th}, in order to have field emission current larger than the uncoated case from 1D flat surfaces.

4.4 Comparison with Modified Double-barrier Fowler-Nordheim Equation

In this section, we compare our quantum model with the modified Fowler-Nordheim (FN) equation with a double-barrier potential profile, developed for cathode surfaces with an oxidation

layer [183], [184],

$$J = \frac{e^3 F^2}{16\pi^2 \hbar W B^2} \exp\left[-\frac{4\sqrt{2m}}{3e\hbar F} W^{\frac{3}{2}} C\right] \tag{4.12}$$

with

$$B = \varepsilon_{diel}\left[\sqrt{\frac{W_{eff}}{W}} - H\left(W_{eff} - eF_{diel}d\right)\sqrt{\frac{W_{eff} - eF_{diel}d}{W}}\right] + H(W - eF_{diel}d)\sqrt{\frac{W - eF_{diel}d}{W}}$$

and

$$C = \varepsilon_{diel}\left[\left(\frac{W_{eff}}{W}\right)^{\frac{3}{2}} - H\left(W_{eff} - eF_{diel}d\right)\left(\frac{W_{eff} - eF_{diel}d}{W}\right)^{\frac{3}{2}}\right]$$

$$+ H(W - eF_{diel}d)\left(\frac{W - eF_{die}d}{W}\right)^{\frac{3}{2}}$$

where e and m are the positive elementary charge and electron mass (set equal to electron rest mass in all the three regions of metal, dielectric, and vacuum), $\hbar$ is the reduced Planck's constant, F is the applied dc electric field in the vacuum, $F_{diel} = F/\varepsilon_{diel}$ is the electric field inside the dielectric layer, W is the nominal work function of the metal, $W_{eff} = W - \chi$ is the effective work function at metal-dielectric interface, and d is the thickness of the dielectric layer, $H(x)$ is the Heaviside function. In case of no dielectric layer, $W_{eff} = W$, $d = 0$, $\varepsilon_{diel} = 1$, B and C become 1, and Eq. (4.12) recovers the Fowler-Nordheim equation [97].

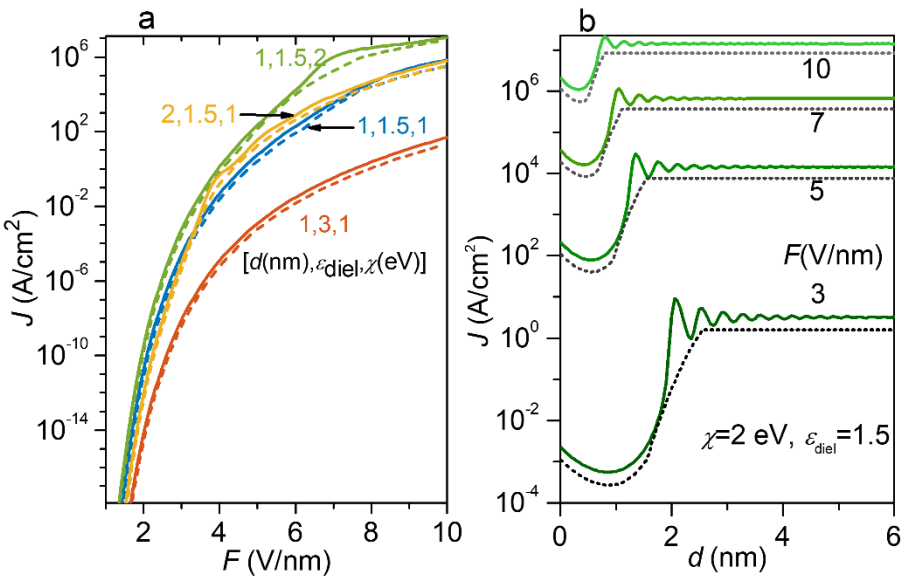

Figure 4.8 (a) The emission current density J from the dielectric-coated metal, calculated from Eq. (4.9), and the modified Fowler-Nordheim equation, Eq. (4.12), as a function of electric field under various combinations of dielectric thickness d, dielectric constant ε_{diel}, and dielectric electron affinity χ. (b) J from the dielectric-coated metal, calculated from the quantum model (solid lines) and the modified Fowler-Nordheim equation (broken lines), as a function of dielectric thickness d. The dielectric has $\varepsilon_{diel} = 1.5$, and $\chi = 2\ eV$.

The electron emission current density of the quantum model, calculated from Eq. (4.9) is compared with that calculated from the modified FN equation, Eq. (4.12), as shown in Fig. 4.8. The two models show good agreement in the scaling, with the quantum model giving a higher emission current density in general. This is because the quantum model considers electron emission from all the energy levels at room temperature T = 300 K, whereas the FN based model assumes electron emission at 0 K. The quantum model shows resonance behavior in J vs d, which cannot be revealed by the modified FN equation.

4.5 Concluding Remarks

In this chapter, we have developed an exact theory for field emission from dielectric-coated cathode surfaces, by solving the one-dimensional time-independent Schrödinger equation with a double-triangular barrier, which is formed by applying dc electric field to the dielectric-coated cathode surface. The model includes both field emission and thermionic emission. It is found that the combination of a small dielectric constant and a large dielectric electron affinity tends to induce a larger emission current density than bare metal for 1D flat cathode surfaces, under a given dc electric field. It is found the emission current density is larger than the uncoated case when the dielectric constant is smaller than a certain value ε_{diel}^{th} and the dielectric thickness is

larger than the threshold value $d_{th}[\mathrm{nm}] \approx \varepsilon_{diel} W/eF$ with $\varepsilon_{diel} < \varepsilon_{diel}^{th}$. This relation is consistent with the sharp transition of the potential barrier width in the double-triangular barrier. This quantum model is also compared with a modified Fowler-Nordheim equation for a double-triangular barrier, showing good agreement in the scaling of the emission current. The theory provides insights for designing the emitter with higher efficiency and better stability.

CHAPTER 5 PHOTOEMISSION FROM METAL SURFACES WITH NANOSCALE DIELECTRIC COATINGS AND ITS ENHANCEMENT BY PLASMONIC RESONANCE

This chapter is based on the published journal papers "Theory of laser-induced photoemission from a metal surface with nanoscale dielectric coating," *J. Appl. Phys.*, vol. 131, no. 6, p. 064903, Feb. 2022, doi: 10.1063/5.0078060, by **Yang Zhou** and Peng Zhang, and "Plasmon-enhanced resonant photoemission using atomically thick dielectric coatings," *ACS Nano*, vol. 14, no. 7, p. 8806-8815, Jun. 2020, doi: 10.1021/acsnano.0c03406, by X. Xiong, **Yang Zhou**, Y. Luo, X. Li, M. Bosman, L. K. Ang, Peng Zhang, and L. Wu.

5.1 Introduction

High-performance photocathodes or photoemitters are always required to be of high efficiency and high stability [69], [106], [194]. Coatings, such as, graphene, nano-diamond, silicon dioxides, and zinc dioxides, are proposed to fabricated atop cathodes to protect them from degradation by ions and electrons bombardment, or oxidization under poor vacuum conditions [70]–[74]. Coatings not only elongate the operational lifetime and the current stability of photocathodes, but also enhance the quantum efficiency of photoemission by the lowering of the effective work function or the enhancement of laser field [47], [70], [71], [78], [79]. Analogous heterostructure photocathodes are prospective to optimize the quantum yield and emittance simultaneously for electron sources in X-ray free-electron lasers [69], [188].

The development of theory for photoemission from coated cathodes facilitates the optimization of the design and performance of photocathodes. Commonly used Fowler-Nordheim-type equations, which assume photoelectron emission occurs in positive half cycles of the intense laser, are applicable only in the optical field tunneling regime but not in the multiphoton absorption regime [184]. Furthermore, it has been shown that negative half cycles also play a role in the photoemission process [25]. Therefore, an exact model for photoemission from cathodes with ultrathin coatings is desirable to uncover the interplay of various parameters on photoemission and provide insights into the development of photocathodes.

The introduction of surface coating results in an irregular double-barrier under the optical field. In Sec. 5.2, we approximate the double-barrier to an effective single triangular barrier by WKBJ approximation and employ the quantum photoemission model in Sec. 2.2, which is

developed by solving the TDSE subject to a triangular oscillating potential barrier, to investigate the photoemission processes under the plasmon resonant conditions on both bare and coated Au-nanopyramid field emitters. It is found that a 1 nm thick layer of SiO_2 around a Au-nanopyramid will enhance photoemission current density by ~2 orders of magnitude and the optical field tunneling can be accessed at a significantly reduced incident laser intensity.

In Sec. 5.3, we construct an exact analytical quantum model for laser-driven photoemission from cathodes coated with a nanoscale-thick dielectric by solving the TDSE. The model is applicable to photoemission for arbitrary combinations of metal properties (i.e., work function and Fermi level), dielectric properties (i.e., thickness, relative permittivity, and electron affinity), laser field (i.e., wavelength, and field strength or intensity), and dc field. Based on the analytical solution, we investigate the effects of dielectric properties on photoemission. This analytical model is compared with the effective single-triangular-barrier quantum model [47] and modified Fowler-Nordheim equation [183], [184] for photoemission from a dielectric-coated flat metal surface and a dielectric-coated pyramid-shaped nanoemitter.

5.2 Effective Single-triangular-barrier Quantum Model

5.2.1 Pyramid-shaped Nanoemitter

Xiao Xiong and Lin Wu *et al*. [47] designed an efficient plasmonic photoemitter supporting antenna mode [195] by full-wave optical simulations [196]–[198], so that the incident optical energy could be maximally concentrated to the tip of the emitter. Figure 5.1(a) illustrates the schematics of the bare and coated Au-nanopyramid field emitters sitting on a Au substrate. The nanopyramid emitter has a side length of a at the bottom surface or κa at the top surface and height h, either bare in a vacuum or coated with a thin dielectric layer of thickness d and refractive index n. The geometrical settings of the nanopyramid emitters (a, κ, and h) are used to design the resonant wavelength of the antenna mode [47].

For a typical photoemitter with $a = h = 40$ nm and $\kappa = 0.1$, under the illumination of z-polarized light from the side, the antenna mode at 590 nm for the bare photoemitter or at 608 nm for the coated photoemitter ($d = 1$ nm, $n = 1.5$) is observed, as shown in Fig. 1(a) in ref. [47]. Though occurring at similar resonant wavelengths, the plasmon field enhancement and the underlying microscopic physics differ drastically. For the bare Au-nanopyramid, a typical plasmonic nanostructure, the enhanced plasmonic field concentrates at the sharp corners of the Au with maximum field enhancement $\beta_{Au} = 35$, and its magnitude exponentially decays into the

vacuum, dying out at a distance of <10 nm. In contrast, for the coated case, the dielectric coating with a refractive index n creates an interface with the vacuum. This interface helps to reflect and confine the plasmonic fields into an even smaller volume [195], effectively forming a dielectric waveguide that can locally enhance the fields at the Au surface [199]. As a consequence, the maximum field enhancement at the Au surface β_{Au} increases from 35 to 200 (corresponding to an optical intensity enhancement from 1225 to 40000) due to the combined effects of geometrical plasmon field enhancement and a secondary field enhancement from the plasmonic field confinement. The tremendously increased field enhancement β_{Au} at the Au surface from the antenna mode is particularly desirable, which can vastly facilitate the photoemission process to operate at the optical field tunneling regime at a much lower incident field strength.

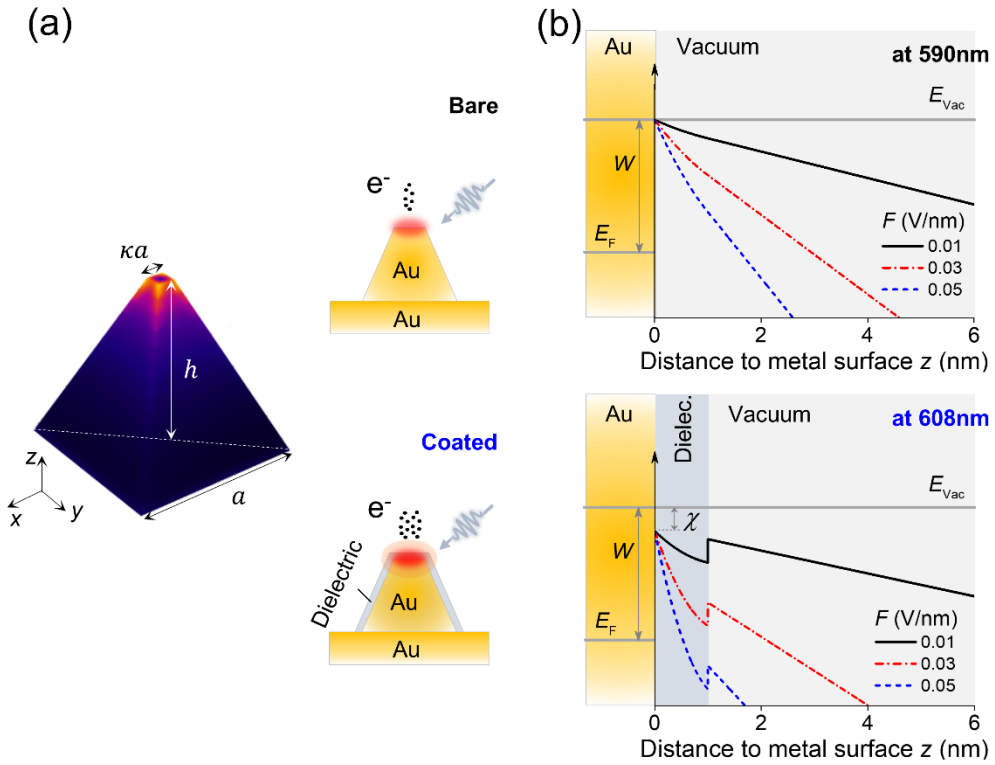

Figure 5.1 (a) Left: Geometrical settings of Au-nanopyramid field emitter; and Right: Schematics of the bare and coated Au-nanopyramid field emitter sitting on a Au substrate, illuminated by *z*-polarized light from the side. (b) Potential profile of the tunneling barriers induced by different incident laser field strengths F for bare (top) and coated (bottom) Au-nanopyramid field emitter.

5.2.2 Effective Field Enhancement

To understand the photoemission process, we start with the time-dependent potential barrier $\phi(z,t)$ that is faced by the free electrons in Au to tunnel through and emit. In the dielectric

region, $0 < z < d$, it is written as:

$$\phi(z,t) = V_0 - eF\cos\omega t \int_0^z \beta(s)ds \cong V_0 - eF\cos\omega t\left(\frac{\beta_D - \beta_{Au}}{2d}z^2 + \beta_{Au}z\right) \quad (5.1)$$

Here, z denotes the distance to the top surface of the Au tip; $V_0 = W + E_F - \chi$ is the nominal potential barrier height at the Au surface, where $W = 5.1$ eV and $E_F = 5.53$ eV are the work function and Fermi energy of Au and χ is the electron affinity of the dielectric layer; e is the elementary charge (positive); $\omega = 2\pi c/\lambda$ denotes the angular frequency with the laser wavelength λ, where c is the speed of light in vacuum; and F represents the field strength of the incident laser. The optical near fields are taken care of by the exact enhancement profile that is extracted from optical simulations [47] and fitted using a linear function of distance, $\beta(z) = \beta_{Au} - (\beta_{Au} - \beta_D)z/d$, with $\beta(0) = \beta_{Au}$ at the Au surface and $\beta(d) = \beta_D$ at the dielectric-vacuum interface, respectively. In the free space region, $z > d$, the potential profile reads,

$$\phi(z,t) = W + E_F - eF\cos\omega t\left(\frac{\beta_{Au} - \beta_D}{2}d + \beta_D z\right) \quad (5.2)$$

where the field enhancement is assumed constant β_D. To ensure a fair comparison, our optical simulations employ exactly the same settings for both bare and coated field emitters, but we set $n = 1$ to the dielectric for the bare emitter. As a result, the potential profiles described above also apply to the bare emitter, where we set the electron affinity $\chi = 0$ for the dielectric.

We plot in Figure 5.1(b) their potential barrier profiles $\phi(z, t = 0)$ induced by a different incident laser. Clearly, the presence of a dielectric coating not only reduces the height of the potential barrier due to the electron affinity of the dielectric layer, χ, but also significantly narrows the barrier, because of the much stronger field enhancement at the Au surface, β_{Au}. This barrier narrowing effect becomes even more profound for larger incident laser fields, as indicated by blue dashed lines in Fig. 5.1(b).

Despite the barrier narrowing effect from the dielectric coatings, electrons inside the metal now need to overcome two barriers to get photoemitted (Figure 5.1(b)), for example via multiphoton absorption, photo-assisted tunneling through either vacuum or the dielectric layer, or direct optical field tunneling. The probability for each of these processes depends on the electron initial energy ε and the overall potential barrier for a given incident laser field F. Here, ε is the longitudinal energy of electrons inside the metal impinging on the metal surface. To calculate the photoemission current, we employ the quantum theory developed in Sec. 2.2.

Therefore, we first need to approximate the irregular "double-barrier" potential profiles with an effective triangular barrier, as exemplified in Fig. 5.2(a). Here, the effective work function of the coated Au is fixed at $W_{eff} = W - \chi$. For an electron inside the metal with an initial energy ε, it would originally see an irregular potential barrier at the metal surface (left of Fig. 5.2(a)). Correspondingly, the effective triangular barrier (right of Fig. 5.2(a)) has the same barrier height as the original barrier, $W_{eff} + E_F - \varepsilon$, for electrons at energy level ε, but with potential energy dropping linearly as a function of the distance away from the metal surface z. The area under the two barriers is kept the same (cf. the red-shaded area S vs the blue-shaded area S' in Fig. 5.2(a)), from which the effective field enhancement factor $\beta_{eff}(\varepsilon)$ can be determined for electrons with initial energy ε. As the area under the irregular double barrier changes nonlinearly with both the electron initial energy ε and the field strength of the incident laser F, the effective field enhancement factor β_{eff} is also a function of ε and F. This effective triangular-barrier approximation is plausible as the electron transmission is insensitive to the actual shape of the barrier, but is predominantly determined by the "area under the curve" according to the WKBJ approximation [106], [200], which has been previously verified for photoemission [38], [49], [62], [100], [119]. We also compare this effective single-triangular-barrier quantum photoemission model based on this approximation to a double-barrier Fowler–Nordheim equation used in the "simple-man" model [183], [184] and exact analytical quantum model in Sec. 5.4.

In Fig. 5.2(b), we plot the ε-dependent effective optical field enhancement factor β_{eff} as a function of the field strength of the incident laser F at three representative electron initial energies ε for both coated and bare photoemitters. The coated emitter has improved β_{eff} over the bare emitter only for F exceeding a certain threshold, e.g., 0.018 V/nm for Fermi electrons with $\varepsilon = E_F$. This can be explained by the barrier profiles in Fig. 5.1(b). When F is small (black solid lines), the second barrier peak at the dielectric-vacuum interface can be higher than that at the Au surface. This results in β_{eff} smaller than that in the bare emitter due to the double-barrier profile. But when F is medium to large (blue dashed lines), the second barrier peak is lowered, and β_{eff} is predominantly determined by the significantly increased field enhancement at the Au surface β_{Au}.

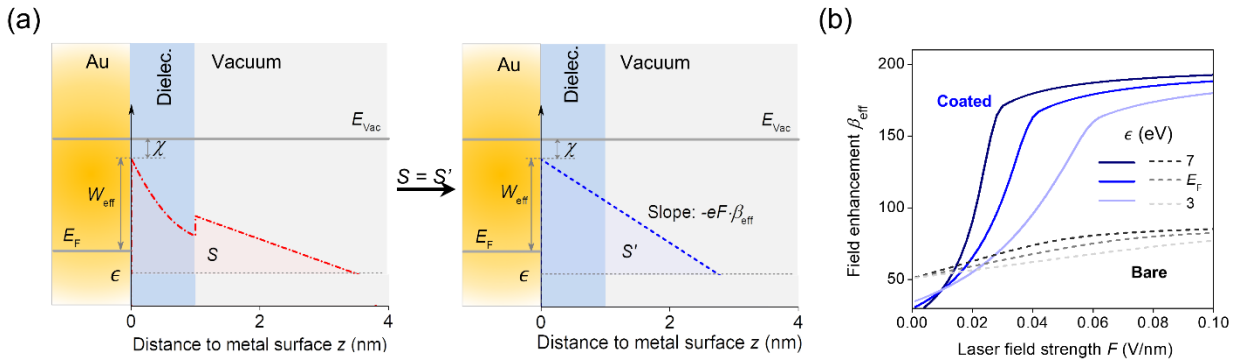

Figure 5.2 (a) Triangular-barrier approximation: with fixed effective work function $W_{eff} = W - \chi$, an effective field enhancement β_{eff} is defined for each electron initial energy ε to maintain the same area under the barriers: $S' = S$. (b) Calculated β_{eff} for three representative ε.

5.2.3 Results and Discussion

The calculated emission current density J as a function of the field strength of the incident laser F is shown in Fig. 5.3(a). In regime I where $F < 0.014$ V/nm, the emission current density from the coated Au tip is close to that from the bare tip, because of the smaller effective enhancement factor β_{eff}, as indicated by the lowered but widened barrier for Fermi electrons at $F = 0.01$ V/nm (inset). However, in regime II where $F > 0.014$ V/nm, the coated Au photoemitter outperforms the bare photoemitter, due to the combined effects of increased β_{eff} and lowered potential barrier, e.g., for Fermi electrons at $F = 0.1$ V/nm (inset). For laser fields over a wide range of $F = 0.014 - 0.1$ V/nm, J from the coated photoemitter is enhanced by at least 2 orders of magnitude as compared to the bare emitter. The threshold laser field of 0.014 V/nm, at which the coated emitter outperforms the bare emitter, can also be derived when β_{eff} of the coated emitter exceeds that of the bare emitter for Fermi electrons, i.e., 0.018 V/nm in Fig. 5.2(b). Interestingly, the increment of the current density J from the coated emitter slows down at higher incident laser fields $F > 0.05$ V/nm (Fig. 5.3(a)), due to the saturation of β_{eff} at larger F (Fig. 5.2(b)). The decreased slope suggests that the coated emitter has probably entered into the optical field tunneling regime, as it follows the Fowler–Nordheim current density scaling law [45], [119].

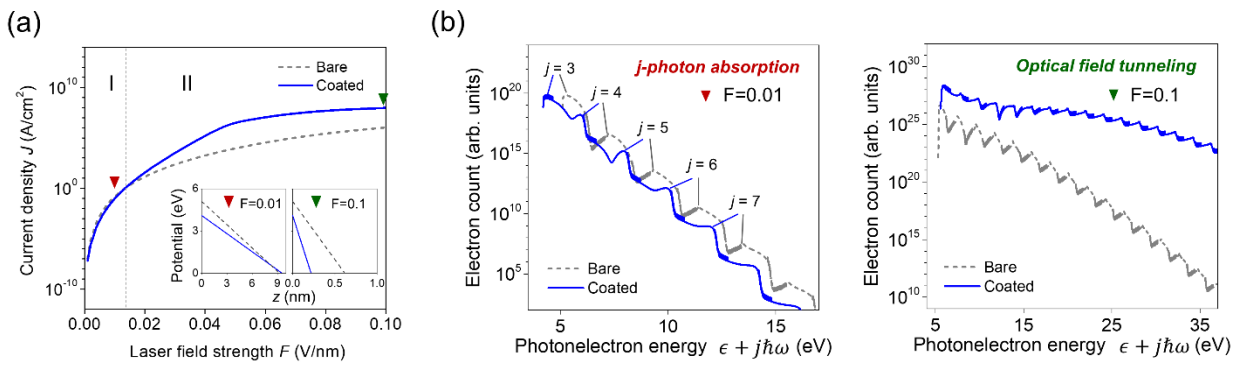

Figure 5.3 (a) Calculated photoemission current density J as a function of the field strength of the incident laser. (b) Photoelectron energy spectra via j-photon absorption (with respect to E_F) at $F = 0.01$ or 0.1 V/nm. In all calculations, the dielectric coating has $d = 1$ nm, $n = 1.5$, and $\chi = 0.9$ eV.

To better understand the photoemission mechanism, we plot the photoelectron energy spectra for two representative incident laser fields in Fig. 5.3(b). At $F = 0.01$ V/nm, the spectra exhibit distinct multiphoton peaks, whose magnitudes decay rapidly with energy. The dominant peaks correspond to three-photon absorption, as the ratio of barrier height to photon energy $W_{eff}/\hbar\omega > 2$ for both bare and coated photoemitters. At larger field $F = 0.1$ V/nm, the spectrum of the coated emitter becomes significantly broadened, reaching a plateau; meanwhile, the multiphoton peaks are severely smeared out. The broadening of the spectrum is ascribable to the increased contributions of higher-order photon processes at large incident laser fields [38], as electrons need to absorb sufficient photon energy to overcome the increased ponderomotive energy, $U_p = e^2(\beta_{eff}F)^2/4m\omega^2$, in order to emit. Classically, the plateau also signifies the back-propagation and rescatterings of electrons in an optical field tunneling process [11], [49], [184]. Therefore, the features of broadening and the plateau in the energy spectrum for the coated photoemitter indicate a more rapid transition from multiphoton absorption to optical field tunneling [24], [38], [49]. To be quantitative, the transition point can be indicatively determined by a local Keldysh parameter at the tip $\gamma_{loc} = \omega\sqrt{2mW_{eff}}/e\beta_{eff}F \approx 1$ [24], [38], [49], [119], [120], which gives a corresponding transition incident field strength of 0.10 (or 0.32) V/ nm for the coated (or bare) field emitter. Alternatively, the transition point could be nominally marked by observing the termination of the scaling $J \propto F^{2j}$ with $j = 3$, which indicates the exit of the three-photon absorption regime, yielding a transition incident field strength of 0.05 (or 0.17) V/nm for the coated (or bare) field emitter. In either way, the coated emitter reaches the optical field tunneling regime at less than one-third of the incident laser field F as compared to the bare

emitter. In other words, the optical field tunneling regime can be accessed at an incident laser intensity of about 10 times smaller with the dielectric coating.

5.3 1D Exact Analytical Quantum Model

5.3.1 Formulation

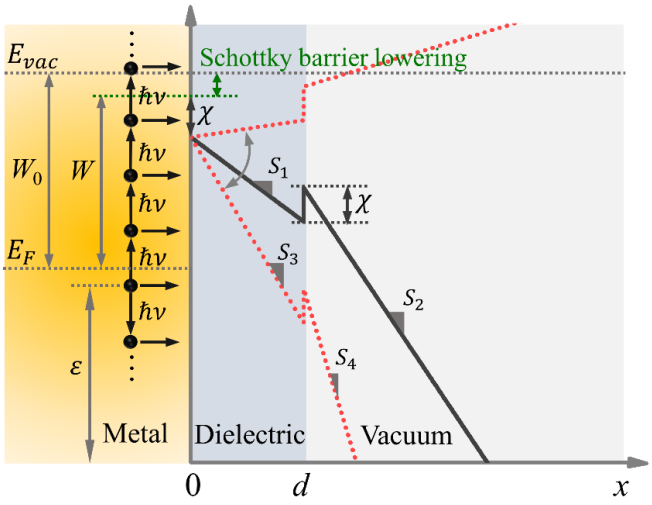

Figure 5.4 Photoemission from a flat metal surface coated with a dielectric under a laser electric field and a dc bias. The metal-dielectric interface is located at $x = 0$, and the coating's thickness is d. The metal has Fermi energy E_F and nominal work function of W_0. The effective work function $W = W_0 - \Delta W$, with the Schottky barrier lowering $\Delta W = 2\sqrt{e^3 F_0^{diel}/16\pi\varepsilon_0\varepsilon_{diel}}$ when the maximum of the potential barrier including image charge potential is in the coating or $\Delta W = 2\sqrt{e^3 F_0/16\pi\varepsilon_0}$ when the potential maximum is in the vacuum. The dielectric has an electron affinity of χ and a relative permittivity of ε_{diel}. The laser field strengths are F_1 in the vacuum and F_1^{diel} in the coating. The dc field strengths are F_0 in the vacuum and F_0^{diel} in the coating. The electron incident longitudinal energy is ε. The black solid line represents the potential profile under the dc field F_0 only, and the red dotted lines are for the time-dependent potential profile due to both F_0 and F_1. Slopes of the potential profile, denoted as S_1, S_2, S_3, and S_4, are $-eF_0^{diel}$, $-eF_0$, $-e(F_0^{diel} + F_1^{diel})$, and $-e(F_0 + F_1)$, respectively.

In the 1D model (see Fig. 5.4), electrons with initial longitudinal energy ε are emitted from the flat metal surface coated with a nanoscale-thick dielectric, driven by a laser field and a dc bias. The laser field and dc bias field are perpendicular to the metal surface. For simplicity, the scattering effects of photoexcited electrons with other electrons and phonons in the metal and dielectric, the charge trapping effect in the dielectric, are ignored [25], [38], [125]. Therefore, the time-varying potential barrier in those three regions, i.e., metal, dielectric, and vacuum, reads,

$$\phi(x,t)=\begin{cases}0, & x<0\\ V_0-\chi-eF_0^{diel}x-eF_1^{diel}x\cos\omega t, & 0\le x<d\\ V_0+ed\left(F_0-F_0^{diel}\right)+ed\left(F_1-F_1^{diel}\right)\cos\omega t-eF_0x-eF_1x\cos\omega t, & x\ge d\end{cases} \tag{5.3}$$

where $V_0=W+E_F$, with E_F the Fermi energy of the metal and $W=W_0-\Delta W$ the effective work function including the potential barrier lowering by the Schottky effect due to the dc electric field F_0, $\Delta W=2\sqrt{e^3F_0^{diel}/16\pi\varepsilon_0\varepsilon_{diel}}$ when the maximum of the potential barrier including image charge potential is in the coating or $\Delta W=2\sqrt{e^3F_0/16\pi\varepsilon_0}$ when the potential maximum is in the vacuum; χ is the electron affinity of the dielectric; e is the positive elementary charge; F_0 and F_1 are the dc electric field and laser electric field in the vacuum respectively; F_0^{diel} and F_1^{diel} are the dc and laser electric field inside the dielectric respectively; ω is the angular frequency of the laser field; and d is the thickness of the dielectric. For perfectly flat surface, $F_0^{diel}=F_0/\varepsilon_{diel}$ and $F_1^{diel}=F_1/\varepsilon_{diel}$ inside the dielectric with ε_{diel} the relative permittivity of the dielectric.

The electron wave functions $\psi(x,t)$ in the metal, dielectric, and vacuum are obtained by solving the time-dependent Schrödinger equation,

$$i\hbar\frac{\partial\psi(x,t)}{\partial t}=-\frac{\hbar^2}{2m}\frac{\partial^2\psi(x,t)}{\partial x^2}+\phi(x,t)\psi(x,t) \tag{5.4}$$

where $\hbar$ is the reduced Planck's constant; m is the electron effective mass, set to the electron rest mass in all three regions for simplicity; and $\phi(x,t)$ is the potential given in Eq. (5.3).

The exact solution to Eq. (5.4) in the metal ($x<0$) is

$$\psi_I(x,t)=e^{-i\frac{\varepsilon}{\hbar}t+ik_0x}+\sum_{n=-\infty}^{\infty}R_{1n}e^{-i\frac{\varepsilon+n\hbar\omega}{\hbar}t-ik_nx}, \qquad x<0 \tag{5.5}$$

where $k_0=\sqrt{2m\varepsilon/\hbar^2}$ and $k_n=\sqrt{2m(\varepsilon+n\hbar\omega)/\hbar^2}$. It represents the superposition of the incident plane wave with electron incident longitudinal energy ε, and a set of reflected waves with energy of $\varepsilon+n\hbar\omega$ after photon absorption ($n>0$) or emission ($n<0$) processes. R_{1n} is the reflection coefficient.

In the dielectric ($0\le x<d$), the solution to Eq. (5.4) is obtained by following Truscott transformation and separation of variables [25], [38], [91]–[93], [121], [125],

$$\psi_{II}(x,t) = \sum_{n=-\infty}^{\infty} T_{2n} \exp\left[i\sqrt{\frac{2m}{\hbar^2}E_{2n}}\left(x + \frac{eF_1^{diel}\cos\omega t}{m\omega^2}\right)\right]\Theta(x,t) + \sum_{n=-\infty}^{\infty} R_{2n} \exp\left[-i\sqrt{\frac{2m}{\hbar^2}E_{2n}}\left(x + \frac{eF_1^{diel}\cos\omega t}{m\omega^2}\right)\right]\Theta(x,t)\,, 0 \le x < d \tag{5.6a}$$

for $F_0 = 0$, or

$$\psi_{II}(x,t) = \sum_{n=-\infty}^{\infty} \left[T_{2n}[Ai(-\zeta_n) - iBi(-\zeta_n)] + R_{2n}[Ai(-\zeta_n) + iBi(-\zeta_n)]\right]\Gamma(x,t)\,, 0 \le x < d \tag{5.6b}$$

for $F_0 \neq 0$, where T_{2n} and R_{2n} are the transmission coefficient and reflection coefficient of electron waves through the *n*th channel in the dielectric, respectively; $E_{2n} = \varepsilon + n\hbar\omega - U_{p2} - V_{20}$ is the drift kinetic energy in the dielectric, with the ponderomotive energy $U_{p2} = \frac{e^2\left(F_1^{diel}\right)^2}{4m\omega^2}$ and $V_{20} = E_F + W - \chi$; $\Theta(x,t) = \exp\left[-i\frac{\varepsilon+n\hbar\omega}{\hbar}t + i\frac{eF_1^{diel}\sin\omega t}{\hbar\omega}x + i\frac{e^2\left(F_1^{diel}\right)^2\sin 2\omega t}{8\hbar m\omega^3}\right]$; $\Gamma(x,t) = \exp\left[-i\frac{e^2F_0^{diel}F_1^{diel}\sin\omega t}{\hbar m\omega^3}\right]\Theta(x,t)$; $\zeta_n = \left(x + \frac{eF_1^{diel}\cos\omega t}{m\omega^2} + \frac{E_{2n}}{eF_0^{diel}}\right)\left(\frac{2meF_0^{diel}}{\hbar^2}\right)^{1/3}$. ψ_{II} represents the superposition of the forward traveling waves and the reflected waves in the dielectric.

In the vacuum ($x \ge d$), the exact solution to Eq. (5.4) is

$$\psi_{III}(x,t) = \sum_{n=-\infty}^{\infty} T_{3n} \exp\left[i\sqrt{\frac{2m}{\hbar^2}E_{3n}}\left(x + \frac{eF_1\cos\omega t}{m\omega^2}\right)\right]\Xi(x,t)\,, x \ge d \tag{5.7a}$$

for $F_0 = 0$, or

$$\psi_{III}(x,t) = \sum_{n=-\infty}^{\infty} T_{3n}[Ai(-\eta_n) - iBi(-\eta_n)] \exp\left[-i\frac{e^2F_0F_1\sin\omega t}{\hbar m\omega^3}\right]\Xi(x,t), x \ge d \tag{5.7b}$$

for $F_0 \neq 0$, where T_{3n} is the transmission coefficient in the vacuum; $E_{3n} = \varepsilon + n\hbar\omega - U_{p3} - V_{30}$ is the drift kinetic energy in the vacuum, with the ponderomotive energy $U_{p3} = \frac{e^2F_1^2}{4m\omega^2}$ and $V_{30} = W + E_F + ed\left(F_0 - F_0^{diel}\right)$ for $F_0 \neq 0$ or $V_{30} = W + E_F$ for $F_0 = 0$; $\Xi(x,t) =$

$\exp\left[-i\frac{ed\left(F_1-F_1^{diel}\right)\sin\omega t}{\hbar\omega}-i\frac{\varepsilon+n\hbar\omega}{\hbar}t+i\frac{eF_1\sin\omega t}{\hbar\omega}x+i\frac{e^2F_1^2\sin 2\omega t}{8\hbar m\omega^3}\right]$; $\eta_n=\left(x+\frac{eF_1\cos\omega t}{m\omega^2}+\frac{E_{3n}}{eF_0}\right)\left(\frac{2meF_0}{\hbar^2}\right)^{1/3}$. ψ_{III} denotes the outgoing waves traveling to the vacuum.

Continuity of the wave function and its derivative at both metal-dielectric interface ($x=0$) and dielectric-vacuum interface ($x=d$) and Fourier transform yield the solution for R_{1n}, T_{2n}, R_{2n}, and T_{3n},

$$\delta(l)+R_{1l}=\sum_{n=-\infty}^{\infty}T_{2n}P_{1n(n-l)}+\sum_{n=-\infty}^{\infty}R_{2n}Q_{1n(n-l)} \tag{5.8a}$$

$$k_0\delta(l)-k_lR_{1l}=\sum_{n=-\infty}^{\infty}T_{2n}P_{2n(n-l)}+\sum_{n=-\infty}^{\infty}R_{2n}Q_{2n(n-l)} \tag{5.8b}$$

$$\sum_{n=-\infty}^{\infty}T_{2n}\,P_{3n(n-l)}+\sum_{n=-\infty}^{\infty}R_{2n}Q_{3n(n-l)}=\sum_{n=-\infty}^{\infty}T_{3n}Z_{3n(n-l)} \tag{5.8c}$$

$$\sum_{n=-\infty}^{\infty}T_{2n}P_{4n(n-l)}+\sum_{n=-\infty}^{\infty}R_{2n}Q_{4n(n-l)}=\sum_{n=-\infty}^{\infty}T_{3n}Z_{4n(n-l)} \tag{5.8d}$$

where δ is the Dirac delta function; $P_{1nl}=\frac{1}{2\pi}\int_0^{2\pi}P_{1n}(\omega t)e^{-il\omega t}d(\omega t)$, $Q_{1nl}=\frac{1}{2\pi}\int_0^{2\pi}Q_{1n}(\omega t)e^{-il\omega t}d(\omega t)$, $P_{2nl}=\frac{1}{2\pi}\int_0^{2\pi}P_{2n}(\omega t)e^{-il\omega t}d(\omega t)$, $Q_{2nl}=\frac{1}{2\pi}\int_0^{2\pi}Q_{2n}(\omega t)e^{-il\omega t}d(\omega t)$, $P_{3nl}=\frac{1}{2\pi}\int_0^{2\pi}P_{3n}(\omega t)e^{-il\omega t}d(\omega t)$, $Q_{3nl}=\frac{1}{2\pi}\int_0^{2\pi}Q_{3n}(\omega t)e^{-il\omega t}d(\omega t)$, $Z_{3nl}=\frac{1}{2\pi}\int_0^{2\pi}Z_{3n}(\omega t)e^{-il\omega t}d(\omega t)$, $P_{4nl}=\frac{1}{2\pi}\int_0^{2\pi}P_{4n}(\omega t)e^{-il\omega t}d(\omega t)$, $Q_{4nl}=\frac{1}{2\pi}\int_0^{2\pi}Q_{4n}(\omega t)e^{-il\omega t}d(\omega t)$, $Z_{4nl}=\frac{1}{2\pi}\int_0^{2\pi}Z_{4n}(\omega t)e^{-il\omega t}d(\omega t)$ are the Fourier transform coefficients. For $F_0=0$, we have

$$P_{1n}(\omega t)=\exp\left[i\sqrt{\frac{2m}{\hbar^2}E_{2n}}\left(\frac{eF_1^{diel}\cos\omega t}{m\omega^2}\right)\right]\rho(\omega t) \tag{5.9a}$$

$$Q_{1n}(\omega t)=\exp\left[-i\sqrt{\frac{2m}{\hbar^2}E_{2n}}\left(\frac{eF_1^{diel}\cos\omega t}{m\omega^2}\right)\right]\rho(\omega t) \tag{5.9b}$$

$$P_{2n}(\omega t)=P_{1n}(\omega t)\left[\sqrt{\frac{2m}{\hbar^2}E_{2n}}+\frac{eF_1^{diel}\sin\omega t}{\hbar\omega}\right] \tag{5.9c}$$

$$Q_{2n}(\omega t) = Q_{1n}(\omega t)\left[-\sqrt{\frac{2m}{\hbar^2}E_{2n}} + \frac{eF_1^{diel}\sin\omega t}{\hbar\omega}\right] \tag{5.9d}$$

$$P_{3n}(\omega t) = \exp\left[i\sqrt{\frac{2m}{\hbar^2}E_{2n}}\left(d + \frac{eF_1^{diel}\cos\omega t}{m\omega^2}\right)\right]\rho(\omega t) \tag{5.9e}$$

$$Q_{3n}(\omega t) = \exp\left[-i\sqrt{\frac{2m}{\hbar^2}E_{2n}}\left(d + \frac{eF_1^{diel}\cos\omega t}{m\omega^2}\right)\right]\rho(\omega t) \tag{5.9f}$$

$$Z_{3n}(\omega t) = \exp\left[i\sqrt{\frac{2m}{\hbar^2}E_{3n}}\left(d + \frac{eF_1\cos\omega t}{m\omega^2}\right)\right]\varrho(\omega t) \tag{5.9g}$$

$$P_{4n}(\omega t) = P_{3n}(\omega t)\left[\sqrt{\frac{2m}{\hbar^2}E_{2n}} + \frac{eF_1^{diel}\sin\omega t}{\hbar\omega}\right] \tag{5.9h}$$

$$Q_{4n}(\omega t) = Q_{3n}(\omega t)\left[-\sqrt{\frac{2m}{\hbar^2}E_{2n}} + \frac{eF_1^{diel}\sin\omega t}{\hbar\omega}\right] \tag{5.9i}$$

$$Z_{4n}(\omega t) = Z_{3n}(\omega t)\left[\sqrt{\frac{2m}{\hbar^2}E_{3n}} + \frac{eF_1\sin\omega t}{\hbar\omega}\right]. \tag{5.9j}$$

with $\rho(\omega t) = \exp\left[i\frac{e^2\left(F_1^{diel}\right)^2\sin 2\omega t}{8\hbar m\omega^3}\right]$ and $\varrho(\omega t) = \exp\left[i\frac{e^2F_1^2\sin 2\omega t}{8\hbar m\omega^3}\right]$.

For $F_0 \neq 0$, we have,

$$P_{1n}(\omega t) = s\big(\zeta_n(x=0)\big)\Upsilon(\omega t) \tag{5.10a}$$

$$Q_{1n}(\omega t) = r\big(\zeta_n(x=0)\big)\Upsilon(\omega t) \tag{5.10b}$$

$$P_{2n}(\omega t) = \left[\frac{eF_1^{diel}\sin\omega t}{\hbar\omega}s\big(\zeta_n(x=0)\big) + \kappa_2 t\big(\zeta_n(x=0)\big)\right]\Upsilon(\omega t) \tag{5.10c}$$

$$Q_{2n}(\omega t) = \left[\frac{eF_1^{diel}\sin\omega t}{\hbar\omega}r\big(\zeta_n(x=0)\big) + \kappa_2 u\big(\zeta_n(x=0)\big)\right]\Upsilon(\omega t) \tag{5.10d}$$

$$P_{3n}(\omega t) = s\big(\zeta_n(x=d)\big)\Upsilon(\omega t) \tag{5.10e}$$

$$Q_{3n}(\omega t) = r\big(\zeta_n(x=d)\big)\Upsilon(\omega t) \tag{5.10f}$$

$$Z_{3n}(\omega t) = v\big(\eta_n(x=d)\big)\Lambda(\omega t) \tag{5.10g}$$

$$P_{4n}(\omega t) = \left[\frac{eF_1^{diel}\sin\omega t}{\hbar\omega} s\big(\zeta_n(x=d)\big) + \kappa_2 t\big(\zeta_n(x=d)\big)\right]\Upsilon(\omega t) \tag{5.10h}$$

$$Q_{4n}(\omega t) = \left[\frac{eF_1^{diel}\sin\omega t}{\hbar\omega} r\big(\zeta_n(x=d)\big) + \kappa_2 u\big(\zeta_n(x=d)\big)\right]\Upsilon(\omega t) \tag{5.10i}$$

$$Z_{4n} = \left[\frac{eF_1\sin\omega t}{\hbar\omega} v\big(\eta_n(x=d)\big) + \kappa_3 w\big(\eta_n(x=d)\big)\right]\Lambda(\omega t) \tag{5.10j}$$

with $\Upsilon(\omega t) = \exp\left[-i\frac{e^2F_0^{diel}F_1^{diel}\sin\omega t}{\hbar m\omega^3} + i\frac{e^2\left(F_1^{diel}\right)^2\sin 2\omega t}{8\hbar m\omega^3}\right]$, $s(\zeta_n) = Ai(-\zeta_n) - iBi(-\zeta_n)$, $r(\zeta_n) = Ai(-\zeta_n) + iBi(-\zeta_n)$, $t(\zeta_n) = iAi'(-\zeta_n) + Bi'(-\zeta_n)$, $u(\zeta_n) = iAi'(-\zeta_n) - Bi'(-\zeta_n)$, $\kappa_2 = \left(\frac{2meF_0^{diel}}{\hbar^2}\right)^{1/3}$, $\Lambda(\omega t) = \exp\left[-i\frac{e^2F_0F_1\sin\omega t}{\hbar m\omega^3} + i\frac{e^2F_1^2\sin 2\omega t}{8\hbar m\omega^3}\right]$,$v(\eta_n) = Ai(-\eta_n) - iBi(-\eta_n)$, $w(\eta_n) = iAi'(-\eta_n) + Bi'(-\eta_n)$, $\kappa_3 = \left(\frac{2meF_0}{\hbar^2}\right)^{1/3}$.

The electron transmission probability, $w(\varepsilon, x, t) = j_v(\varepsilon, x, t)/j_i(\varepsilon)$, is the transmitted electron probability current density in the vacuum j_v relative to the incident electron probability current density in the metal j_i, both of which are calculated from the electron probability current density $j = i\hbar/2m(\psi\nabla\psi^* - \psi^*\nabla\psi)$. It is easy to show the time-averaged transmission probability as

$$D(\varepsilon) = \sum_{n=-\infty}^{\infty} w_n(\varepsilon), \qquad w_n(\varepsilon) = \frac{1}{k_0}\mathrm{Im}\left[i\sqrt{\frac{2m}{\hbar^2}E_{3n}}|T_{3n}|^2\right], \text{for } F_0 = 0, \tag{5.11a}$$

or

$$D(\varepsilon) = \sum_{n=-\infty}^{\infty} w_n(\varepsilon), \qquad w_n(\varepsilon) = \frac{|T_{3n}|^2}{k_0}\mathrm{Im}\left[\frac{i\kappa_3}{\pi}\right], \text{for } F_0 \neq 0 \tag{5.11b}$$

with all parameters defined above.

The electron emission current density is obtained from

$$J = e\int_0^{\infty} D(\varepsilon)N(\varepsilon)d\varepsilon, \tag{5.12}$$

where $D(\varepsilon)$ is given in Eq. (5.11) and $N(\varepsilon) = \frac{mk_BT}{2\pi^2\hbar^3}\ln\left[1 + \exp\left(\frac{E_F-\varepsilon}{k_BT}\right)\right]$ is the flux of electrons impinging normal to the metal-dielectric interface, which is calculated from the three-dimensional (3D) free electron theory of metal [122], [123], [125], with k_B being the Boltzmann's constant and T the temperature.

5.3.2 Keldysh Parameter

The Keldysh parameter γ is a physical indicator of transition from multiphoton absorption to optical field tunneling in photoemission. γ is estimated as the ratio of two time scales [104], [105],

$$\gamma = \frac{4\pi t_t}{T}, \tag{5.13}$$

where $T = 2\pi/\omega$ is the cycle of the optical field, and $t_t = l/v$ is the time of an electron with velocity $v = \sqrt{2W/m}$ tunneling through the potential barrier with a width l, W is the work function of the metal and m is the electron rest mass.

Following the definition of Keldysh parameter, the width of the barrier must be narrowed enough by the optical field that the escaping electrons can traverse the barrier within a fraction of half cycle of the optical field. For the case of photoemission from bare metal surfaces, with the instantaneous lower limit potential profile under a single laser field shown in Fig. 5.5(a), $\gamma = \omega\sqrt{2mW}/eF_1$. In the effective single-barrier quantum model (ESQM), we calculate the Keldysh parameter as $\gamma = \omega\sqrt{2mW_{eff}}/eF_{eff}$ with $W_{eff} = W - \chi$ and F_{eff} effective laser field determined by the slope of the effective single triangular barrier (refer to Sec. 5.2 or Ref. [47] for more details). If we follow Keldysh to calculate γ as the ratio of the tunneling time to the optical period, for photoemission from dielectric-coated metal surface, the expression of γ will depend on the laser field strength. When the applied F_1 is relatively small ($W - edF_1^{diel} > 0$), the incident electron has to tunnel through the potential barrier in the vacuum, as shown in Fig. 5.5(b), and it is found $\gamma = \omega\sqrt{\frac{2m}{W}}\left(W + ed\left(F_1 - F_1^{diel}\right)\right)/eF_1$. When the applied F_1 is relatively large ($W - edF_1^{diel} < 0$), electrons inside the metal can be emitted by tunneling the only potential barrier inside the dielectric, as shown in Fig. 5.5(c), and we find $\gamma = \omega\sqrt{\frac{2m}{W}}(W - \chi)/eF_1^{diel}$.

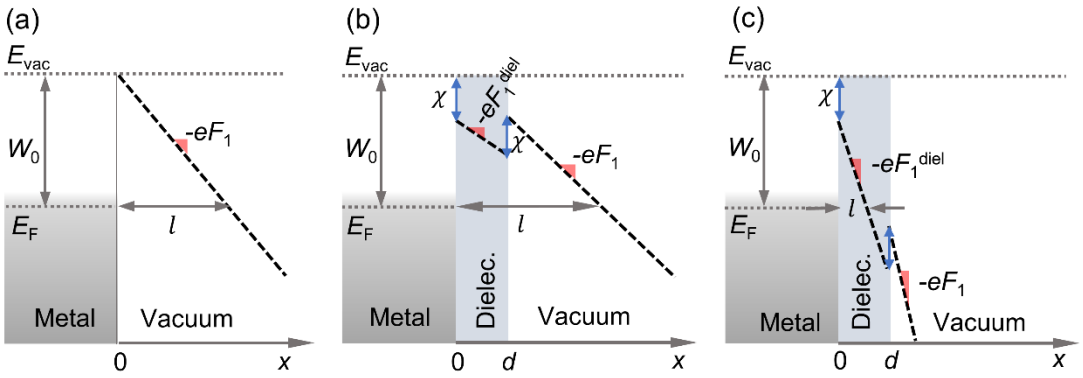

Figure 5.5 Potential profile for photoemission from (a) bare metal surface; (b) dielectric-coated metal surface under a relatively small laser field; (c) dielectric-coated metal surface under a relatively large laser field.

5.3.3 Results and Discussion

Based on the theory developed in Sec. 5.3.1, we provide an analysis of the photoemission from metallic cathodes coated with dielectric. The metal is assumed to be gold, with nominal work function $W_0 = 5.1$ eV and Fermi energy $E_F = 5.53$ eV. The laser has a wavelength of 800 nm, corresponding to the photon energy of 1.55 eV. These are the default properties of the metal and laser respectively, unless prescribed otherwise.

A. Effects of dielectric properties on photoemission from a flat metal surface

Figure 5.6 shows the effects of coating dielectric properties (i.e., thickness d, relative permittivity ε_{diel}, and electron affinity χ) on the electron transmission probability from a flat metal surface. Since most of the photoemission occurs with electron initial energies near Fermi level at ambient temperature, the free electrons inside the metal are assumed to have an initial energy $\varepsilon = E_F$. The electron transmission probability through the nth channel $w_n(\varepsilon = E_F)$ calculated from Eq. (5.11), for dielectrics of different thickness d, relative permittivity ε_{diel}, and electron affinity χ, is plotted in Figs. 5.6(a), 5.6(b), and 5.6(c), respectively. The laser has a field strength of $F_1 = 5$ V/nm. The dc electric field is $F_0 = 0$. It is found that the dominant photoemission is through four-photon absorption (n = 4) under the fields provided, regardless of the dielectric properties. By checking the Keldysh parameter γ, it is found that $\gamma \geq 3.59$ for all the cases in Figs. 5.6(a), 5.6(b), and 5.6(c), indicating the multiphoton absorption process. The dominant channel, n = 4, is consistent with the ratio of the work function to the photon energy $\langle W/\hbar\omega \rangle$, where $\langle \quad \rangle$ represents the next nearest integer to the value inside the bracket. $w_n(\varepsilon = E_F)$ increases with decreasing ε_{diel} or increasing χ, due to the narrowed or reduced barrier in the

dielectric, which is similar to dc field emission from thin dielectric coated surfaces [79]. However, $w_n(\varepsilon = E_F)$ has no clear monotonic dependence on d, as shown in Fig. 5.6(a).

The electron transmission probability $D(\varepsilon = E_F)$, which is a sum of w_n over all channels, is presented as a function of dielectric thickness, relative permittivity, and electron affinity in Figs. 5.6(d), 5.6(e), and 5.6(f), respectively, under various laser field strengths F_1. It is obvious that the transmission probability increases when the laser field strength increases. In Fig. 5.6(d), the transmission probability shows approximately periodic peaks with respect to the dielectric thickness. These peaks are due to resonance in the quantum interference [201] between electron waves transmitted to and reflected from the dielectric-vacuum interface, which forms constructive interference when the dielectric is of a particular thickness (see Figs. 5.7 and 5.9). As the laser field strength increases, peaks on the curves shift towards larger thicknesses, as indicated by the gray dotted line in Fig. 5.6(d). The physics behind this shift lies in that the wavelength of the electron waves inside the dielectric increases with the laser field (see Fig. 8), which can also be indicated by the wavenumber $\sqrt{2mE_{2n}/\hbar^2}$, with $E_{2n} = \varepsilon + n\hbar\omega - U_{p2} - (E_F + W - \chi)$ and $U_{p2} = e^2\left(F_1^{diel}\right)^2/4m\omega^2$.

Figure 5.6(e) shows that the transmission probability $D(\varepsilon = E_F)$ decreases with the relative permittivity of the dielectric, ε_{diel}, for a given laser field, due to the smaller field $F_1^{diel} = F_1/\varepsilon_{diel}$ inside the dielectric. When ε_{diel} is large, e.g., $\varepsilon_{diel} > 2$, F_1^{diel} inside the dielectric would be relatively smaller for a given F_1, thus the incident electron would see a double-triangular potential barrier before emission (see Fig. 5.4), yielding a rapidly decreasing slope in $D(\varepsilon = E_F)$ vs ε_{diel}. When ε_{diel} is small (<2), F_1^{diel} would be larger, such that the incident electron would see only a single-triangular barrier inside the dielectric (since the barrier at the dielectric-vacuum interface would be below the electron initial energy level), yielding a smaller slope. The smaller slope is particularly obvious for $F_1 = 6, 8, \text{and } 10\ \text{V/nm}$ when $\varepsilon_{diel} < 2$. The trends of these curves are found to follow closely those of "area under the curve" in the potential barrier (i.e., WKBJ approximation, see Fig. 5.10).

Figure 5.6(f) shows the effect of the dielectric electron affinity on photoelectron transmission probability, with $\varepsilon_{diel} = 2$, and $d = 1$ nm. $D(\varepsilon = E_F)$ increases with χ, due to the lowering of the potential barrier. There appear distinct resonance peaks on each curve for a given F_1 due to quantum interference. The peaks shift towards a larger χ as the laser field strength

increases, which is indicated by the gray dotted lines in Fig. 5.6(f). Note that the model recovers photoemission from bare metal surfaces [38], [125] when $d = 0$ or when $\chi = 0$ and $\varepsilon_{diel} = 1$ (i.e., vacuum).

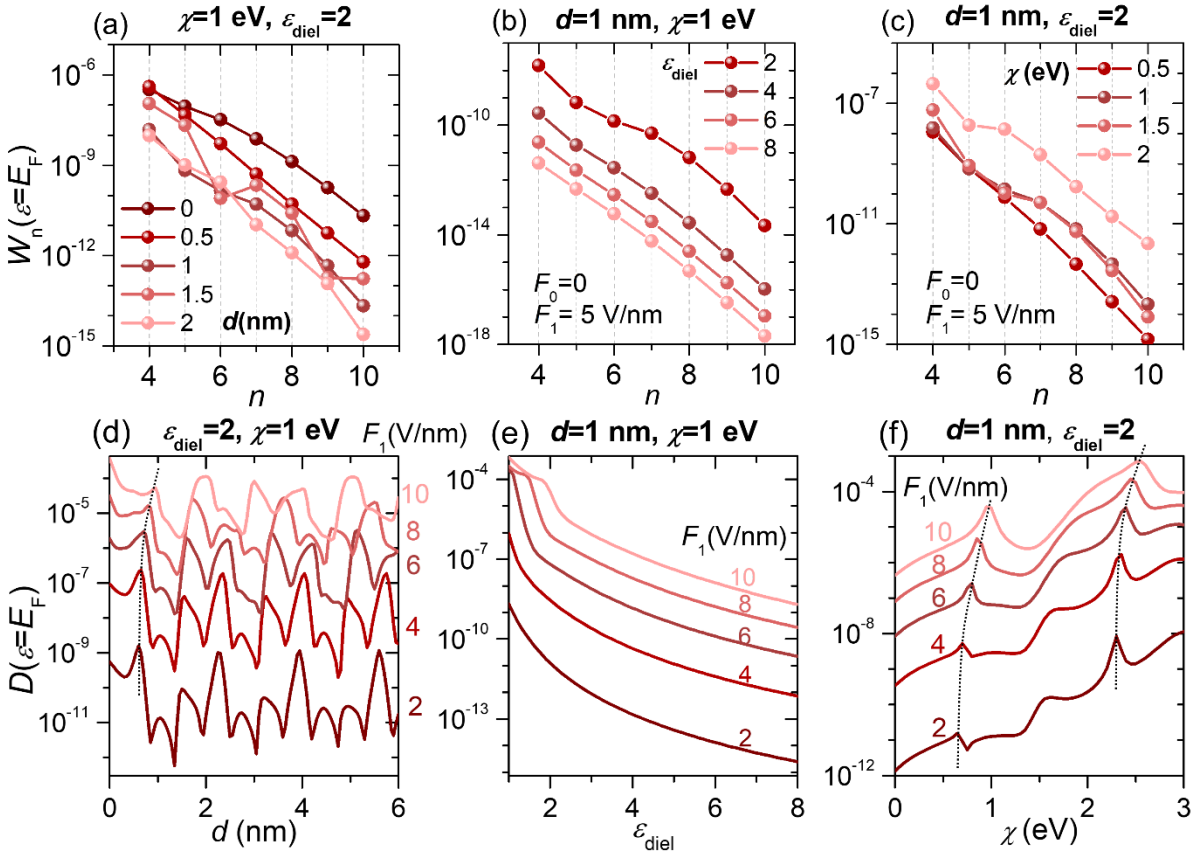

Figure 5.6 Effects of dielectric properties on photoelectron transmission probability from a flat metal surface. Time-averaged electron transmission probability through the nth channel, w_n, calculated from Eq. (5.11), for a dielectric of different (a) thickness d; (b) relative permittivity ε_{diel}; and (c) electron affinity χ. The photoelectron transmission probability $D(\varepsilon = E_F)$ calculated from Eq. (5.11), as a function of dielectric properties (d) thickness d; (e) relative permittivity ε_{diel}; and (f) electron affinity χ, for various laser field strengths. The dc electric field $F_0 = 0$.

The resonance peaks shown in Fig. 5.6(d) are due to the electron wave interference inside the dielectric [79]. In Fig. 5.7, the instantaneous electron waves at $t = 0$, including the wave traveling to the dielectric-vacuum interface ψ_{II}^{t} (blue line), the wave reflected from the dielectric-vacuum interface ψ_{II}^{r} (orange line), as well as the combined wave ψ_{II} (gray line), inside the dielectric of various thicknesses, are plotted. A constructive interference is shown in Fig. 5.7(a) with $d = 2.45$ nm where the resonance peak appears in Fig. 5.6(d) for $F_1 = 6$ V/nm. The incident wave and reflected wave are almost in phase, especially at a distance close to the

dielectric-vacuum interface. Figure 5.7(b) plots the electron waves for $d = 3.8$ nm, which forms a valley point in Fig. 5.6(d) for $F_1 = 6$ V/nm. The incident wave and reflected wave are ~100 degree out of phase, which results in a small transmission probability.

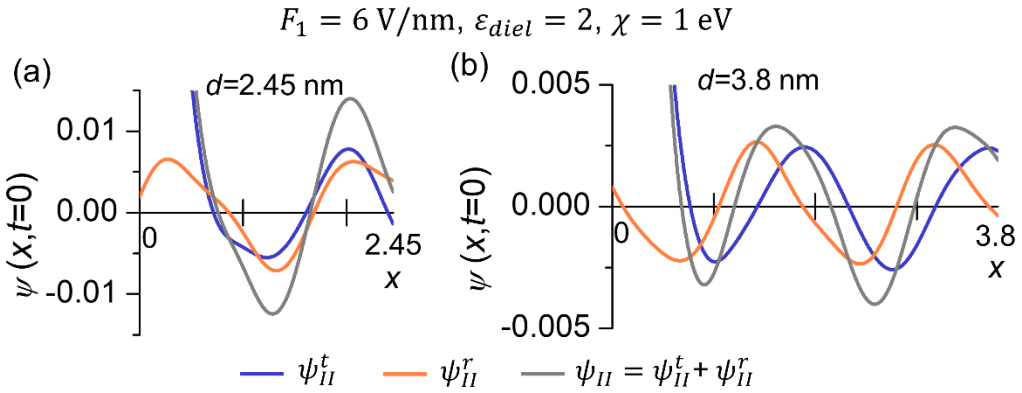

Figure 5.7 Electron waves inside the dielectric of thicknesses: (a) $d = 2.45$ nm (peak on the curve for $F_1 = 6$ V/nm in Fig. 5.6(d)); and (b) 3.8 nm (valley on the curve for $F_1 = 6$ V/nm in Fig. 5.6(d)). The blue curve represents the wave traveling to the dielectric-vacuum interface ψ_{II}^t. The orange curve represents the wave reflected from the dielectric-vacuum interface ψ_{II}^r. The gray curve represents the combination of incident and reflected waves $\psi_{II} = \psi_{II}^t + \psi_{II}^r$. The laser field strength is 6 V/nm. The dielectric has $\chi = 1$ eV and $\varepsilon_{diel} = 2$.

Note that the wavelength from peak to peak may change slightly for a dielectric of certain thicknesses under a given laser field, as shown in Fig. 5.8(a). The wavelength varies with dielectric properties, such as thickness shown in Fig. 5.8(a) and 5.8(b). The laser field strength also has effects on the wavelength. As F_1 increases, the wavelength increases, as demonstrated in Figs. 5.8(a), 5.8(c) and 5.8(d).

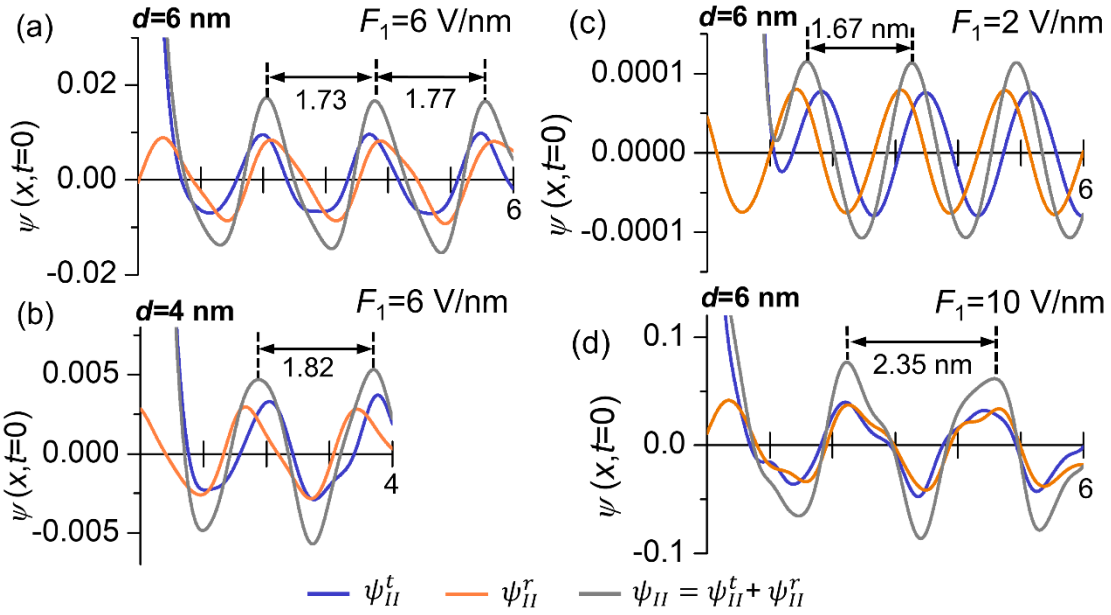

Figure 5.8 Electron waves for (a) $F_1 = 6$ V/nm and $d = 6$ nm; (b) $F_1 = 6$ V/nm and $d = 4$ nm; (c) $F_1 = 2$ V/nm and $d = 6$ nm; and (d) $F_1 = 10$ V/nm and $d = 6$ nm. The blue curve represents the wave traveling to the dielectric-vacuum interface ψ_{II}^t. The orange curve represents the wave reflected from the dielectric-vacuum interface ψ_{II}^r. The gray curve represents the combination of incident and reflected waves $\psi_{II} = \psi_{II}^t + \psi_{II}^r$. The double arrow line indicates the wavelength between peaks. The dielectric has $\chi = 1$ eV and $\varepsilon_{diel} = 2$.

The incident wave and reflected wave inside the dielectric form constructive interference by approximately satisfying the condition,

$$kd = n\pi \text{ or } 2d = n\lambda_e, \text{with } n = 1, 2, 3 \ldots \tag{5.14}$$

where k and λ_e are the electron wavenumber and the wavelength in the dielectric respectively, and d is the dielectric thickness. Using this condition, with an approximately constant "wavelength" $\lambda_e = 1.7$ nm obtained from Fig. 5.8(a), we can predict the dielectric thickness at which interference occurs in the dielectric. The comparison of the predicted resonance thicknesses by Eq. (5.14) and the ones from the quantum model which are denoted as blue dots in Fig. 5.9(a), is provided in Fig. 5.9(b). Those two results show very good quantitative agreement.

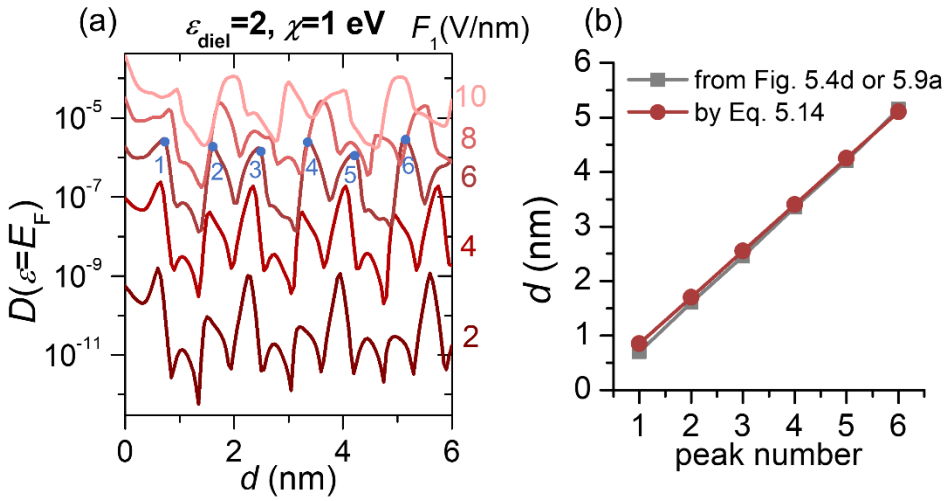

Figure 5.9 (a) Electron transmission probability as a function of dielectric thickness under various laser field strengths, same as Fig. 5.6(d). Blued dots indicate the resonance peaks for $F_1 = 6$ V/nm. (b) A comparison of the predicted resonance dielectric thickness by Eq. (5.14) and resonance dielectric thickness obtained from Fig. 5.6(d) or Fig. 5.9(a) here.

The area enclosed by the potential profile and the electron initial energy provides a good explanation for the slope variation in Fig. 5.6(e) for electron transmission probability as a function of dielectric relative permittivity. The area (shown as red shaded area in Fig. 5.10(a)) reads

$$S = \int_0^{x'} [V(x, t = 0) - \varepsilon]\, dx\,, \tag{5.15}$$

where $V(x, t = 0)$ is the potential barrier provided as Eq. (5.3) at $t = 0$ with $F_0 = 0$, ε is the electron initial energy, and x' is such that $V(x, t = 0) - \varepsilon = 0$.

Figures 5.10(b) and 5.10(c) plot the negative area S and exponential function of normalized negative S as a function of dielectric relative permittivity under various laser fields. Both plots show a similar trend with Fig. 5.6(e), especially the slope change for $F_1 = 8$ and 10 V/nm. It is because electrons would face the only triangular barrier inside the dielectric when ε_{diel} is small and F_1 is large enough, since the barrier at the dielectric-vacuum interface would be below ε.

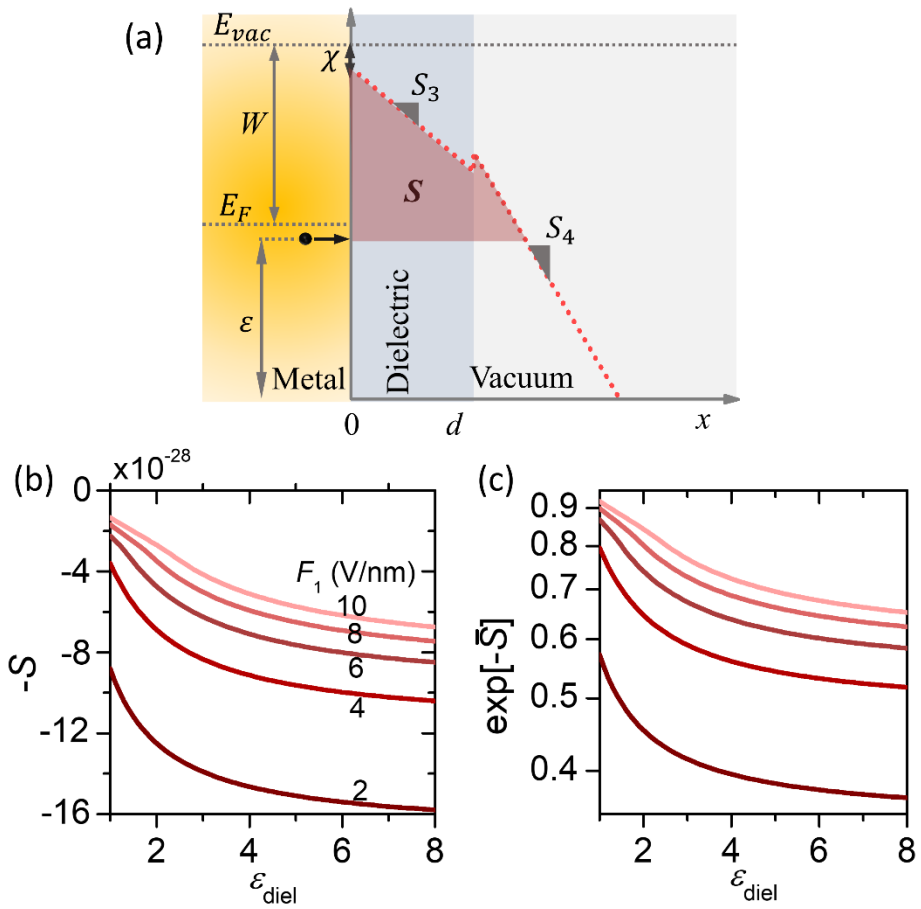

Figure 5.10 (a) Energy diagram for photoemission from dielectric-coated metal surfaces. The red shaded area denotes the area enclosed by the potential profile (at the time instant of peak laser field) and the electron initial energy ε. (b) Negative S as a function of dielectric relative permittivity under various laser field strengths. (c) Exponential function of negative normalized S as a function of dielectric relative permittivity under various laser field strengths. The area S is normalized to S at $\varepsilon_{diel} = 8$ for $F_1 = 2$ V/nm.

The electron transmission probability $D(\varepsilon = E_F)$ is shown as a function of the laser field strength F_1 under different dielectric thickness, relative permittivity, and electron affinity in Figs. 5.11(a), 5.11(b), and 5.11(c), respectively. The applied dc electric field F_0 is 0. The electron transmission probability is well scaled as $D(\varepsilon = E_F) \propto F_1^{2n}$, with $n = 4$, in the small laser field range. The sharp slope change of the curves is observed at $F_1 \approx 11.9$ V/nm (see the vertical blue dashed lines in Fig. 5.11) due to the channel closing effect [38], which indicates the transition from multiphoton absorption to optical field emission. For the chosen parameter ranges, it is found that the dielectric coating has little effects on the laser field strength at which the transition from multiphoton absorption to optical field emission occurs.

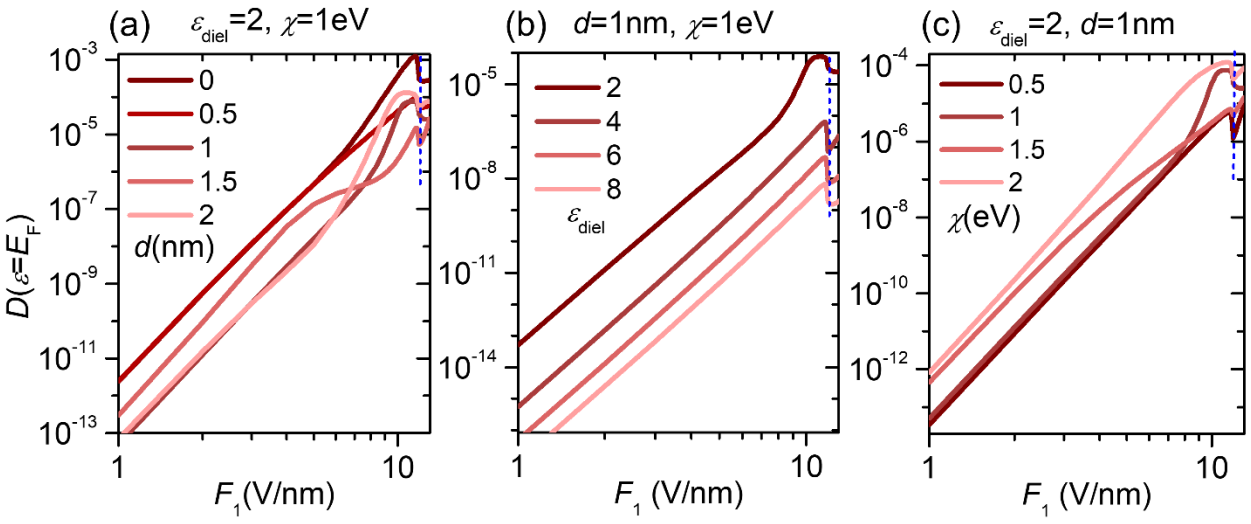

Figure 5.11 The photoelectron transmission probability $D(\varepsilon = E_F)$ calculated from Eq. (5.11), as a function of laser field strength F_1 for different dielectric (a) thickness d; (b) relative permittivity ε_{diel}; and (c) electron affinity χ. The dc electric field F_0 = 0.

Figure 5.12 shows the effects of dielectric properties on photoemission current density. The photoemission current density J, calculated from Eq. (5.12), is plotted as a function of dielectric thickness d in Fig. 5.12(a), for laser field strengths from 2 to 10 V/nm. J decreases with d for $0 < d < 1$ nm. The current density is almost constant for $d > 1$ nm, while there appear some slight resonance peaks, such as the orange dots on the curve for $F_1 = 2$ V/nm. These features are similar to those of dc field emission from dielectric coated surfaces (cf. Fig. 5 of Ref. [79]). The resonances are not as strong as those in Fig. 5.6(d) for $D(\varepsilon = E_F)$ vs d. This is because photoemission current includes the electron emission from all incident energy levels in the metal, which, in combination, smoothens the curve and reduces the strong emission peaks from a single initial energy level. Note that in our model, electron-phonon scattering and electron-electron scattering effects in dielectric are not considered. According to the experiment in [202], a mean free path of a few nanometers has been observed for photoexcited electrons in dielectrics [202], [203]. Therefore, for dielectric thickness smaller than the mean free path, the scattering effect inside the coating may not be important. Figure 5.12(b) shows J as a function of relative permittivity ε_{diel}. The curves exhibit two distinct slopes in the semilog scale plot, which can be inferred from the transmission probability in Fig. 5.6(e). Figure 5.12(c) presents the effects of dielectric electron affinity on photoemission current density. Generally, emission current density increases with electron affinity for a given field strength, due to the lowering of the surface potential barrier. Mild resonant peaks in J are also observed as χ changes.

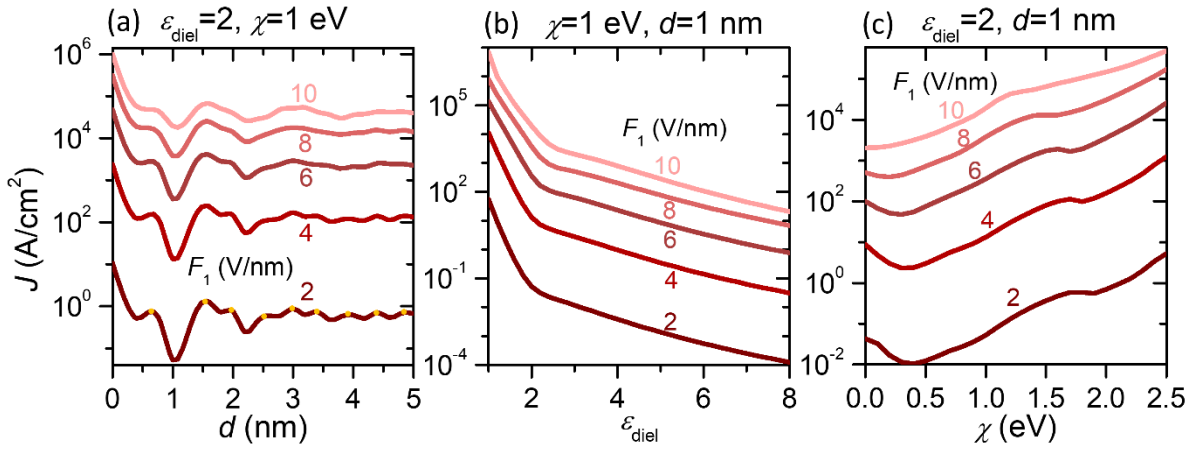

Figure 5.12 The photoelectron emission current density J from a dielectric-coated flat metal surface as a function of dielectric properties (a) thickness d; (b) relative permittivity ε_{diel}; and (c) electron affinity χ, for laser field strengths from 2 to 10 V/nm. The dc field $F_0 = 0$, and temperature $T = 300$ K.

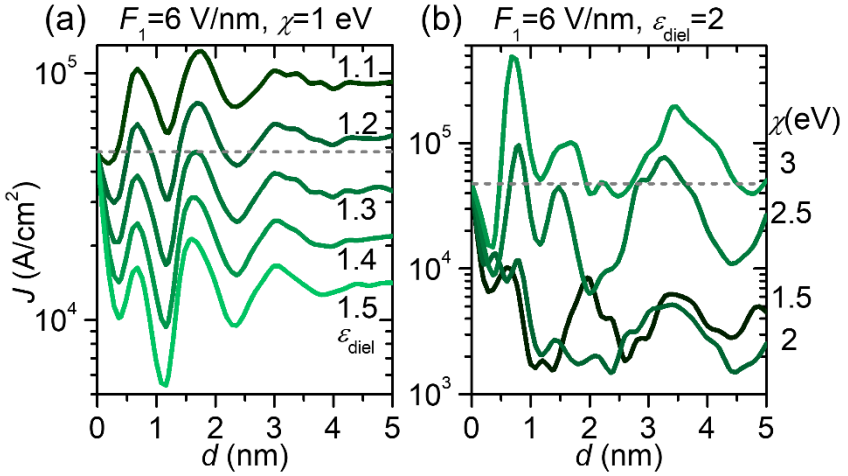

Figure 5.13 The photoemission current density J from a dielectric-coated flat metal surface as a function of dielectric thickness d under a different (a) relative permittivity ε_{diel}; (b) electron affinity χ. The dc electric field $F_0 = 0$.

It is interesting to find that a flat cathode surface with dielectric coating can emit a larger current density than an uncoated case, when the dielectric has sufficiently small relative permittivity ε_{diel} or large electron affinity χ, which would result in a narrowed or lowered potential barrier. Figures 5.13(a) and 5.13(b) provide examples of such cases, as shown in the region above the gray dashed lines. Similar electron emission enhancement phenomenon is also demonstrated for field emission from dielectric-coated surfaces [79]. It should be pointed out that scattering of electrons with phonons, impurities, and even with other electrons inside the dielectric is not considered in the model. Photoelectron emission from ultrathin oxide covered

devices shows an exponential attenuation behavior for the relatively thicker oxide layer (2.5~15.3 nm), with the dominant mean-free-path of the photoexcited electrons inside the SiO_2 ~1.2 nm [202]. Therefore, for dielectric thicker than the mean-free-path, electron scattering effects cannot be ignored.

B. Effects of dc field on photoemission

Figure 5.14 shows the effects of dc electric field on photoemission from dielectric-coated metal surfaces. The transmission probability through different *n* channels from initial energy $\varepsilon = E_F$ under different F_0 is shown in Fig. 5.14(a). As F_0 increases, the dominant emission channel shifts to smaller *n*. The narrowed and lowered (due to Schottky effect) surface potential barrier by the static field enables more photoemission mechanisms, such as photo-assisted field emission ($1 < n < 4$), multiphoton emission ($n < 0$), and direct tunneling ($n = 0$). The electron transmission probability is greatly enhanced by the dc field.

The electron transmission probability $D(\varepsilon = E_F)$ is plotted as a function of dc field F_0 in Fig. 5.14(b) for different laser field strengths. The combined dc field and laser field result in an emission probability significantly larger than that from either field alone. When $F_1 = 0$, the electron transmission probability recovers the dc field emission from dielectric coated surfaces [79].

Figure 5.14(c) shows the emission current density as a function of dc field under various laser field strengths. The shape of the emission current density is similar to the transmission probability from $\varepsilon = E_F$ in Fig. 5.14(b). For $F_0 \lesssim 12\ \mathrm{V/nm}$, the slope of the curves varies with the laser field strength F_1, which indicates that *n*-photon-assisted field tunneling dominates in this range, where n becomes smaller as F_0 increases. When $F_0 \gtrsim 12\ \mathrm{V/nm}$, the slopes of the curves for all four cases are almost the same, because the dominant emission becomes dc field tunneling.

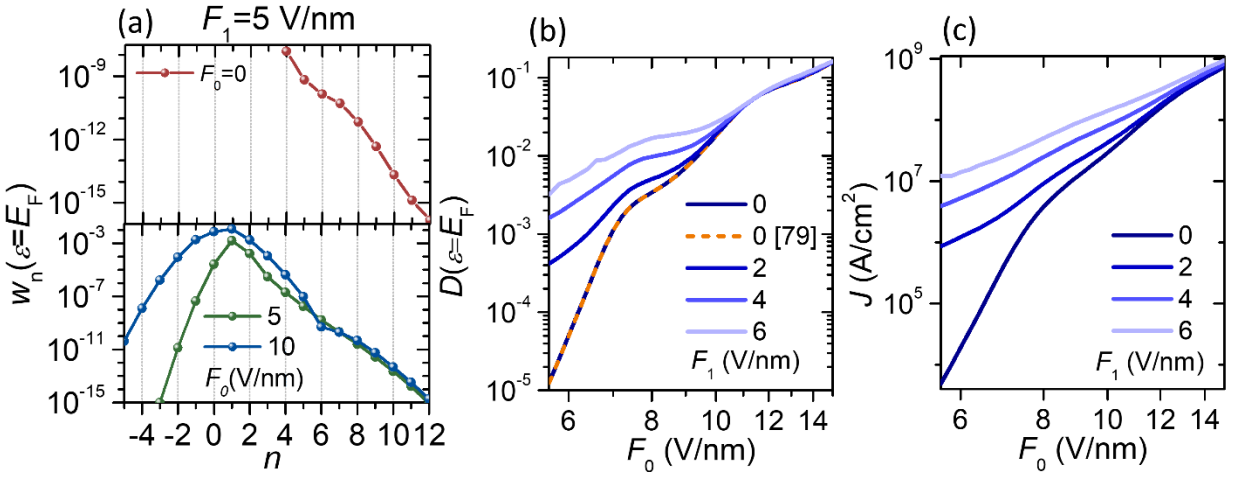

Figure 5.14 Effects of dc field on photoemission from dielectric-coated metal surfaces. (a) Photoemission probability through different n-channels from initial energy level $\varepsilon = E_F$ under various dc fields with the laser field strength $F_1 = 5$ V/nm. (b) Electron transmission probability $D(\varepsilon = E_F)$, and (c) Electron emission current density J, as a function of dc field F_0 under various laser field strengths. The dashed line in (b) is for calculation using Eq. (8) of Ref.[79]. The coating has $\varepsilon_{diel} = 2$, $\chi = 1$ eV, and $d = 1$ nm.

5.4 Comparison of Models

In this section, we compare the results of our exact analytical model with the effective single-triangular-barrier quantum model (ESQM) [47] and modified Fowler-Nordheim (FN) equation [183], [184] for photoemission from dielectric-coated metal surfaces. The description of ESQM is provided in Sec. 5.2.2. A short account of the modified FN equation is provided herein.

5.4.1 Modified Fowler-Nordheim Equation for Double-triangular Barrier

Following the procedure in [183], a modified Fowler-Nordheim equation is formulated. For the scenario of an ultrathin dielectric on a metal surface, a double step barrier is formed. If the zero of energy is taken at Fermi level, the lowermost barrier profile bent by the laser field reads,

$$V(x,t) = \begin{cases} 0, & x < 0, \\ W_{eff} - eF_1^{diel}(t), & 0 \le x < d, \\ W + ed\left(F_1(t) - F_1^{diel}(t)\right) - eF_1(t)x, & x \ge d, \end{cases} \tag{5.16}$$

where W is the nominal work function of the metal; χ and d are the electron affinity and the thickness of the dielectric; $W_{eff} = W - \chi$ is the effective work function at metal-dielectric interface; F_1 and F_1^{diel} are the laser field strengths in the vacuum and in the dielectric respectively; and e is the positive elementary charge. Note that dc field is not considered in this modified Fowler-Nordheim equation.

In the current emission calculation, only the positive half cycle of the laser field is considered. According to the WKBJ approximation, we have the transmission probability,

$$D(\varepsilon, F_1) = \exp[Q(\varepsilon, F_1)], \tag{5.17}$$

where $Q(\varepsilon, F_1) = -2\int_0^{x'} \sqrt{2m[V(x)-\varepsilon]/\hbar^2}\, dx$, m is the effective electron mass, $\hbar$ is the reduced Planck's constant, and x' is such that $V(x) - \varepsilon = 0$. For simplicity, m is set to equal the electron rest mass in all three regions. It is easy to show that,

$$\begin{aligned} Q(\varepsilon, F_1) = -\frac{4}{3}\frac{\sqrt{2m}}{e\hbar F_1^{diel}}\Big[\big(W_{eff}-\varepsilon\big)^{\frac{3}{2}} - H\big(W_{eff} - eF_1^{diel}d - \varepsilon\big)\big(W_{eff} - eF_1^{diel}d - \varepsilon\big)^{\frac{3}{2}}\Big] \\ -\frac{4}{3}\frac{\sqrt{2m}}{eF_1\hbar}H\big(W - eF_1^{diel}d - \varepsilon\big)\big(W - eF_1^{diel}d - \varepsilon\big)^{\frac{3}{2}}. \end{aligned} \tag{5.18}$$

Since most of the emission comes from the immediate neighborhood of the Fermi level, we replace $Q(\varepsilon, F_1)$ with the first two terms of the Taylor expansion for $Q(\varepsilon, F_1)$ at $\varepsilon = E_F = 0$, which reads,

$$Q(\varepsilon, F_1) = -\frac{4}{3}\frac{\sqrt{2m}W^{\frac{3}{2}}}{e\hbar F_1^{diel}(t)}C + 2\frac{\sqrt{2mW}}{e\hbar F_1^{diel}(t)}B\varepsilon \tag{5.19}$$

with

$$\begin{aligned} B = \sqrt{\frac{W_{eff}}{W}} - H\big(W_{eff} - eF_1^{diel}(t)d\big)\sqrt{\frac{W_{eff} - eF_1^{diel}(t)d}{W}} \\ + H\big(W - eF_1^{diel}(t)d\big)\frac{1}{\varepsilon_{diel}}\sqrt{\frac{W - eF_1^{diel}(t)d}{W}} \end{aligned}$$

and

$$\begin{aligned} C = \left(\frac{W_{eff}}{W}\right)^{3/2} - H\big(W_{eff} - eF_1^{diel}(t)d\big)\left[\frac{W_{eff} - eF_1^{diel}(t)d}{W}\right]^{\frac{3}{2}} \\ + H\big(W - eF_1^{diel}(t)d\big)\frac{1}{\varepsilon_{diel}}\left[\frac{W - eF_1^{diel}(t)d}{W}\right]^{\frac{3}{2}}, \end{aligned}$$

where ε_{diel} is the relative permittivity of the dielectric, and $H(x)$ is the Heaviside step function. $F_1^{diel} = F_1/\varepsilon_{diel}$ is used for a perfectly flat dielectric-vacuum interface. The H functions arise from different tunneling scenarios under different field strengths (cf. Fig. 5 in [184]).

The emission current density can be calculated from

$$J = e\int_{-\infty}^{\infty} N(\varepsilon, T)D(\varepsilon, F_1)d\varepsilon\,. \tag{5.20}$$

At a low temperature, $N(\varepsilon,T) = \frac{mk_BT}{2\pi^2\hbar^3}\ln\left[1+\exp\left(\frac{E_F-\varepsilon}{k_BT}\right)\right] \approx \frac{m}{2\pi^2\hbar^3}(E_F-\varepsilon)$. We finally yield the modified Fowler-Nordheim equation for the double-triangular barrier,

$$J(t) = H[F_1(t)]\frac{e^3 {F_1^{diel}}^2(t)}{16\pi^2\hbar W B^2}\exp\left[-\frac{4\sqrt{2m}}{3e\hbar F_1^{diel}(t)}W^{\frac{3}{2}}C\right] \tag{5.21}$$

The time-averaged photoemission current density is

$$J = \frac{\omega}{2\pi}\int_0^{\frac{2\pi}{\omega}} J(t)dt\,, \tag{5.22}$$

where ω is the angular frequency of the laser.

5.4.2 Comparison Results for 1D Flat Cathodes

Figure 5.15 shows the comparison of the three models for photoemission from 1D flat cathodes. The electron emission probability $D(\varepsilon = E_F)$ as a function of the laser field strength F_1 is plotted in Fig. 5.15(a). It can be seen that, for flat surfaces with coatings, the ESQM overestimates the photoemission probability, but the modified FN equation underestimates the photoemission probability, as compared to the exact double-triangular barrier model. ESQM models the double barrier using an effective single triangular barrier based on WKBJ approximation [47], where the effective barrier height is chosen at $W_{eff} = W_0 - \chi$. When $F_1 < 6$ V/nm, the dominant emission process is multi-photon absorption, since the curve scales as $D \propto F_1^{2n}$ from both ESQM and the exact double-barrier quantum model. Here, $n = 3$ for ESQM and $n = 4$ for the exact double-barrier model, which is determined by the ratio of the barrier height W_{eff} to the photon energy ($\hbar\omega = 1.55$ eV for 800 nm laser) in each model, with $W_{eff} = W_0 - \chi = 4.1$ eV for ESQM and $W_{eff} = W_0 = 5.1$ eV for the exact double-barrier model. The smaller effective potential barrier used in ESQM also explains the greater transmission probability by ESQM. The regime of multiphoton absorption is further confirmed by the Keldysh parameter, $\gamma = 4.75$ (Exact) and $\gamma = 5.68$ (ESQM) for $F_1 = 6\,\mathrm{V/nm}$. The abrupt slope change at $F_1 \approx 12\,\mathrm{V/nm}$ from the exact model is due to the channel closing effect [38], [119] (see Fig. 5.11). The underestimation of $D(\varepsilon = E_F)$ from FN equation is expected, because FN equation takes account of optical field tunneling only, which is significantly smaller than other *n*-photon

processes in the multiphoton absorption regime. For $13 < F_1 < 15\ \mathrm{V/nm}$, the curve for FN equation overlaps with that for the exact model, as the emission enters the optical field tunneling regime.

Figure 5.15(b) shows emission current density as a function of the laser field strength F_1, showing similar trends as the emission probability in Fig. 5.15(a). The curves from the three models converge as the laser field increases to 15 V/nm, when the strong optical field tunneling becomes dominant.

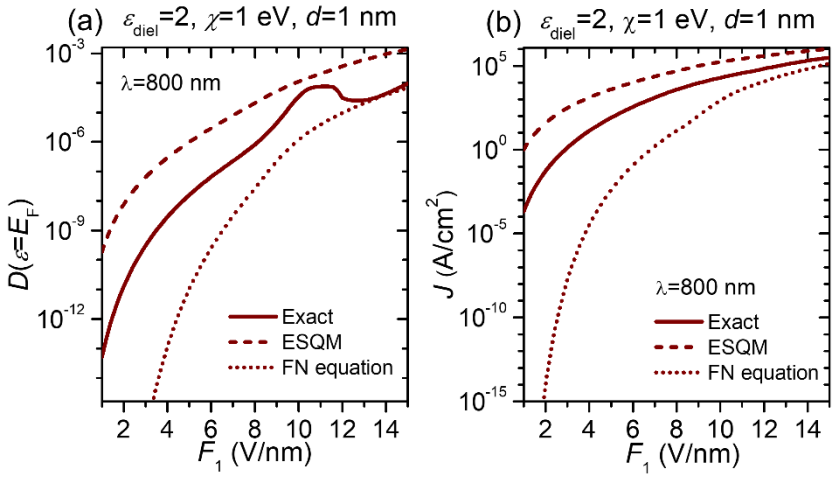

Figure 5.15 Comparison of the exact quantum model with the effective single-barrier quantum model (ESQM) and modified Fowler-Nordheim (FN) equation for photoemission from 1D flat dielectric-coated metal surfaces. (a) Transmission probability $D(\varepsilon = E_F)$, and (b) emission current density J, as a function of the laser field strength F_1 in the vacuum. Here, we use $\varepsilon_{diel} = 2$, $\chi = 1$ eV, and d = 1nm. The dc electric field $F_0 = 0$.

5.4.3 Comparison Results for Pyramidal Cathodes

It has been demonstrated that a pyramid-shaped plasmonic resonant photoemitter coated with an atomically thick dielectric can produce an emission current of orders of magnitude larger than a bare photoemitter [47]. Although ESQM was used to estimate the photoemission current and has been verified by comparing it with modified FN equation in Ref.[47], it is desirable to calculate photoemission from the exact analytical model. Figure 5.16 presents emission current density J, calculated from the exact double-barrier quantum model, ESQM, and modified FN equation for photoemission from the pyramid-shaped gold emitter with SiO_2 coating, as a function of the externally applied laser field strength F_{ext}. Full wave optical simulation shows an approximately linearly decaying laser field inside the dielectric at the resonance wavelength of 608 nm, with the maximum field enhancement factor β at the metal-dielectric interface ($x = 0$ in

Fig. 5.4). To accommodate to the double-triangular barrier quantum model and the modified FN equation, the laser field inside the coating is assumed uniform, with the field strength being the one at the metal-dielectric interface, and the laser field in the vacuum is assumed to be that at the dielectric-vacuum interface, i.e., $F_1^{diel} = \beta(x = 0)F_{ext}$, and $F_1 = \beta(x = d)F_{ext}$. Those three models manifest quantitatively good agreement for $F_{ext} > 0.05\,\mathrm{V/nm}$, where the emission enters strong field tunneling regime [47]. This transition is also indicated from the value of Keldysh parameter approaching unity, $\gamma = 1.89$ (Exact) and $\gamma = 2.46$ (ESQM) for $F_{ext} = 0.05\,\mathrm{V/nm}$. For $0.01 < F_{ext} < 0.05\,\mathrm{V/nm}$, emission current densities calculated from both ESQM and FN equation are smaller than that from the exact double-barrier model.

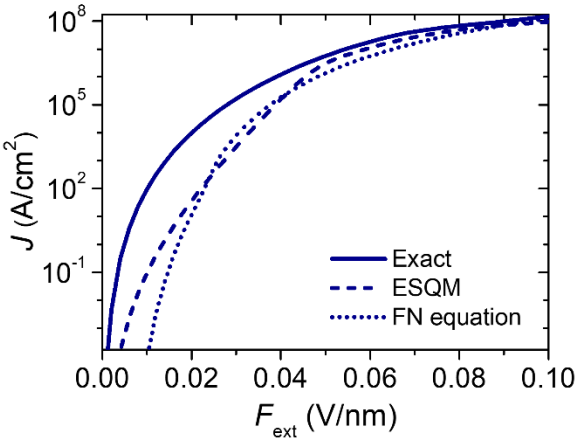

Figure 5.16 Photoemission current density J, calculated from the exact double barrier quantum model (Exact), effective single-barrier quantum model (ESQM), and modified Fowler-Nordheim equation (FN equation), as a function of the externally applied laser field strength F_{ext} for a pyramid-shaped plasmonic resonant photoemitter with SiO_2 coating [47]. Here, the coating thickness d = 1nm, coating electron affinity $\chi = 0.9$ eV, coating relative permittivity $\varepsilon_{diel} = 2.25$, field resonance wavelength is at 608 nm, field enhancement factor at metal-dielectric interface $\beta(x = 0) = 200$, and field enhancement factor at dielectric-vacuum interface $\beta(x = d) = 44$ [47]. The dc electric field $F_0 = 0$.

One may expect that the assumption of the uniform laser field inside the coating being the maximum field at metal-dielectric interface would result in an overestimate of the emission current in the small field regime. However, calculation from the exact double-barrier model with F_1^{diel} determined by the slope of the line connecting the peaks of the potential barrier at two interfaces (see Fig. 5.17), shows that emission current densities from ESQM and FN equation are still smaller for $F_{ext} < 0.03\,\mathrm{V/nm}$, despite the fact that such an approximation of F_1^{diel} would overestimate the potential barrier, thus underestimating photoemission from the exact model. Therefore, applying ESQM to a dielectric-coated plasmonic resonant Au photoemitter [47] may

underestimate the photoemission current for $F_{ext} < 0.03\ \mathrm{V/nm}$, and the exact double-triangular barrier model may be used to give a more accurate estimation of photoemission from coated photoemitters.

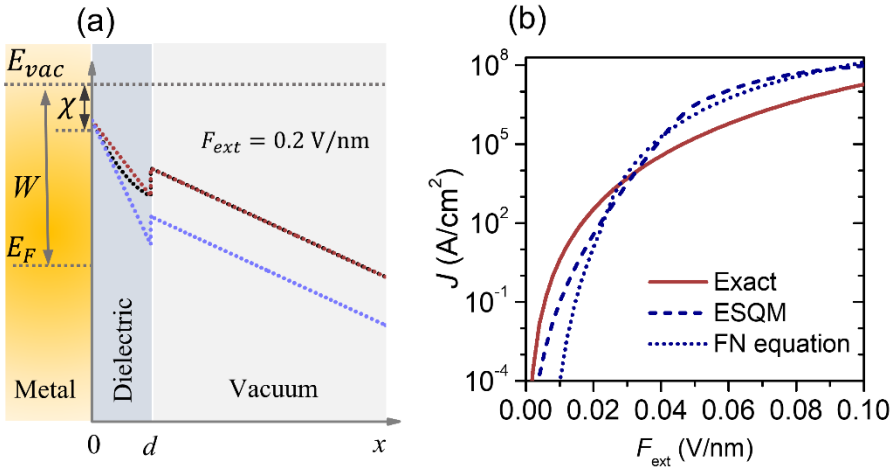

Figure 5.17 (a) Potential barrier profiles. Black dotted line: original potential profile with laser field profile obtained from full wave optical simulation [47]; red dotted line: approximated potential profile with the uniform laser field in the dielectric determined by the slope of the line; blue dotted line: approximated potential profile with the uniform laser field in the dielectric of the field at the metal-dielectric interface. The blue dotted line is used in the FN equation (Fig. 5.16 and 5.17(b)) and exact quantum model (Fig. 5.16). (b) Photoemission current density J, calculated from the exact double-barrier quantum model, effective single-barrier quantum model (ESQM), and modified Fowler-Nordheim equation (FN equation), as a function of the externally applied laser field strength F_{ext} for a pyramid-shaped photoemitter with SiO_2 coating. The calculation in the exact model uses the approximate potential profile shown as the red dotted line in (a). The modified FN equation uses the approximate potential profile shown as the blue dotted line in (a).

5.5 Concluding Remarks

In this chapter, we use our effective single-barrier quantum model (ESQM) to demonstrate that a 1 nm thick layer of SiO_2 around a Au-nanopyramid will enhance the resonant photoemission current density by ~2 orders of magnitude, where the transition from multiphoton absorption to optical field tunneling is accessed at an incident laser intensity at least 10 times lower than that of the bare nanoemitter. The great enhancement is due to the combined effects of the significantly localized enhanced plasmon resonant fields and the reduced potential barrier induced by the coating.

We also construct an analytical model for photoemission from metal surfaces coated with a nanoscale dielectric, by exactly solving the one-dimensional (1D) time-dependent Schrödinger

equation subject to a double-triangular barrier. The model manifests various electron emission mechanisms, i.e., multiphoton photoemission, static field tunneling, photon-assisted field emission, optical field tunneling, and thermionic emission, depending on the applied fields (laser field and dc field) and temperature. The effects of dielectric properties on photoemission are investigated. It is found that a flat metal surface coated with a dielectric of smaller relative permittivity and larger electron affinity can photoemit a current density larger than the uncoated metal due to the lowered surface barrier. For dielectric coated nanoemitters, photoemission can be greatly enhanced due to the nonlinear field enhancements near the coating.

Our model is compared with the effective single-barrier quantum model and the modified Fowler-Nordheim equation, for both flat cathodes and three-dimensional (3D) nanoemitters. It is found that both the effective single-barrier quantum model and the modified Fower-Nordheim equation may underestimate photoemission from the dielectric-coated nanoemitters in the multiphoton absorption regime, and that our exact model may give a more accurate estimation. In the strong-field optical tunneling regime, the three models show quantitatively good agreement. The results further confirm that plasmonic resonant tip photoemitters with nanoscale dielectric coatings may be promising for higher yield electron sources [47].

CHAPTER 6 TWO-COLOR COHERENT CONTROL OF PHOTOEMISSION FROM METAL SURFACES

This chapter is based on the published journal paper "Unraveling quantum pathways interference in two-color coherent control of photoemission with bias voltages," *Phys. Rev. B*, vol. 106, no. 8, p. 085402, Aug. 2022, doi: 10.1103/PhysRevB.106.085402, by **Yang Zhou** and Peng Zhang.

6.1 Introduction

Coherent control of quantum systems relies on the manipulation of quantum interference phenomena via external fields such as laser pulses. Two-color laser field consisting of a strong fundamental laser and a weak second harmonic has become an essential tool to probe and steer quantum pathways interference in the interaction with matter. Recently, two-color coherent control of photoemission from nanotips has drawn great interest, for its flexibility in manipulating electron dynamics in ultrashort temporal scale and nanometer spatial scale [84], [92], [204]–[207], which makes it applicable in spatiotemporal characterization of surface plasmon polaritons [89], [208], [209], investigation of hot-carrier dynamics [205] and strong-field photoemission [88], [210], and control of interference fringes in the momentum distribution of electron emission [90], [211]. It also opens up new opportunities in flexible control of photoemission in applications such as time-resolved electron microscopy [4], [15], [17], [19], free-electron lasers [45], [212], carrier-envelope phase detection [24], [25], [30], and emerging nanophotonic and nanoelectronic devices [26], [28], [32], [47], [207], [213].

By tuning the intensity mixture ratio and relative phase difference between the fundamental laser and its second harmonic, the photoemission current can be modulated with a contrast of up to 97.5% [84], [85], [87], [91], [92], [214]. The strong modulation of photoemission current by two-color laser is ascribed to the quantum interference between competing pathways. The excitation of two-color laser opens out multicolor quantum pathways where photons of different colors are simultaneously absorbed. Depending on the two-color intensity mixture ratio, simple two-pathway or three-pathway quantum interference model has been used to explain the scaling of the coherent signal to the second harmonic intensity in experiments [84]–[87]. However, to give satisfactory fitting to the experimental results, the simple quantum pathway model has to be modified to allow independent weights for the three channels and to account for the discrepancy in the extracted prefactors from those of independent pulses [86]. As another key tuning knob,

increasing dc bias field enhances electron emission but meanwhile suppresses the current modulation, as experimentally observed in [85], [86]. Nevertheless, how the dc bias field influences the weight of each pathway and interference between them is still ambiguous. Analyzing the quantum pathway model using exact quantum theory is therefore of highest interest for photoemission from metals in two-color fields and for coherent control schemes in general [86].

In this chapter, we analyze the quantum pathways interference with the exact analytical solutions of the TDSE including dc bias [91], [92]. These exact analytical quantum models for two-color laser induced photoemission show quantitative good agreement with experimental results [91], [92] and demonstrate the potential in measurement of time-resolved photoelectron energy spectra [92], [93]. The analysis explicitly shows the effects of laser fields and dc bias field on the weights of each pathway and the interference effects among them.

6.2 Analytical Quantum Models for Two-color Laser Induced Photoemission from Metal Surfaces

The 1D model is illustrated in Fig. 6.1(a). Electrons with initial energy of ε emit through the metal-vacuum interface ($x = 0$) due to dc field F_0 and two-color laser field $f(t) = F_1 \cos \omega t + F_2 \cos(2\omega t + \theta)$, where F_1 and F_2 are the magnitudes of the fundamental and second harmonic electric fields, respectively, ω is the angular frequency of the fundamental laser, $\theta = 2\omega\tau$ is the relative phase between the fundamental and second harmonic, with τ the corresponding time delay. For simplicity, the fields are assumed to be perpendicular to the metal surface and abruptly cut off inside the metal [25], [38], [91], [92]. The potential barrier seen by electrons inside the metal reads

$$\phi(x,t) = \begin{cases} 0, & x < 0 \\ V_0 - ef(t)x - eF_0x, & x \geq 0 \end{cases}, \tag{6.1}$$

where $V_0 = E_F + W_{eff}$, E_F is the Fermi energy of the metal, and $W_{eff} = W_0 - W_{Schottky}$ is the effective work function with W_0 the nominal work function and $W_{Schottky} = 2\sqrt{e^3F_0/16\pi\varepsilon_0}$ the Schottky barrier lowering due to dc field F_0, e (> 0) is the elementary charge, and ε_0 is the vacuum permittivity. By exactly solving the TDSE subject to the potential barrier in Eq. (6.1), the time-averaged electron transmission probability from energy level ε is obtained as (more details of the derivation, see references [91], [92])

$$D(\varepsilon) = \sum_{l=-\infty}^{\infty} w_l(\varepsilon) \tag{6.2}$$

where $w_l(\varepsilon)$ represents the electron emission through l-photon processes, with $l < 0$ being multiphoton emission, $l = 0$ direct tunneling, and $l > 0$ multiphoton absorption processes [38], [91]–[93], [125]. The detailed expressions for w_l can be found in Ref. [91] for $F_0 = 0$ and in Ref. [92] for $F_0 \neq 0$. It is important to note that although l in Eq. (6.2), as written, is referred to the number of fundamental photons $\hbar\omega$, it also includes the possible processes of substituting two fundamental photons $2\hbar\omega$ with a single second-harmonic photon $\hbar(2\omega)$, illustrated in the three possible pathways in Fig. 6.1(a), as well as arbitrary multiples of such substitutions.

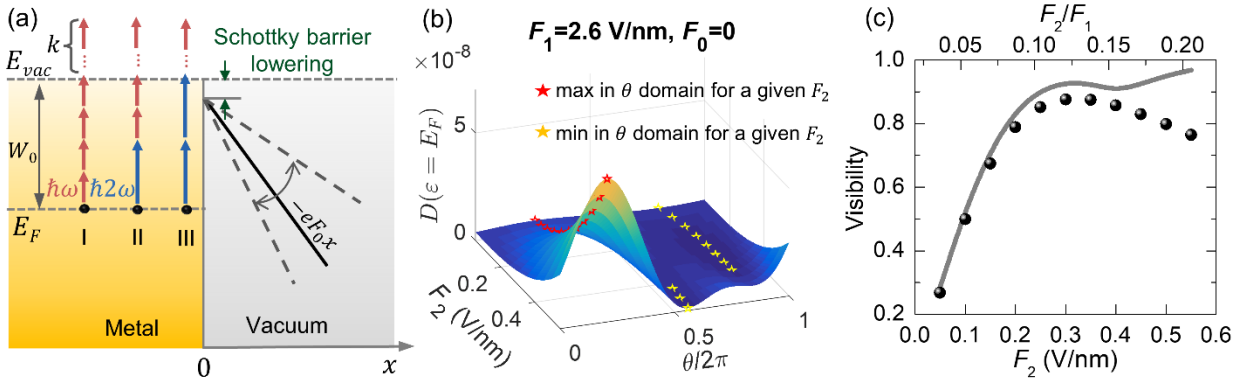

Figure 6.1 (a) Energy diagram for photoemission from metal surfaces induced by two-color laser fields $f(t) = F_1\cos(\omega t) + F_2\cos(2\omega t + \theta)$ under a dc field F_0. Red and blue arrows depict quantum pathway model, with pathway I: absorption of (4+k) fundamental photons (red arrow); pathway II: absorption of (2+k) fundamental photons and 1 second-harmonic photon (blue arrow); pathway III: absorption of 2 second-harmonic photons and k fundamental photons. (b) Electron transmission probability from initial energy $\varepsilon = E_F$, $D(\varepsilon = E_F)$, as a function of 2ω laser field F_2 and phase delay θ, with $F_1 = 2.6\,\mathrm{V/nm}$ and $F_0 = 0$. Red and yellow pentagrams depict maxima and minima in θ domain for a given F_2, respectively. (c) Solid gray curve is calculated from our quantum model in Eq. (6.2), and black scatters are for visibility $= D_{I\&II}/(D_I + D_{II})$, by fitting results with D_is obtained from Eq. (6.4).

Figure 6.1(b) shows the electron emission probability from Fermi level $D(\varepsilon = E_F)$ as a function of second harmonic laser field F_2 and relative phase θ, with fundamental laser field $F_1 = 2.6\,\mathrm{V/nm}$ and dc field $F_0 = 0$. The metal is assumed as gold, with $W_0 = 5.1$ eV and $E_F = 5.53$ eV. The fundamental laser has a wavelength of 800 nm (photon energy of 1.55 eV). For a given F_2, $D(\varepsilon = E_F)$ is a periodic function of relative phase θ with an angular frequency of 2ω. Maxima of $D(\varepsilon = E_F)$ for a given F_2 are observed at $\theta \cong \pi/2$ (shown as red pentagrams in Fig. 6.1(b)), whereas the minima are at $\theta \cong 3\pi/2$ when $F_2 \leq 0.4\,\mathrm{V/nm}$ and at $\theta \approx \pi$ when $F_2 >$

0.4 V/nm (shown as yellow pentagrams in Fig. 6.1(b)). Visibility or the modulation depth due to relative phase θ, which is defined as the ratio of the difference between the maximum and the minimum of transmission probability in θ domain to the summation of them, increases as F_2 increases for $F_2 \leq 0.3$ V/nm and keeps almost constant for $F_2 > 0.3$ V/nm (Fig. 6.1 (c)).

6.3 Quantum Pathways Interference Model

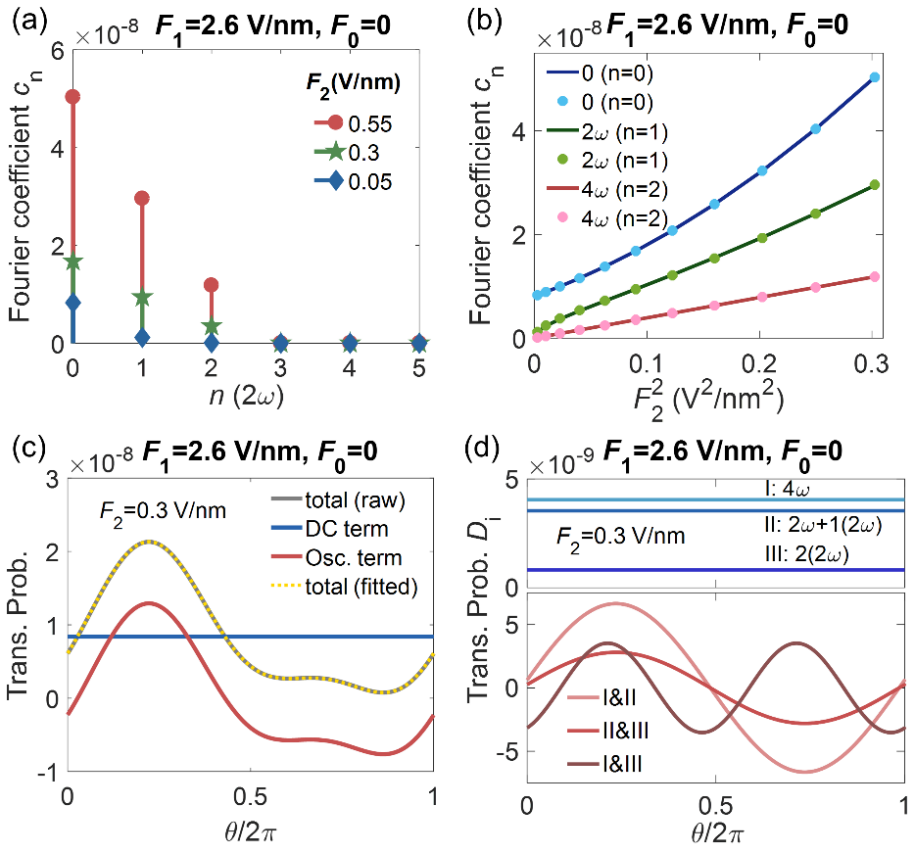

Figure 6.2 (a) Coefficients of Fourier series expansion for $D(\tau)$ for $F_2 = 0.05$, 0.3, and 0.55 V/nm. (b) Fourier series coefficients at angular frequencies of 0 (n=0), 2ω (n=1), and 4ω (n=2) as a function of F_2^2. Scatters represent coefficients from Fourier series expansion of $D(\tau)$ from the exact quantum model, and solid curves are fitted from the quantum pathway model. (c) Decomposed electron transmission probability, with blue curves 0 frequency terms and red curves the oscillatory terms (2ω and 4ω terms). (d) Electron transmission D_i through each quantum pathway (top) and their interference terms (bottom).

Figure 6.2(a) shows the Fourier series coefficient c_n of $D(\varepsilon = E_F)$ vs τ at multiples of second-harmonic laser frequency 2ω, obtained from,

$$D(\tau) = \frac{c_0}{2} + \sum_{n=1}^{N} c_n \sin(n(2\omega)\tau + \varphi_n) \tag{6.3}$$

with $c_0 = \frac{2}{T}\int_0^T D(\tau)d\tau$, $c_n = \sqrt{a_n^2 + b_n^2}$, $a_n = \frac{2}{T}\int_0^T D(\tau)\cos\big(n(2\omega\tau)\big)\,d\tau$, $b_n = \frac{2}{T}\int_0^T D(\tau)\sin(n(2\omega)\tau)\,d\tau$, $T = \frac{2\pi}{2\omega}$, and $\varphi_n = \tan^{-1}\left(\frac{a_n}{b_n}\right)$. Three dominant components at angular frequencies of 0, 2ω, and 4ω are observed for $F_2 = 0.05$, 0.3, and 0.55 V/nm. As F_2 increases, c_1 and c_2 increase and their relative differences to c_0 become smaller, indicating more contribution from high frequency components.

These Fourier coefficients are shown as a function of F_2^2 as scatters in Fig. 6.2(b). The results are fitted with the quantum interference model [84]–[87], which considers pathways I, II, and III as illustrated in Fig. 6.1(a), with the red and blue arrows representing absorption of one fundamental photon and one second-harmonic photon, respectively. The transmission probabilities of each pathway and of the interference terms between them are,

$$D_I \propto \alpha^k (F_1^2)^k (\alpha^4 (F_1^2)^4) = K_I, \tag{6.4a}$$

$$D_{II} \propto \alpha^k (F_1^2)^k (\zeta^2 (F_1^2)^2 F_2^2) = K_{II} F_2^2, \tag{6.4b}$$

$$D_{III} \propto \alpha^k (F_1^2)^k (\beta^2 (F_2^2)^2) = K_{III} (F_2^2)^2, \tag{6.4c}$$

$$D_{I\&II} \propto 2\sqrt{D_I D_{II}}\cos\theta \propto \alpha^k (F_1^2)^k \left(2\alpha^2 \zeta (F_1^2)^3 \sqrt{F_2^2}\cos\theta\right) = K_{I\&II}\sqrt{F_2^2}\cos(2\omega\tau), \tag{6.4d}$$

$$D_{I\&III} \propto 2\sqrt{D_I D_{III}}\cos 2\theta \propto \alpha^k (F_1^2)^k (2\alpha^2 (F_1^2)^2 \beta F_2^2 \cos 2\theta) = K_{I\&III} F_2^2 \cos(4\omega\tau), \tag{6.4e}$$

$$D_{II\&III} \propto 2\sqrt{D_{II} D_{III}}\cos\theta \propto \alpha^k (F_1^2)^k \left(2\zeta F_1^2 \beta \sqrt{(F_2^2)^3}\cos\theta\right) = K_{II\&III}\sqrt{(F_2^2)^3}\cos(2\omega\tau), \tag{6.4f}$$

where α, ζ, and β are the weights for pathways I, II, and III, respectively, and K_i is the prefactor for each term as a power function of F_2^2.

The prefactors K_i in Eq. (6.4), are shown as a function of F_1^2 as scatters in Fig. 6.3. They are fitted by power functions of F_1^2, with fitting results shown as solid curves. The fitting power orders for prefactors of K_I, K_{II}, $K_{I\&II}$, $K_{II\&III}$, and $K_{I\&III}$ are 3.84, 2.43, 3.14, 0.9, and 1.53, respectively. These values are close to the corresponding power orders of 4, 2, 3, 1, and 2 with $k = 0$ in Eq. (4), which validates the quantum pathway model and also indicates the dominant absorption of equivalent 4 fundamental photons for $\varepsilon = E_F$. It should be noted that K_{III} is not fitted here, since it is independent of F_1^2 for $k = 0$. Figure 6.3(a) shows that D_{III} decreases slightly as F_1^2 increases.

With $k = 0$, α, ζ, and β can be calculated from K_I, K_{II}, and K_{III} respectively for a given F_1. Those values are used to calculate $K_{I\&II}$, $K_{II\&III}$, and $K_{I\&III}$, which are shown as dashed curves in

Fig. 6.3(c). Good agreement is achieved between the dashed curves and the scatters obtained from Eq. (6.4), which further confirms the validity of the quantum pathway model.

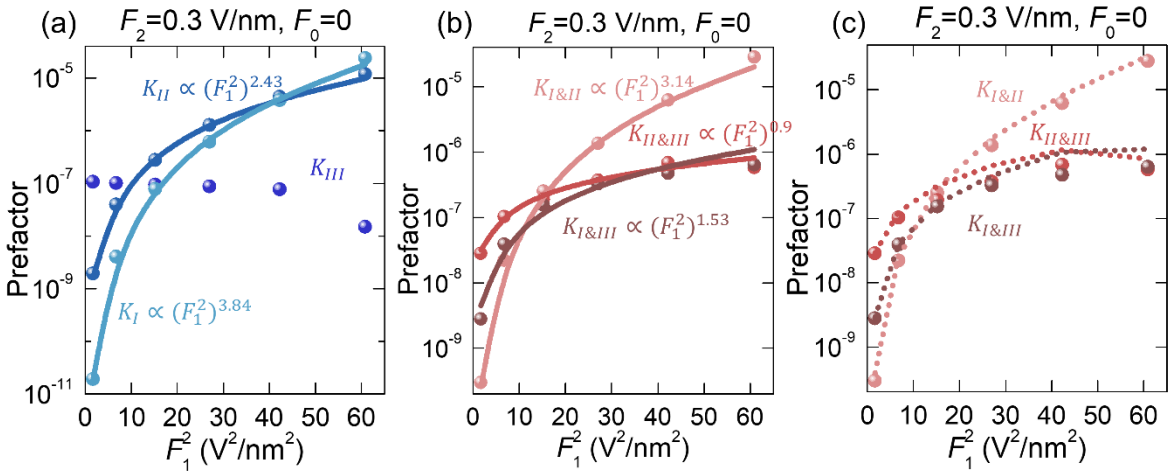

Figure 6.3 Prefactors in Eq. (6.4), (a) K_I, K_{II}, K_{III}, (b) and (c) $K_{I\&II}$, $K_{I\&III}$, and $K_{II\&III}$ as a function of F_1^2. Scatters: values from the fitting of Fourier series coefficients using the quantum interference model; solid curves in (a) and (b): power fitting with respect to F_1^2; dashed curves in (c): values calculated with α, ζ, and β from K_I, K_{II}, and K_{III}.

Equating the total transmission probability $D(\tau)$ in Eq. (6.3) with the sum of all the probabilities in Eqs. (6.4a)-(6.4f) enables us to extract straightforwardly the weights α, ζ, and β from the Fourier coefficients. Here, by setting $k = 0$ (see Fig. 6.3), the fitted K_I, K_{II}, and K_{III} in Fig. 6.2(b) yield $\alpha = 1.18 \times 10^{-3}\mathrm{nm}^2/\mathrm{V}^2$, $\zeta = 2.93 \times 10^{-5}\mathrm{nm}^3/\mathrm{V}^3$, and $\beta = 3.17 \times 10^{-4}\mathrm{nm}^2/\mathrm{V}^2$. With these K_i weights (Fig. 6.2(b)), the transmission probability $D(\varepsilon = E_F)$ is decomposed into a dc term (0 frequency term) and an oscillatory term (consisting of 2ω and 4ω terms), as exemplified in Fig. 6.2(c) for $F_2 = 0.3\,\mathrm{V/nm}$. Fourier series expansion with these fitting parameters perfectly reproduces the raw data from our quantum model obtained from Eq. (6.2).

Photoemission through each of the channels in Eq. (6.4) is explicitly shown in Fig. 6.2(d). It is clear that pathways I and II in combination, form the majority of the constant baseline emission channels, around which the transmission probability oscillates with the relative phase θ. The strongest interference is between pathways I and II. Interference terms, and therefore the total transmission probability, can be strongly tuned by the phase difference θ, with maximum at $\theta \cong \pi/2$ and minimum at $\theta \cong 1.8\pi$, as shown in Figs. 6.2(c) and 6.2(d).

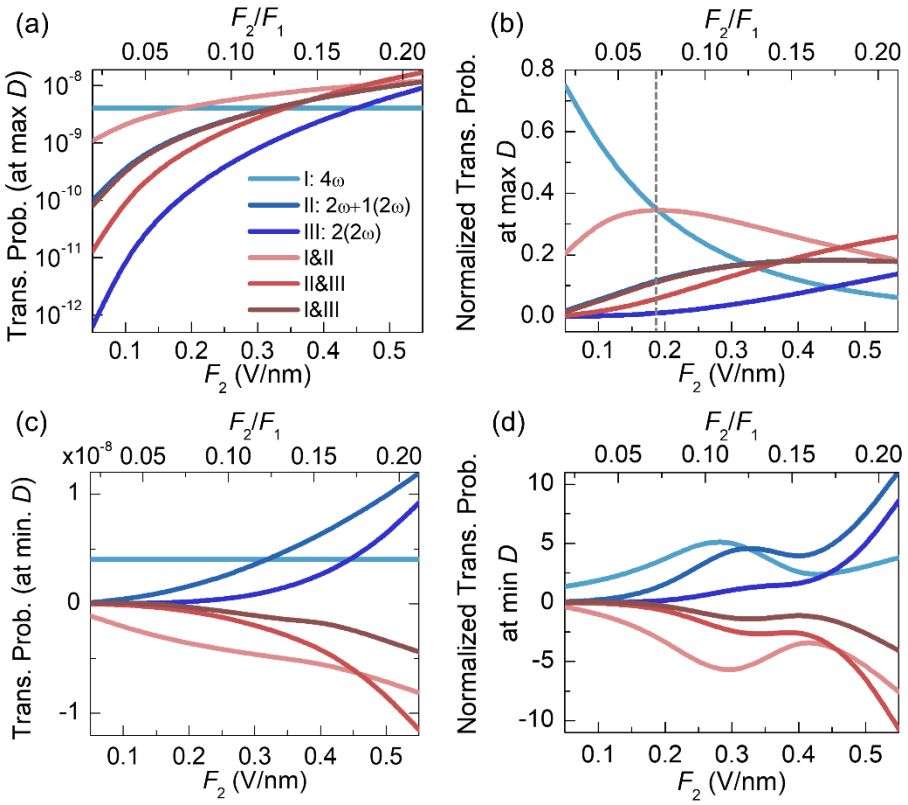

Figure 6.4 (a) Electron transmission probability D_i through each channel and (b) the corresponding normalized transmission probability D_i/D at maximum of $D(\varepsilon = E_F)$ in θ domain for a given F_2. (c) D_i and (d) D_i/D at minimum of $D(\varepsilon = E_F)$ in θ domain for a given F_2. Here, $F_1 = 2.6$ V/nm, and $F_0 = 0$.

The effect of second harmonic laser field F_2 on the contribution of each channel to the total emission is shown in Fig. 6.4. Transmission probability D_i through each channel i at the maximum of total $D(\varepsilon = E_F)$ in θ domain for the given F_2 is plotted in Fig. 6.4(a). The corresponding normalized transmission probability with respect to the total $D(\varepsilon = E_F)$ is shown in Fig. 6.4(b). When $F_2 \lesssim 0.2\,\mathrm{V/nm}$, pathway I and the interference of I&II account for more than 66% of the total emission, whereas contribution from pathway III can be neglected. The negligibility of pathway III for a low field mixture ratio ($F_2/F_1 < 7\%$ here) is further confirmed by the visibility analysis (see Fig. 6.1(c)), which is consistent with previous work for tungsten [84]. As F_2 increases, transmission probability through all channels but pathway I increases, exhibiting strong constructive interferences from I&II, II&III, and I&III. When $F_2 \gtrsim 0.35\,\mathrm{V/nm}$, contributions from channels II, I&III, and II&III exceed that from pathway I. The interference II&III surpasses I&II at $F_2 \cong 0.46\,\mathrm{V/nm}$. Figures 6.4(c) and 6.4(d) shows the transmission probability and their normalized value at minima of $D(\varepsilon = E_F)$ in θ domain as a function of F_2.

The interference terms I&II, II&III, and I&III are negative, which indicate destructive interferences and greatly suppress the total transmission probability. More details of the effect of F_2 is given by analyzing the dependence of $D_i(\varepsilon = E_F)$ vs τ for $F_2 = 0.05$, 0.3, and 0.55 V/nm in Fig. 6.5, which reconfirms the above observation. When F_2 increases to 0.55 V/nm, emission through pathway II and interference II&III become the dominant dc and oscillatory terms respectively.

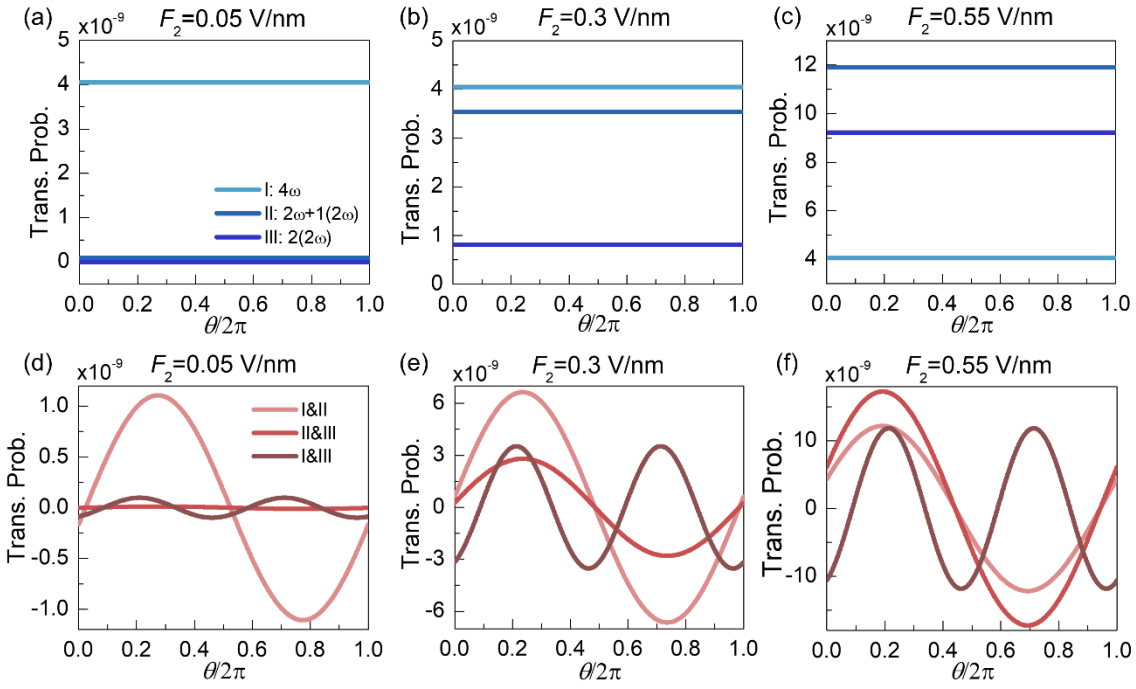

Figure 6.5 Decomposed electron transmission probability by Fourier series expansion. (a), (b), and (c) 0 frequency terms for $F_2 = 0.05$, 0.3 and 0.55 V/nm, respectively. (d), (e), and (f) oscillatory terms (2ω and 4ω terms) for $F_2 = 0.05$, 0.3 and 0.55 V/nm, respectively. F_1 is fixed at 2.6 V/nm.

Figure 6.6 shows the effect of fundamental laser field on the modulation of quantum interference and the contribution of each pathway. As shown in Fig. 6.6(a), when F_1 increases, the visibility increases and then decreases, with the maximum at $F_1 = 2.6$ V/nm, corresponding to the intensity ratio of second harmonic to the fundamental of 1.3%, with fixed second harmonic field $F_2 = 0.3$ V/nm and dc field $F_0 = 0$. The transmission probability from initial energy level $\varepsilon = E_F$ as a function of relative phase θ is shown as inset in Fig. 6.6(a) under various fundamental laser fields F_1. As F_1 increases, $D(\varepsilon = E_F)$ is greatly enhanced. The oscillation magnitude gradually decreases for $F_1 > 2.6$ V/nm, consistent with the decreasing visibility in Fig. 6.6(a).

The decrease of the visibility is ascribed to smaller two-color laser intensity ratio, which results in relatively less contribution from pathways II and III and therefore the interference terms, as shown in Fig. 6.6(b). When $F_1 < 2\ \mathrm{V/nm}$ (or $F_2/F_1 > 0.15$), the dominant emission is through pathway III and the interference term II & III. As F_1 increases, electron emission through pathway I and interference I&II increase greatly. As F_1 reaches $\sim 3.7\ \mathrm{V/nm}$, the contribution from pathway I exceeds that of the interference term I&II. For $F_1 > 3.7\ \mathrm{V/nm}$, while I&II remains the dominant interference term, its contribution to photoemission continues to decrease.

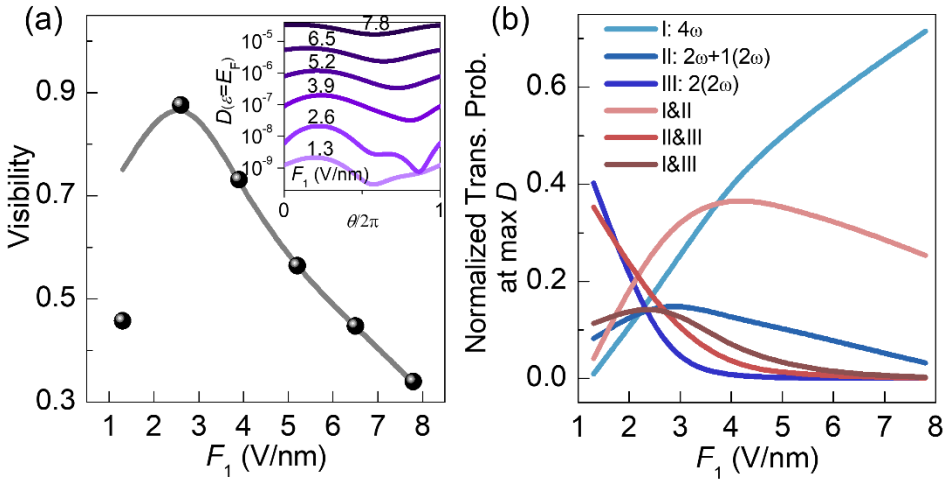

Figure 6.6 (a) Visibility as a function of F_1. Gray solid curve: calculated directly from the data by the quantum model in Eq. (6.2); Black scatters: calculated from visibility $= D_{I\&II}/(D_I + D_{II})$ with D_I, D_{II}, and $D_{I\&II}$ from Eq. (6.4) using fitted parameters; inset: transmission probability as a function of relative phase under different F_1. (b) Normalized transmission probability over the total transmission probability at maximum of $D(\varepsilon = E_F)$ in θ domain as a function of F_1. Here, we fix $F_2 = 0.3\ \mathrm{V/nm}$ and $F_0 = 0$.

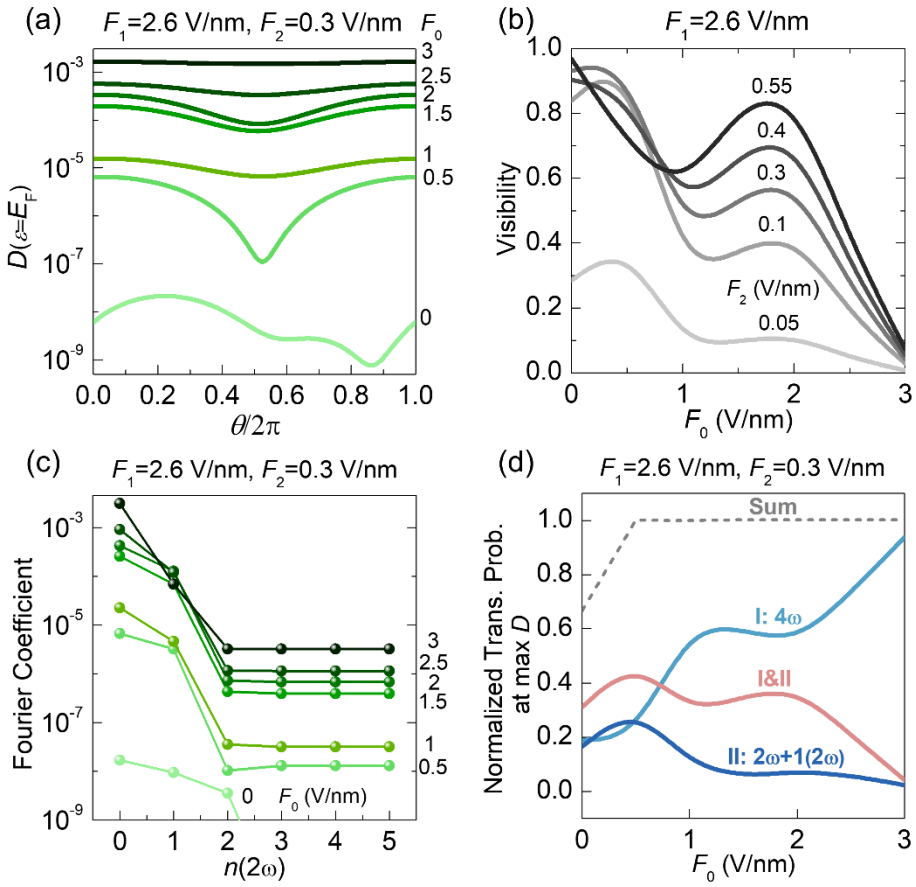

Figure 6.7 (a) $D(\varepsilon = E_F)$ as a function of phase delay θ under various dc fields F_0. (b) Visibility as a function of F_0 under various F_2. (c) Fourier series coefficients under various F_0. (d) Normalized transmission probability over the total transmission probability at maximum of $D(\varepsilon = E_F)$ in θ domain as a function of F_0. Here, we use $F_1 = 2.6$ V/nm and $F_2 = 0.3$ V/nm in (a), (c), and (d).

As another key knob to the coherent control of electron emission by two-color lasers, the effect of dc field is shown in Fig. 6.7. In Fig. 6.7(a), $D(\varepsilon = E_F)$ is plotted as a function of relative phase θ under various dc fields F_0. As F_0 increases, transmission probability is greatly enhanced due to the lowering and narrowing of the surface potential barrier, which opens emission channels of lower order (cf. Fig. 2 in [92]). The minimum shifts from $\theta \cong 1.7\pi$ to $\theta \cong \pi$, which indicates the suppression of high order 4ω terms. Figure 6.7(b) shows the visibility as a function of F_0 under different second harmonic laser fields with $F_1 = 2.6\,\mathrm{V/nm}$. For $F_2 \leq 0.3\,\mathrm{V/nm}$, the maximum visibility is observed at $F_0 \cong 0.5\,\mathrm{V/nm}$, whereas for $F_2 \geq 0.4\,\mathrm{V/nm}$, the maximum occurs at $F_0 = 0$. Another peak also appears at $F_0 \cong 1.75\,\mathrm{V/nm}$ for all cases. When $F_0 > 1.75\,\mathrm{V/nm}$, visibility decreases. As F_0 reaches 3 V/nm, visibility drops to almost 0 for all cases.

The nonlinear dependence of visibility on dc fields can be explained by looking at the Fourier series coefficient, as shown in logarithm scale in Fig. 6.7(c). When $F_0 \geq 0.5\,\mathrm{V/nm}$, the high frequency component at 4ω is suppressed compared to the 0 and 2ω terms. As F_0 further increases, the difference between the coefficient at 0 frequency and that at 2ω increases. When F_0 is sufficiently large, the component at 2ω becomes also negligibly small compared to the 0 frequency component. Thus, the peaks around 0 - 0.5 V/nm and 1.75 V/nm in Fig. 6.7(b) can be attributed to the 4ω and 2ω components, respectively. Note the peaks are also observed in previous experiments (inset in Fig. 5 of [86]). Normalized transmission probability at maximum of $D(\varepsilon = E_F)$ in θ domain in Fig. 6.7(d) also confirms this observation. Since 4ω term is negligible for the majority of the cases, only pathways I, II, and their interference I&II are considered here for simplicity. When $F_0 < 0.5\,\mathrm{V/nm}$, those two pathways and the interference between them cannot account for the total emission, as the sum of those terms is smaller than 1, indicating that additional contributions from 4ω term are needed in this regime. As $F_0 \geq 0.5\,\mathrm{V/nm}$, the sum approaches 1. The contribution from pathway I to the total emission increases, while the contribution from the other two channels decreases. It is important to note that, different from the physical meaning of absorption of 4 photons of fundamental laser in the absence of dc field, pathway I with positive F_0 also includes contributions from direct tunneling, photon-assisted tunneling, and photon emission tunneling (cf. Fig. 2 in [92]), which are all captured by the prefactors with power of k in Eq. (6.4).

6.4 Concluding Remarks

In this chapter, we analyze the quantum pathways interference in two-color coherent control of photoemission using exact analytical solutions of the TDSE including dc bias. The exact theory includes the contribution from all possible quantum pathways and their interference terms. The effects of two-color laser fields and dc bias field on the weights of each pathway and interferences between them are explicitly demonstrated. It is found that increasing the intensity ratio of the second harmonic to fundamental lasers would result in stronger high frequency modulations and increased visibility more than 95%, where contributions from pathways with the replacement of two fundamental photons with one second-harmonic photon and their interferences become significant. The occurrence of maximum (or minimum) transmission with varying phase delays of the two-color lasers is due to the constructive (or destructive) interferences among the pathways. Increasing bias voltages shifts the dominant emission process

from multiphoton absorption to photon-assisted tunneling or direct tunneling, which sequentially decrease the weights of higher order 4ω and then 2ω components, resulting in two peaks in the visibility as a function of bias voltage. This study provides direct theoretical foundation to confirm the coherent emission physics of replacing two fundamental photons with one second-harmonic photon despite various possible pathways.

CHAPTER 7 SUMMARY AND SUGGESTED FUTURE WORKS

7.1 Summary

In this thesis, we develop analytical quantum models for laser-induced photoemission from bare or dielectric-coated metal surfaces, by exactly solving the TDSE. Our models are applicable to arbitrary combination of laser properties (wavelength and field strength), metal properties (Fermi energy and work function), dc field, and dielectric properties (thickness, relative permittivity, and electron affinity). These models include various electron emission processes, i.e., multiphoton absorption photoemission, above-threshold photoemission, photo-assisted field emission, field emission, and optical field emission. The parametric dependence of those processes is discussed in detail. The quantum model for bare metal surfaces is validated by comparing with classical models, i.e., three-step model and Fowler-DuBridge model. The effects of laser wavelength (200-1200 nm) and the accompanying laser heating on the quantum efficiency of photoemission from bare metal surfaces are studied. The effects of dielectric coatings on cathode surfaces are studied. With the quantum model for two-color laser induced photoemission, we analyze the quantum pathways interference in two-color coherent control of photoemission. The effects of laser fields (the intensity mixture ratio of the second harmonic (2ω) to fundamental (ω) and their relative phase) and dc field on the weights of each pathway and the interferences among them are investigated.

Using the model for photoemission from bare metal surfaces, it is found that shorter wavelength lasers can induce more photoemission from electron initial energy levels further below the Fermi level, and therefore yield a larger quantum efficiency (QE). The dc field increases QE, but it is found to have a greater impact on lasers with wavelengths close to the threshold (i.e., the corresponding photon energy is the same as the cathode work function) than on shorter wavelength lasers. By comparison with classical models, the scaling of QE of the quantum model agrees well with the other models for low intensity laser fields, even though they have different settings and assumptions.

Using the model for photoemission from metal surfaces and the two temperature model, it is found that QE can be increased nonlinearly by the non-equilibrium electron heating produced by intense sub-picosecond laser pulses. This increase of QE due to laser heating is the strongest near laser wavelengths where the cathode work function is an integer multiple of the corresponding laser photon energy. The quantum model, with laser heating effects included, reproduces

previous experimental results, which further validates our quantum model and the importance of laser heating.

For 1D flat metallic cathode surfaces with a dielectric coating, it is found the field emission current density can be larger than the uncoated case when the dielectric constant is smaller than a certain value ε_{diel}^{th} and the dielectric thickness is larger than the threshold value $d_{th}[\text{nm}] \approx \varepsilon_{diel} W/eF$ with the dielectric constant $\varepsilon_{diel} < \varepsilon_{diel}^{th}$, where W is the work function of the cathode material, F is the applied dc field, and e is the elementary charge (positive). Comparison of our quantum model with a modified Fowler-Nordheim equation for double-barrier shows qualitatively good agreement.

Similar to field emission, a flat metal surface with dielectric coatings can photoemit a larger current density than the uncoated case when the dielectric has a smaller relative permittivity and a larger electron affinity. Resonant peaks in the photoemission probability and emission current are observed as a function of dielectric thickness or electron affinity, due to the quantum interference of electron waves inside the dielectric. The comparison of our model with the effective single-barrier quantum model and modified Fowler-Nordheim equation, for both 1D flat cathodes and pyramid-shaped nanoemitters, shows quantitatively good agreement in the optical field tunneling regime. Our quantum model may give a more accurate evaluation of photoemission from dielectric-coated emitters in the multiphoton absorption regime.

Under two-color laser field excitation, the visibility of the photoemission current can be tuned to be more than 95% by increasing the intensity ratio of the second harmonic (2ω) to fundamental (ω) lasers, which signifies the coherent emission physics of replacing two ω photons with one 2ω photon. Constructive (or destructive) interferences among the pathways lead to the maximum (or minimum) emission with varying phase delay of the two-color lasers. Increasing bias voltages shifts the dominant emission process from multiphoton absorption to photon-assisted or direct tunneling, where the sequential decrease of the 4ω and 2ω components in current modulation leads to two peaks in the visibility as a function of dc field.

7.2 Suggested Future Works on the Improvement of the Models

In this thesis, laser heating induced electron dynamics is considered by using the two-temperature model (TTM) for 450 fs laser pulses. Due to the large difference between the heat capacity of electrons and phonons, as well as picosecond-scaled electron-phonon scattering, there is a thermal nonequilibrium between electrons and the lattice [58], [135], [136]. For a laser

pulse of a few hundred femtoseconds to a few picoseconds, TTM is used to obtain electron temperature, with electrons in the metal following Fermi-Dirac distribution. As the laser pulse duration further decreases, TTM may fail due to the thermal nonequilibrium in both the electron and lattice systems. The microscopic kinetic theory, such as Boltzmann's equation [62], [63], [151], needs to be used. In this thesis, the time-averaged transmission probability for continuous wave laser excitation is used for the pulsed laser photoemission. It is an excellent approximation for laser pulses of longer than 10 optical cycles [38]. Therefore, it is expected to be applicable for laser pulses of 450 fs for various laser wavelengths, with ~112.5 laser cycles for 1200 nm and ~675 laser cycles for 200 nm. As laser pulses further decrease to tens of femtoseconds or even shorter, a model for few-cycle pulsed laser induced photoemission is needed [25]. The consistent treatment of the dynamic electron energy distribution function and electron emission, induced by a laser pulse of a few to a hundred femtoseconds, will be a subject of future study.

The effective electron mass in all quantum models is assumed to be electron rest mass in all regions, i.e., metal, dielectric, and vacuum. However, effective electron mass varies with materials. Metals usually have an effective electron mass close to the electron rest mass, while in semiconductors and dielectrics, electrons usually have an effective mass (with respect to electron rest mass) in the range of 0.01 to 10 [215], [216]. The external applied fields may also affect the effective electron mass. The tunneling effective mass for the electron in the SiO_2 layer is found to increase slightly with applied dc bias [217]. Theoretical analysis of the effective electron mass of various semiconductors in the presence of light waves reveals that the effective electron mass increases with light intensity and wavelength [218], [219]. Including the effective electron mass in different regions into our quantum models will be another subject of future study.

In the models for electron emission from dielectric-coated metal surfaces, the dielectric is assumed to be ideal, with only electron affinity and relative permittivity considered. Relative permittivity is assumed to be a constant real value all the time. For lossy material, relative permittivity can be a complex number. It is found that relative permittivity depends on the thickness of the material. Experimental and theoretical studies have shown that both real and imaginary parts of the relative permittivity of Si decrease as the thickness decreases to nanoscale (a few to ten nanometers), due to the quantum confinement effect [220], [221]. Both real and imaginary parts of the relative permittivity of Si also show their dependence on the photon energy when the thickness of Si is under a certain threshold [220], [221]. It is worthwhile to take

those factors into account in our quantum models.

In those models for electron emission from metal surfaces with dielectric coatings, the metal, the dielectric, and the interfaces between them are all assumed to be perfectly aligned and with no defects or impurities. However, localized traps may exist in the bulk dielectric and at the metal-dielectric interface, especially when the dielectric layer becomes relatively thick [222], which may result in trapping of photoexcited electrons from metal. Trapped charges, impurities, and defects will modify the surface potential profile. Ionic defects in the dielectric in metal-dielectric-metal structure form quantum wells, resulting in enhanced tunneling current [223]. At higher fields, more electrons are emitted into the dielectric, where the space charge effect cannot be ignored [28], [32], [224]. The potential barrier is considerably modified by these factors. All these call for a numerical solution to higher-dimensional time-dependent Schrödinger equation with a realistic potential profile due to the time- and space-varying local fields, space charge, image charge, trapped charges and impurities and defects in dielectric.

7.3 Suggested Future Works on the Applications of the Models

Quantum models presented in this thesis are one dimensional, with surface potential profile in (oscillatory) triangular shape. The field enhancement due to the emitter geometry, surface roughness and plasmonic effects and corresponding spatial variation are prescribed but not considered consistently in the quantum models. Triangular potential profile is still a good approximation with local field enhancement included for cathodes of various shapes [47], [79], [92]. It will be of great interest to apply quantum models with surface field enhancement included to cathodes of different geometries or nanostructures.

Graphene has unique electronic properties, including high carrier mobility, ballistic transport, and linear energy dispersion relationship, which make it a promising cathode material to produce high-quality electron sources [225]. Classical models for field emission and photoemission [97], [110], [111] may not work for graphene, since they assume that the energy dispersion of the emitter has a parabolic-like function. Equations. (2.9), (4.9), and (5.12) indicate that emission current density is determined by two factors, i.e., transmission probability and supply function. Our quantum models include photoemission, field emission, and thermionic emission with laser heating induced temperature rise included. By utilizing the material-specific supply function, our model is expected to be directly applicable to graphene and other two-dimensional (2D) materials.

The models developed and/or utilized in this thesis can be applied to study density modulation of electron beams during their emission. Such a density modulation scheme based on optical means may open new opportunities to improve the performance of electron beam based electromagnetic sources and amplifiers [172], [226], [227]. Models in this thesis may also be extended to photoemission and transport in a nanogap, where the effects of the nearby anode will become important [123], [124], [207], [228]. The physics of photoemission in nanogaps will find applications to photodetectors [109], electrical contacts and junctions [229]–[232], and ultrafast electron microscopy [233].

High resolution scanning electron microscopy (SEM) or transmission electron microscopy (TEM) requires the electron source to be with a high brightness and a low energy spread [19], [234]. Quantum models for field/photo- emission from dielectric-coated metal surfaces indicate that the quantum well formed on the surface due to the dielectric induces quantum resonance effects. Metal surfaces with dielectric coatings of certain properties (thickness, electron affinity, and relative permittivity) can produce enhanced electron emission with narrow energy peaks on the energy spectrum (see Fig. 4.4), compared to electron emission from bare metals. An ongoing work on photoemission from metal surfaces with a nearby quantum well also observes the aforementioned quantum resonant enhanced emission. Our models on electron emission from dielectric-coated metal surfaces provide insights into designing cathodes to produce highly bright and highly collimated electron sources, which can be useful for applications such as high-resolution electron microscopies, compact particle accelerators, and high-power microwave sources.

BIBLIOGRAPHY

[1] P. Baum and A. H. Zewail, "Attosecond electron pulses for 4D diffraction and microscopy," *Proc. Natl. Acad. Sci. U.S.A.*, vol. 104, no. 47, pp. 18409–18414, Nov. 2007, doi: 10.1073/pnas.0709019104.

[2] O. F. Mohammed, D.-S. Yang, S. K. Pal, and A. H. Zewail, "4D scanning ultrafast electron microscopy: visualization of materials surface dynamics," *J. Am. Chem. Soc.*, vol. 133, no. 20, pp. 7708–7711, May 2011, doi: 10.1021/ja2031322.

[3] S. Hüfner, *Photoelectron Spectroscopy: Principles and Applications*. Springer Science & Business Media, 2013.

[4] E. Najafi, T. D. Scarborough, J. Tang, and A. Zewail, "Four-dimensional imaging of carrier interface dynamics in p-n junctions," *Science*, vol. 347, no. 6218, pp. 164–167, Jan. 2015, doi: 10.1126/science.aaa0217.

[5] G. Herink, F. Kurtz, B. Jalali, D. R. Solli, and C. Ropers, "Real-time spectral interferometry probes the internal dynamics of femtosecond soliton molecules," *Science*, vol. 356, no. 6333, pp. 50–54, Apr. 2017, doi: 10.1126/science.aal5326.

[6] S. Vogelgesang *et al.*, "Phase ordering of charge density waves traced by ultrafast low-energy electron diffraction," *Nature Phys.*, vol. 14, no. 2, Art. no. 2, Feb. 2018, doi: 10.1038/nphys4309.

[7] P. Dombi *et al.*, "Strong-field nano-optics," *Rev. Mod. Phys.*, vol. 92, no. 2, p. 025003, Jun. 2020, doi: 10.1103/RevModPhys.92.025003.

[8] T. Udem, R. Holzwarth, and T. W. Hänsch, "Optical frequency metrology," *Nature*, vol. 416, no. 6877, Art. no. 6877, Mar. 2002, doi: 10.1038/416233a.

[9] C. Gohle *et al.*, "A frequency comb in the extreme ultraviolet," *Nature*, vol. 436, no. 7048, Art. no. 7048, Jul. 2005, doi: 10.1038/nature03851.

[10] L. M. Krüger, S. L. Camenzind, C. R. Phillips, and U. Keller, "Carrier-envelope offset frequency dynamics of a 10-GHz modelocked laser based on cascaded quadratic nonlinearities," *Opt. Express*, vol. 29, no. 22, pp. 36915–36925, Oct. 2021, doi: 10.1364/OE.441393.

[11] M. Krüger, M. Schenk, and P. Hommelhoff, "Attosecond control of electrons emitted from a nanoscale metal tip," *Nature*, vol. 475, no. 7354, Art. no. 7354, Jul. 2011, doi: 10.1038/nature10196.

[12] M. F. Ciappina *et al.*, "Attosecond physics at the nanoscale," *Rep. Prog. Phys.*, vol. 80, no. 5, p. 054401, Mar. 2017, doi: 10.1088/1361-6633/aa574e.

[13] D. J. Park and Y. H. Ahn, "Ultrashort field emission in metallic nanostructures and low-dimensional carbon materials," *Adv. Phys.: X*, vol. 5, no. 1, p. 1726207, Jan. 2020, doi: 10.1080/23746149.2020.1726207.

[14] J. S. Kim *et al.*, "Imaging of transient structures using nanosecond in situ TEM," *Science*, vol. 321, no. 5895, pp. 1472–1475, Sep. 2008, doi: 10.1126/science.1161517.

[15] A. H. Zewail, "Four-dimensional electron microscopy," *Science*, vol. 328, no. 5975, pp. 187–193, Apr. 2010, doi: 10.1126/science.1166135.

[16] A. Feist, K. E. Echternkamp, J. Schauss, S. V. Yalunin, S. Schäfer, and C. Ropers, "Quantum coherent optical phase modulation in an ultrafast transmission electron microscope," *Nature*, vol. 521, no. 7551, Art. no. 7551, May 2015, doi: 10.1038/nature14463.

[17] A. Feist *et al.*, "Ultrafast transmission electron microscopy using a laser-driven field emitter: Femtosecond resolution with a high coherence electron beam," *Ultramicroscopy*, vol. 176, pp. 63–73, May 2017, doi: 10.1016/j.ultramic.2016.12.005.

[18] F. Houdellier, G. M. Caruso, S. Weber, M. Kociak, and A. Arbouet, "Development of a high brightness ultrafast Transmission Electron Microscope based on a laser-driven cold field emission source," *Ultramicroscopy*, vol. 186, pp. 128–138, Mar. 2018, doi: 10.1016/j.ultramic.2017.12.015.

[19] S. Sun *et al.*, "Direct imaging of plasma waves using ultrafast electron microscopy," *Struct. Dyn.*, vol. 7, no. 6, p. 064301, Nov. 2020, doi: 10.1063/4.0000044.

[20] C. A. Brau, "High-brightness electron beams – small free-electron lasers," *Nucl. Instrum. Methods Phys. Res. A: Accel. Spectrom. Detect. Assoc. Equip.*, vol. 407, no. 1, pp. 1–7, Apr. 1998, doi: 10.1016/S0168-9002(97)01356-9.

[21] P. G. O'Shea and H. P. Freund, "Free-electron lasers: status and applications," *Science*, vol. 292, no. 5523, pp. 1853–1858, Jun. 2001, doi: 10.1126/science.1055718.

[22] I. Grguraš *et al.*, "Ultrafast X-ray pulse characterization at free-electron lasers," *Nat. Photonics*, vol. 6, no. 12, Art. no. 12, Dec. 2012, doi: 10.1038/nphoton.2012.276.

[23] P. Baum and A. H. Zewail, "Breaking resolution limits in ultrafast electron diffraction and microscopy," *Proc. Natl. Acad. Sci. U.S.A.*, vol. 103, no. 44, pp. 16105–16110, Oct. 2006, doi: 10.1073/pnas.0607451103.

[24] B. Piglosiewicz *et al.*, "Carrier-envelope phase effects on the strong-field photoemission of electrons from metallic nanostructures," *Nat. Photonics*, vol. 8, no. 1, Art. no. 1, Jan. 2014, doi: 10.1038/nphoton.2013.288.

[25] Y. Luo, Y. Zhou, and P. Zhang, "Few-cycle optical-field-induced photoemission from biased surfaces: An exact quantum theory," *Phys. Rev. B*, vol. 103, no. 8, p. 085410, Feb. 2021, doi: 10.1103/PhysRevB.103.085410.

[26] E. Forati, T. J. Dill, A. R. Tao, and D. Sievenpiper, "Photoemission-based microelectronic devices," *Nat. Commun.*, vol. 7, no. 1, Art. no. 1, Nov. 2016, doi: 10.1038/ncomms13399.

[27] P. Zhang and Y. Y. Lau, "Ultrafast and nanoscale diodes," *J. Plasma Phys.*, vol. 82, no. 5, Oct. 2016, doi: 10.1017/S002237781600091X.

[28] P. Zhang, Á. Valfells, L. K. Ang, J. W. Luginsland, and Y. Y. Lau, "100 years of the physics of diodes," *Appl. Phys. Rev.*, vol. 4, no. 1, p. 011304, Mar. 2017, doi: 10.1063/1.4978231.

[29] C. Karnetzky *et al.*, "Towards femtosecond on-chip electronics based on plasmonic hot electron nano-emitters," *Nat. Commun.*, vol. 9, no. 1, Art. no. 1, Jun. 2018, doi: 10.1038/s41467-018-04666-y.

[30] Y. Yang *et al.*, "Light phase detection with on-chip petahertz electronic networks," *Nat.*

Commun., vol. 11, no. 1, Art. no. 1, Jul. 2020, doi: 10.1038/s41467-020-17250-0.

[31] F. Rezaeifar, H. U. Chae, R. Ahsan, and R. Kapadia, "Hot electron emission from waveguide integrated lanthanum hexaboride nanoparticles," *Appl. Phys. Lett.*, vol. 118, no. 7, p. 071108, Feb. 2021, doi: 10.1063/5.0029877.

[32] P. Zhang, Y. S. Ang, A. L. Garner, Á. Valfells, J. W. Luginsland, and L. K. Ang, "Space–charge limited current in nanodiodes: Ballistic, collisional, and dynamical effects," *J. Appl. Phys.*, vol. 129, no. 10, p. 100902, Mar. 2021, doi: 10.1063/5.0042355.

[33] M. Schenk, M. Krüger, and P. Hommelhoff, "Strong-field above-threshold photoemission from sharp metal tips," *Phys. Rev. Lett.*, vol. 105, no. 25, p. 257601, Dec. 2010, doi: 10.1103/PhysRevLett.105.257601.

[34] P. Musumeci *et al.*, "Multiphoton photoemission from a copper cathode illuminated by ultrashort laser pulses in an rf photoinjector," *Phys. Rev. Lett.*, vol. 104, no. 8, p. 084801, Feb. 2010, doi: 10.1103/PhysRevLett.104.084801.

[35] M. R. Bionta *et al.*, "Laser-induced electron emission from a tungsten nanotip: identifying above threshold photoemission using energy-resolved laser power dependencies," *J. Mod. Opt.*, vol. 61, no. 10, pp. 833–838, Jun. 2014, doi: 10.1080/09500340.2013.846432.

[36] P. Dombi *et al.*, "Ultrafast strong-field photoemission from plasmonic nanoparticles," *Nano Lett.*, vol. 13, no. 2, pp. 674–678, Feb. 2013, doi: 10.1021/nl304365e.

[37] F. Kusa, K. E. Echternkamp, G. Herink, C. Ropers, and S. Ashihara, "Optical field emission from resonant gold nanorods driven by femtosecond mid-infrared pulses," *AIP Adv.*, vol. 5, no. 7, p. 077138, Jul. 2015, doi: 10.1063/1.4927151.

[38] P. Zhang and Y. Y. Lau, "Ultrafast strong-field photoelectron emission from biased metal surfaces: exact solution to time-dependent Schrödinger Equation," *Sci. Rep.*, vol. 6, no. 1, p. 19894, Apr. 2016, doi: 10.1038/srep19894.

[39] S. Zhou *et al.*, "Ultrafast field-emission electron sources based on nanomaterials," *Adv. Mater.*, vol. 31, no. 45, p. 1805845, 2019, doi: 10.1002/adma.201805845.

[40] A. Apolonski *et al.*, "Observation of light-phase-sensitive photoemission from a metal," *Phys. Rev. Lett.*, vol. 92, no. 7, p. 073902, Feb. 2004, doi: 10.1103/PhysRevLett.92.073902.

[41] N. A. Papadogiannis, S. D. Moustaïzis, and J. P. Girardeau-Montaut, "Electron relaxation phenomena on a copper surface via nonlinear ultrashort single-photon photoelectric emission," *J. Phys. D: Appl. Phys.*, vol. 30, no. 17, pp. 2389–2396, Sep. 1997, doi: 10.1088/0022-3727/30/17/004.

[42] N. A. Papadogiannis and S. D. Moustaizis, "Ultrashort laser-induced electron photoemission: a method to characterize metallic photocathodes," *J. Phys. D: Appl. Phys.*, vol. 34, no. 4, pp. 499–505, Feb. 2001, doi: 10.1088/0022-3727/34/4/310.

[43] D. H. Dowell, F. K. King, R. E. Kirby, J. F. Schmerge, and J. M. Smedley, "In situ cleaning of metal cathodes using a hydrogen ion beam," *Phys. Rev. ST Accel. Beams*, vol. 9, no. 6, p. 063502, Jun. 2006, doi: 10.1103/PhysRevSTAB.9.063502.

[44] D. H. Dowell and J. F. Schmerge, "Quantum efficiency and thermal emittance of metal

photocathodes," *Phys. Rev. ST Accel. Beams*, vol. 12, no. 7, p. 074201, Jul. 2009, doi: 10.1103/PhysRevSTAB.12.074201.

[45] P. Hommelhoff, Y. Sortais, A. Aghajani-Talesh, and M. A. Kasevich, "Field emission tip as a nanometer source of free electron femtosecond pulses," *Phys. Rev. Lett.*, vol. 96, no. 7, p. 077401, Feb. 2006, doi: 10.1103/PhysRevLett.96.077401.

[46] M. Sivis, N. Pazos-Perez, R. Yu, R. Alvarez-Puebla, F. J. García de Abajo, and C. Ropers, "Continuous-wave multiphoton photoemission from plasmonic nanostars," *Commun. Phys.*, vol. 1, no. 1, Art. no. 1, Apr. 2018, doi: 10.1038/s42005-018-0014-7.

[47] X. Xiong *et al.*, "Plasmon-enhanced resonant photoemission using atomically thick dielectric coatings," *ACS Nano*, vol. 14, no. 7, pp. 8806–8815, Jul. 2020, doi: 10.1021/acsnano.0c03406.

[48] D. J. Park, B. Piglosiewicz, S. Schmidt, H. Kollmann, M. Mascheck, and C. Lienau, "Strong field acceleration and steering of ultrafast electron pulses from a sharp metallic nanotip," *Phys. Rev. Lett.*, vol. 109, no. 24, p. 244803, Dec. 2012, doi: 10.1103/PhysRevLett.109.244803.

[49] G. Herink, D. R. Solli, M. Gulde, and C. Ropers, "Field-driven photoemission from nanostructures quenches the quiver motion," *Nature*, vol. 483, no. 7388, Art. no. 7388, Mar. 2012, doi: 10.1038/nature10878.

[50] L. Wimmer, G. Herink, D. R. Solli, S. V. Yalunin, K. E. Echternkamp, and C. Ropers, "Terahertz control of nanotip photoemission," *Nat. Phys.*, vol. 10, no. 6, pp. 432–436, Jun. 2014, doi: 10.1038/nphys2974.

[51] G. Herink, L. Wimmer, and C. Ropers, "Field emission at terahertz frequencies: AC-tunneling and ultrafast carrier dynamics," *New J. Phys.*, vol. 16, no. 12, p. 123005, Dec. 2014, doi: 10.1088/1367-2630/16/12/123005.

[52] S. L. Lange, N. K. Noori, T. M. B. Kristensen, K. Steenberg, and P. U. Jepsen, "Ultrafast THz-driven electron emission from metal metasurfaces," *J. Appl. Phys.*, vol. 128, no. 7, p. 070901, Aug. 2020, doi: 10.1063/1.5142590.

[53] F. Giori, L. A. MacKenzie, and E. J. McKinney, "Laser-induced thermionic emission," *Appl. Phys. Lett.*, vol. 3, no. 2, p. 4, 1963.

[54] E. M. Logothetis and P. L. Hartman, "Laser-induced electron emission from solids: many-photon photoelectric effects and thermionic emission," *Phys. Rev.*, vol. 187, no. 2, pp. 460–474, Nov. 1969, doi: 10.1103/PhysRev.187.460.

[55] K. Yamada, K. Miyajima, and F. Mafuné, "Thermionic emission of electrons from gold nanoparticles by nanosecond pulse-laser excitation of interband," *J. Phys. Chem. C*, vol. 111, no. 30, pp. 11246–11251, Aug. 2007, doi: 10.1021/jp0730747.

[56] T. Wang, J. Guo, J. Shao, D. Wang, A. Chen, and M. Jin, "Ultrafast thermionic emission from metal irradiated using a femtosecond laser and an electric field in combination," *Phys. Plasmas*, vol. 22, no. 3, p. 033106, Mar. 2015, doi: 10.1063/1.4914164.

[57] J. M. Mitrani, M. N. Shneider, B. C. Stratton, and Y. Raitses, "Modeling thermionic emission from laser-heated nanoparticles," *Appl. Phys. Lett.*, vol. 108, no. 5, p. 054101, Feb. 2016, doi: 10.1063/1.4940992.

[58] S. I. Anisimov, “Electron emission from metal surfaces exposed to ultrashort laser pulses,” *Sov. Phys. JETP*, vol. 39, no. 2, pp. 375–377, Aug. 1974.

[59] K. L. Vodopyanov, L. A. Kulevskii, Cs. Tóth, Gy. Farkas, and Z. Gy. Horváth, “Laser induced electron emission from gold surface irradiated by picosecond pulses at λ=2.9 μm,” *Appl. Phys. B*, vol. 48, no. 6, pp. 485–488, Jun. 1989, doi: 10.1007/BF00694684.

[60] W. S. Fann, R. Storz, H. W. K. Tom, and J. Bokor, “Electron thermalization in gold,” *Phys. Rev. B*, vol. 46, no. 20, pp. 13592–13595, Nov. 1992, doi: 10.1103/PhysRevB.46.13592.

[61] K. L. Jensen, N. A. Moody, D. W. Feldman, E. J. Montgomery, and P. G. O’Shea, “Photoemission from metals and cesiated surfaces,” *J. Appl. Phys.*, vol. 102, no. 7, p. 074902, Oct. 2007, doi: 10.1063/1.2786028.

[62] L. Wu and L. K. Ang, “Nonequilibrium model of ultrafast laser-induced electron photofield emission from a dc-biased metallic surface,” *Phys. Rev. B*, vol. 78, no. 22, p. 224112, Dec. 2008, doi: 10.1103/PhysRevB.78.224112.

[63] M. Pant and L. K. Ang, “Time-dependent quantum tunneling and nonequilibrium heating model for the generalized Einstein photoelectric effect,” *Phys. Rev. B*, vol. 88, no. 19, p. 195434, Nov. 2013, doi: 10.1103/PhysRevB.88.195434.

[64] H. Haug and A.-P. Jauho, *Quantum kinetics in transport and optics of semiconductors*. Berlin: Springer, 2008. Accessed: Mar. 06, 2022. [Online]. Available: http://link.springer.com/10.1007/978-3-540-73564-9

[65] D. H. Dowell *et al.*, “Cathode R&D for future light sources,” *Nucl. Instrum. Methods Phys. Res. A: Accel. Spectrom. Detect. Assoc. Equip.*, vol. 622, no. 3, pp. 685–697, Oct. 2010, doi: 10.1016/j.nima.2010.03.104.

[66] P. Musumeci *et al.*, “Advances in bright electron sources,” *Nucl. Instrum. Methods Phys. Res. A: Accel. Spectrom. Detect. Assoc. Equip.*, vol. 907, pp. 209–220, Nov. 2018, doi: 10.1016/j.nima.2018.03.019.

[67] S. A. Maier, *Plasmonics: fundamentals and applications*, vol. 1. Springer, 2007.

[68] D. A. Dimitrov *et al.*, “Modeling quantum yield, emittance, and surface roughness effects from metallic photocathodes,” *J. Appl. Phys.*, vol. 122, no. 16, p. 165303, Oct. 2017, doi: 10.1063/1.4996568.

[69] N. A. Moody *et al.*, “Perspectives on designer photocathodes for X-ray free-electron lasers: influencing emission properties with heterostructures and nanoengineered electronic states,” *Phys. Rev. Applied*, vol. 10, no. 4, p. 047002, Oct. 2018, doi: 10.1103/PhysRevApplied.10.047002.

[70] F. Liu *et al.*, “Single layer graphene protective gas barrier for copper photocathodes,” *Appl. Phys. Lett.*, vol. 110, no. 4, p. 041607, Jan. 2017, doi: 10.1063/1.4974738.

[71] A. Tafel, S. Meier, J. Ristein, and P. Hommelhoff, “Femtosecond laser-induced electron emission from nanodiamond-coated tungsten needle tips,” *Phys. Rev. Lett.*, vol. 123, no. 14, p. 146802, Oct. 2019, doi: 10.1103/PhysRevLett.123.146802.

[72] G. Wang, P. Yang, and E. R. Batista, “Computational screening of two-dimensional coatings for semiconducting photocathodes,” *Phys. Rev. Materials*, vol. 4, no. 2, p. 024001,

Feb. 2020, doi: 10.1103/PhysRevMaterials.4.024001.

[73] H. Ono *et al.*, "Study on a long-life photocathode with an CsBr protective layer for an rf electron gun," *Jpn. J. Appl. Phys.*, vol. 58, no. 6, p. 066005, Jun. 2019, doi: 10.7567/1347-4065/ab170d.

[74] A. Galdi *et al.*, "The effects of oxygen-induced phase segregation on the interfacial electronic structure and quantum efficiency of Cs3Sb photocathodes," *J. Chem. Phys.*, vol. 153, no. 14, p. 144705, Oct. 2020, doi: 10.1063/5.0024020.

[75] Y. Zhou and P. Zhang, "Theory of laser-induced photoemission from a metal surface with nanoscale dielectric coating," *J. Appl. Phys.*, vol. 131, no. 6, p. 064903, Feb. 2022, doi: 10.1063/5.0078060.

[76] U. Martinez, L. Giordano, and G. Pacchioni, "Tuning the work function of ultrathin oxide films on metals by adsorption of alkali atoms," *J. Chem. Phys.*, vol. 128, no. 16, p. 164707, Apr. 2008, doi: 10.1063/1.2905218.

[77] T. König, G. H. Simon, H.-P. Rust, and M. Heyde, "Work function measurements of thin oxide films on metals—MgO on Ag(001)," *J. Phys. Chem. C*, vol. 113, no. 26, pp. 11301–11305, Jul. 2009, doi: 10.1021/jp901226q.

[78] G. Wang, P. Yang, N. A. Moody, and E. R. Batista, "Overcoming the quantum efficiency-lifetime tradeoff of photocathodes by coating with atomically thin two-dimensional nanomaterials," *npj 2D Mater. Appl.*, vol. 2, no. 1, Art. no. 1, Jun. 2018, doi: 10.1038/s41699-018-0062-6.

[79] Y. Zhou and P. Zhang, "Theory of field emission from dielectric coated surfaces," *Phys. Rev. Research*, vol. 2, no. 4, p. 043439, Dec. 2020, doi: 10.1103/PhysRevResearch.2.043439.

[80] K. J. Betsch, D. W. Pinkham, and R. R. Jones, "Directional emission of multiply charged ions during dissociative ionization in asymmetric two-color laser fields," *Phys. Rev. Lett.*, vol. 105, no. 22, p. 223002, Nov. 2010, doi: 10.1103/PhysRevLett.105.223002.

[81] D. Shafir *et al.*, "Resolving the time when an electron exits a tunnelling barrier," *Nature*, vol. 485, no. 7398, Art. no. 7398, May 2012, doi: 10.1038/nature11025.

[82] K. T. Kim *et al.*, "Manipulation of quantum paths for space–time characterization of attosecond pulses," *Nat. Phys.*, vol. 9, no. 3, Art. no. 3, Mar. 2013, doi: 10.1038/nphys2525.

[83] P. G. de A. Martín, A. C. L. Fontaine, C. Köhler, and L. Bergé, "Effects of multiple ionization in atomic gases irradiated by one- and two-color ultrashort pulses," *J. Phys. B: At. Mol. Opt. Phys.*, vol. 48, no. 9, p. 094010, Apr. 2015, doi: 10.1088/0953-4075/48/9/094010.

[84] M. Förster *et al.*, "Two-color coherent control of femtosecond above-threshold photoemission from a Tungsten nanotip," *Phys. Rev. Lett.*, vol. 117, no. 21, p. 217601, Nov. 2016, doi: 10.1103/PhysRevLett.117.217601.

[85] T. Paschen *et al.*, "High visibility in two-color above-threshold photoemission from tungsten nanotips in a coherent control scheme," *J. Mod. Opt.*, vol. 64, no. 10–11, pp. 1054–1060, Jun. 2017, doi: 10.1080/09500340.2017.1281453.

[86] P. Dienstbier, T. Paschen, and P. Hommelhoff, “Two-color coherent control in photoemission from gold needle tips,” *J. Phys. B: At. Mol. Opt. Phys.*, vol. 54, no. 13, p. 134002, Jul. 2021, doi: 10.1088/1361-6455/ac0294.

[87] A. Li, Y. Pan, P. Dienstbier, and P. Hommelhoff, “Quantum Interference Visibility Spectroscopy in Two-Color Photoemission from Tungsten Needle Tips,” *Phys. Rev. Lett.*, vol. 126, no. 13, p. 137403, Apr. 2021, doi: 10.1103/PhysRevLett.126.137403.

[88] P. Dienstbier, T. Paschen, and P. Hommelhoff, “Coherent control at gold needle tips approaching the strong-field regime,” *Nanophotonics*, Jul. 2021, doi: 10.1515/nanoph-2021-0242.

[89] B. Ji *et al.*, “Two-color multiphoton emission for comprehensive reveal of ultrafast plasmonic field distribution,” *New J. Phys.*, vol. 20, no. 7, p. 073031, Jul. 2018, doi: 10.1088/1367-2630/aad145.

[90] Y. Li *et al.*, “Coherent Interference Fringes of Two-Photon Photoluminescence in Individual Au Nanoparticles: The Critical Role of the Intermediate State,” *Phys. Rev. Lett.*, vol. 127, no. 7, p. 073902, Aug. 2021, doi: 10.1103/PhysRevLett.127.073902.

[91] Y. Luo and P. Zhang, “Ultrafast strong-field photoelectron emission due to two-color laser fields,” *Phys. Rev. B*, vol. 98, no. 16, p. 165442, Oct. 2018, doi: 10.1103/PhysRevB.98.165442.

[92] Y. Luo and P. Zhang, “Analysis of two-color laser-induced electron emission from a biased metal surface using an exact quantum mechanical solution,” *Phys. Rev. Applied*, vol. 12, no. 4, p. 044056, Oct. 2019, doi: 10.1103/PhysRevApplied.12.044056.

[93] Y. Luo, J. Luginsland, and P. Zhang, “Interference modulation of photoemission from biased metal cathodes driven by two lasers of the same frequency,” *AIP Adv.*, vol. 10, no. 7, p. 075301, Jul. 2020, doi: 10.1063/5.0010792.

[94] L. A. Lompre, J. Thebault, and G. Farkas, “Intensity and polarization effects of a single 30-psec laser pulse on five-photon surface photoeffect of gold,” *Appl. Phys. Lett.*, vol. 27, no. 3, pp. 110–112, Aug. 1975, doi: 10.1063/1.88399.

[95] G. Wachter, C. Lemell, J. Burgdörfer, M. Schenk, M. Krüger, and P. Hommelhoff, “Electron rescattering at metal nanotips induced by ultrashort laser pulses,” *Phys. Rev. B*, vol. 86, no. 3, p. 035402, Jul. 2012, doi: 10.1103/PhysRevB.86.035402.

[96] G. G. Paulus, W. Nicklich, H. Xu, P. Lambropoulos, and H. Walther, “Plateau in above threshold ionization spectra,” *Phys. Rev. Lett.*, vol. 72, no. 18, pp. 2851–2854, May 1994, doi: 10.1103/PhysRevLett.72.2851.

[97] R. H. Fowler and L. Nordheim, “Electron emission in intense electric fields,” *Proc. R. Soc. A: Math. Phys. Eng. Sci*, vol. 119, no. 781, pp. 173–181, May 1928, doi: 10.1098/rspa.1928.0091.

[98] A. Modinos, “Theoretical analysis of field emission data,” *Solid-State Electronics*, vol. 45, no. 6, pp. 809–816, Jun. 2001, doi: 10.1016/S0038-1101(00)00218-5.

[99] R. G. Forbes, “Field emission: New theory for the derivation of emission area from a Fowler–Nordheim plot,” *J. Vac. Sci. Technol. B: Microelectron Nanometer Struct. Process. Meas. Phenom.*, vol. 17, no. 2, pp. 526–533, Mar. 1999, doi: 10.1116/1.590588.

[100] C. Ropers, D. R. Solli, C. P. Schulz, C. Lienau, and T. Elsaesser, “Localized multiphoton emission of femtosecond electron pulses from metal nanotips,” *Phys. Rev. Lett.*, vol. 98, no. 4, p. 043907, Jan. 2007, doi: 10.1103/PhysRevLett.98.043907.

[101] R. Bormann, M. Gulde, A. Weismann, S. V. Yalunin, and C. Ropers, “Tip-enhanced strong-field photoemission,” *Phys. Rev. Lett.*, vol. 105, no. 14, p. 147601, Sep. 2010, doi: 10.1103/PhysRevLett.105.147601.

[102] P. D. Keathley *et al.*, “Vanishing carrier-envelope-phase-sensitive response in optical-field photoemission from plasmonic nanoantennas,” *Nat. Phys.*, vol. 15, no. 11, Art. no. 11, Nov. 2019, doi: 10.1038/s41567-019-0613-6.

[103] J. H. Bechtel and P. A. Franken, “Laser-induced electron emission,” *Phys. Rev. B*, vol. 11, no. 4, pp. 1359–1364, Feb. 1975, doi: 10.1103/PhysRevB.11.1359.

[104] L. V. Keldysh, “Ionization in the field of a strong electromagnetic wave,” *Sov. Phys. JETP*, vol. 20, no. 5, pp. 1307–1314, May 1965.

[105]A. M. Zheltikov, “Keldysh parameter, photoionization adiabaticity, and the tunneling time,” *Phys. Rev. A*, vol. 94, no. 4, p. 043412, Oct. 2016, doi: 10.1103/PhysRevA.94.043412.

[106] K. L. Jensen, *Introduction to the Physics of Electron Emission*. John Wiley & Sons, 2017.

[107] R. J. England *et al.*, “Dielectric laser accelerators,” *Rev. Mod. Phys.*, vol. 86, no. 4, pp. 1337–1389, Dec. 2014, doi: 10.1103/RevModPhys.86.1337.

[108] M. Gulde *et al.*, “Ultrafast low-energy electron diffraction in transmission resolves polymer/graphene superstructure dynamics,” *Science*, vol. 345, no. 6193, pp. 200–204, Jul. 2014, doi: 10.1126/science.1250658.

[109] J. Lin, P. Y. Wong, P. Yang, Y. Y. Lau, W. Tang, and P. Zhang, “Electric field distribution and current emission in a miniaturized geometrical diode,” *J. Appl. Phys.*, vol. 121, no. 24, p. 244301, Jun. 2017, doi: 10.1063/1.4987127.

[110] R. H. Fowler, “The analysis of photoelectric sensitivity curves for clean metals at various temperatures,” *Phys. Rev.*, vol. 38, no. 1, pp. 45–56, Jul. 1931, doi: 10.1103/PhysRev.38.45.

[111]L. A. DuBridge, “A further experimental test of Fowler’s theory of photoelectric emission,” *Phys. Rev.*, vol. 39, no. 1, pp. 108–118, Jan. 1932, doi: 10.1103/PhysRev.39.108.

[112] L. A. DuBridge, “Theory of the energy distribution of photoelectrons,” *Phys. Rev.*, vol. 43, no. 9, pp. 727–741, May 1933, doi: 10.1103/PhysRev.43.727.

[113] J. H. Bechtel, W. L. Smith, and N. Bloembergen, “Four-photon photoemission from tungsten,” *Opt. Commun.*, vol. 13, no. 1, pp. 56–59, Jan. 1975, doi: 10.1016/0030-4018(75)90156-X.

[114] W. E. Spicer, “Photoemissive, photoconductive, and optical absorption studies of alkali-Antimony compounds,” *Phys. Rev.*, vol. 112, no. 1, pp. 114–122, Oct. 1958, doi: 10.1103/PhysRev.112.114.

[115] C. N. Berglund and W. E. Spicer, “Photoemission studies of Copper and Silver: theory,” *Phys. Rev.*, vol. 136, no. 4A, pp. A1030–A1044, Nov. 1964, doi: 10.1103/PhysRev.136.A1030.

[116] W. F. Krolikowski and W. E. Spicer, “Photoemission studies of the noble metals. I. Copper,” *Phys. Rev.*, vol. 185, no. 3, pp. 882–900, Sep. 1969, doi: 10.1103/PhysRev.185.882.

[117] W. F. Krolikowski and W. E. Spicer, “Photoemission studies of the noble metals. II. Gold,” *Phys. Rev. B*, vol. 1, no. 2, pp. 478–487, Jan. 1970, doi: 10.1103/PhysRevB.1.478.

[118] W. P. Putnam, R. G. Hobbs, P. D. Keathley, K. K. Berggren, and F. X. Kärtner, “Optical-field-controlled photoemission from plasmonic nanoparticles,” *Nat. Phys.*, vol. 13, no. 4, Art. no. 4, Apr. 2017, doi: 10.1038/nphys3978.

[119] S. V. Yalunin, M. Gulde, and C. Ropers, “Strong-field photoemission from surfaces: Theoretical approaches,” *Phys. Rev. B*, vol. 84, no. 19, p. 195426, Nov. 2011, doi: 10.1103/PhysRevB.84.195426.

[120] M. Pant and L. K. Ang, “Ultrafast laser-induced electron emission from multiphoton to optical tunneling,” *Phys. Rev. B*, vol. 86, no. 4, p. 045423, Jul. 2012, doi: 10.1103/PhysRevB.86.045423.

[121] W. S. Truscott, “Wave functions in the presence of a time-dependent field: Exact solutions and their application to tunneling,” *Phys. Rev. Lett.*, vol. 70, no. 13, pp. 1900–1903, Mar. 1993, doi: 10.1103/PhysRevLett.70.1900.

[122] J. G. Simmons, “Generalized formula for the electric tunnel effect between similar electrodes separated by a thin insulating film,” *J. Appl. Phys.*, vol. 34, no. 6, pp. 1793–1803, Jun. 1963, doi: 10.1063/1.1702682.

[123] P. Zhang, “Scaling for quantum tunneling current in nano- and subnano-scale plasmonic junctions,” *Sci. Rep.*, vol. 5, no. 1, Art. no. 1, May 2015, doi: 10.1038/srep09826.

[124] S. Banerjee and P. Zhang, “A generalized self-consistent model for quantum tunneling current in dissimilar metal-insulator-metal junction,” *AIP Adv.*, vol. 9, no. 8, p. 085302, Aug. 2019, doi: 10.1063/1.5116204.

[125] Y. Zhou and P. Zhang, “A quantum model for photoemission from metal surfaces and its comparison with the three-step model and Fowler–DuBridge model,” *J. Appl. Phys.*, vol. 127, no. 16, p. 164903, Apr. 2020, doi: 10.1063/5.0004140.

[126] K. L. Jensen *et al.*, “Multiple scattering effects on quantum efficiency and response time for cesiated metal photocathodes,” *J. Appl. Phys.*, vol. 110, no. 3, p. 034504, Aug. 2011, doi: 10.1063/1.3610397.

[127] P. L. E. M. Pasmans, D. C. van Vugt, J. P. van Lieshout, G. J. H. Brussaard, and O. J. Luiten, “Extreme regimes of femtosecond photoemission from a copper cathode in a dc electron gun,” *Phys. Rev. Accel. Beams*, vol. 19, no. 10, p. 103403, Oct. 2016, doi: 10.1103/PhysRevAccelBeams.19.103403.

[128] S. Ramo, J. R. Whinnery, and T. Van Duzer, *Fields and waves in communication electronics*, Third edition. New York: Weiley.

[129] P. Zhang, Y. Y. Lau, and R. M. Gilgenbach, “Analysis of radio-frequency absorption and electric and magnetic field enhancements due to surface roughness,” *J. Appl. Phys.*, vol. 105, no. 11, p. 114908, Jun. 2009, doi: 10.1063/1.3131844.

[130] C. Pérez-Arancibia, P. Zhang, O. P. Bruno, and Y. Y. Lau, “Electromagnetic power absorption due to bumps and trenches on flat surfaces,” *J. Appl. Phys.*, vol. 116, no. 12, p. 124904, Sep. 2014, doi: 10.1063/1.4896361.

[131] A. D. Gladun and P. P. Barashev, “The multiquantum photoemissive effect,” *Sov. Phys. Usp.*, vol. 12, no. 4, p. 490, Apr. 1970, doi: 10.1070/PU1970v012n04ABEH003904.

[132] J. P. Girardeau-Montaut and C. Girardeau-Montaut, “Theory of ultrashort nonlinear multiphoton photoelectric emission from metals,” *Phys. Rev. B*, vol. 51, no. 19, pp. 13560–13567, May 1995, doi: 10.1103/PhysRevB.51.13560.

[133] J. G. Fujimoto, J. M. Liu, E. P. Ippen, and N. Bloembergen, “Femtosecond laser interaction with metallic tungsten and nonequilibrium electron and lattice temperatures,” *Phys. Rev. Lett.*, vol. 53, no. 19, pp. 1837–1840, Nov. 1984, doi: 10.1103/PhysRevLett.53.1837.

[134] J.-P. Girardeau-Montaut, M. Afif, C. Tomas, A.-F. Obaton, C. Girardeau-Montaut, and K. Warda, “Ultrafast photoelectric emission from new solid materials,” *Appl. Surf. Sci.*, vol. 106, pp. 451–456, Oct. 1996, doi: 10.1016/S0169-4332(96)00417-5.

[135] W. S. Fann, R. Storz, H. W. K. Tom, and J. Bokor, “Direct measurement of nonequilibrium electron-energy distributions in subpicosecond laser-heated gold films,” *Phys. Rev. Lett.*, vol. 68, no. 18, pp. 2834–2837, May 1992, doi: 10.1103/PhysRevLett.68.2834.

[136] J. Maxson, P. Musumeci, L. Cultrera, S. Karkare, and H. Padmore, “Ultrafast laser pulse heating of metallic photocathodes and its contribution to intrinsic emittance,” *Nucl. Instrum. Methods Phys. Res. A: Accel. Spectrom. Detect. Assoc. Equip.*, vol. 865, pp. 99–104, Sep. 2017, doi: 10.1016/j.nima.2016.08.032.

[137] Y. Zhang and J. K. Chen, “Melting and resolidification of gold film irradiated by nano- to femtosecond lasers,” *Appl. Phys. A*, vol. 88, no. 2, pp. 289–297, Aug. 2007, doi: 10.1007/s00339-007-4016-7.

[138] D. Novko, V. Despoja, M. Reutzel, A. Li, H. Petek, and B. Gumhalter, “Plasmonically assisted channels of photoemission from metals,” *Phys. Rev. B*, vol. 103, no. 20, p. 205401, May 2021, doi: 10.1103/PhysRevB.103.205401.

[139] B. Barwick, C. Corder, J. Strohaber, N. Chandler-Smith, C. Uiterwaal, and H. Batelaan, “Laser-induced ultrafast electron emission from a field emission tip,” *New J. Phys.*, vol. 9, no. 5, pp. 142–142, May 2007, doi: 10.1088/1367-2630/9/5/142.

[140] M. R. Bionta, S. J. Weber, I. Blum, J. Mauchain, B. Chatel, and B. Chalopin, “Wavelength and shape dependent strong-field photoemission from silver nanotips,” *New J. Phys.*, vol. 18, no. 10, p. 103010, Oct. 2016, doi: 10.1088/1367-2630/18/10/103010.

[141] J. H. Bechtel, W. Lee Smith, and N. Bloembergen, “Two-photon photoemission from metals induced by picosecond laser pulses,” *Phys. Rev. B*, vol. 15, no. 10, pp. 4557–4563, May 1977, doi: 10.1103/PhysRevB.15.4557.

[142] G. Ferrini, F. Banfi, C. Giannetti, and F. Parmigiani, “Non-linear electron photoemission from metals with ultrashort pulses,” *Nucl. Instrum. Methods Phys. Res. A: Accel. Spectrom. Detect. Assoc. Equip.*, vol. 601, no. 1, pp. 123–131, Mar. 2009, doi: 10.1016/j.nima.2008.12.107.

[143] W. Wendelen, B. Y. Mueller, D. Autrique, B. Rethfeld, and A. Bogaerts, “Space charge corrected electron emission from an aluminum surface under non-equilibrium conditions,” *J. Appl. Phys.*, vol. 111, no. 11, p. 113110, Jun. 2012, doi: 10.1063/1.4729071.

[144] W. Wendelen, D. Autrique, and A. Bogaerts, “Space charge limited electron emission from a Cu surface under ultrashort pulsed laser irradiation,” *Appl. Phys. Lett.*, vol. 96, no. 5, p. 051121, Feb. 2010, doi: 10.1063/1.3292581.

[145] K. L. Jensen, D. W. Feldman, N. A. Moody, and P. G. O’Shea, “A photoemission model for low work function coated metal surfaces and its experimental validation,” *J. Appl. Phys.*, vol. 99, no. 12, p. 124905, Jun. 2006, doi: 10.1063/1.2203720.

[146] R. H. M. Groeneveld, R. Sprik, and A. Lagendijk, “Femtosecond spectroscopy of electron-electron and electron-phonon energy relaxation in Ag and Au,” *Phys. Rev. B*, vol. 51, no. 17, pp. 11433–11445, May 1995, doi: 10.1103/PhysRevB.51.11433.

[147] J. Hohlfeld, S.-S. Wellershoff, J. Güdde, U. Conrad, V. Jähnke, and E. Matthias, “Electron and lattice dynamics following optical excitation of metals,” *Chem. Phys.*, vol. 251, no. 1, pp. 237–258, Jan. 2000, doi: 10.1016/S0301-0104(99)00330-4.

[148] S. Tsujino *et al.*, “Ultrafast electron emission from metallic nanotip arrays induced by near infrared femtosecond laser pulses,” *Appl. Phys. Lett.*, vol. 92, no. 19, p. 193501, May 2008, doi: 10.1063/1.2924290.

[149] K. Vestentoft and P. Balling, “Formation of an extended nanostructured metal surface by ultra-short laser pulses: single-pulse ablation in the high-fluence limit,” *Appl. Phys. A*, vol. 84, no. 1, pp. 207–213, Jul. 2006, doi: 10.1007/s00339-006-3602-4.

[150] F. H. M. Faisal, J. Z. Kamiński, and E. Saczuk, “Photoemission and high-order harmonic generation from solid surfaces in intense laser fields,” *Phys. Rev. A*, vol. 72, no. 2, p. 023412, Aug. 2005, doi: 10.1103/PhysRevA.72.023412.

[151] L. K. Ang and M. Pant, “Generalized model for ultrafast laser induced electron emission from a metal tip,” *Phys. Plasmas*, vol. 20, no. 5, p. 056705, May 2013, doi: 10.1063/1.4803086.

[152] P. B. Johnson and R. W. Christy, “Optical constants of the noble metals,” *Phys. Rev. B*, vol. 6, no. 12, pp. 4370–4379, Dec. 1972, doi: 10.1103/PhysRevB.6.4370.

[153] Y. Zhou and P. Zhang, “Quantum efficiency of photoemission from biased metal surfaces with laser wavelengths from UV to NIR,” *J. Appl. Phys.*, vol. 130, no. 6, p. 064902, Aug. 2021, doi: 10.1063/5.0059497.

[154] H. Yanagisawa *et al.*, “Energy distribution curves of ultrafast laser-induced field emission and their implications for electron dynamics,” *Phys. Rev. Lett.*, vol. 107, no. 8, p. 087601, Aug. 2011, doi: 10.1103/PhysRevLett.107.087601.

[155] Q. H. Wang, A. A. Setlur, J. M. Lauerhaas, J. Y. Dai, E. W. Seelig, and R. P. H. Chang, “A nanotube-based field-emission flat panel display,” *Appl. Phys. Lett.*, vol. 72, no. 22, pp. 2912–2913, May 1998, doi: 10.1063/1.121493.

[156] A. A. Talin, K. A. Dean, and J. E. Jaskie, “Field emission displays: a critical review,” *Solid-State Electronics*, vol. 45, no. 6, pp. 963–976, Jun. 2001, doi: 10.1016/S0038-1101(00)00279-3.

[157] Y. Saito, K. Hata, A. Takakura, J. Yotani, and S. Uemura, “Field emission of carbon nanotubes and its application as electron sources of ultra-high luminance light-source devices,” *Phys. B: Condens. Matter*, vol. 323, no. 1, pp. 30–37, Oct. 2002, doi: 10.1016/S0921-4526(02)00961-4.

[158] L. W. Swanson and G. A. Schwind, “A review of field electron source use in electron microscopes,” *Microsc. Microanal.*, vol. 11, no. S02, pp. 864–865, Aug. 2005, doi: 10.1017/S1431927605503854.

[159] F. Houdellier *et al.*, “Development of TEM and SEM high brightness electron guns using cold-field emission from a carbon nanotip,” *Ultramicroscopy*, vol. 151, pp. 107–115, Apr. 2015, doi: 10.1016/j.ultramic.2014.11.021.

[160] G. N. Fursey, “Field emission in vacuum micro-electronics,” *Appl. Surf. Sci.*, vol. 215, no. 1, pp. 113–134, Jun. 2003, doi: 10.1016/S0169-4332(03)00315-5.

[161] E. J. Radauscher *et al.*, “Improved performance of field emission vacuum microelectronic devices for integrated circuits,” *IEEE Trans. Electron Devices*, vol. 63, no. 9, pp. 3753–3760, Sep. 2016, doi: 10.1109/TED.2016.2593905.

[162] A. Evtukh, H. Hartnagel, O. Yilmazoglu, H. Mimura, and D. Pavlidis, *Vacuum nanoelectronic devices: novel electron sources and applications*. John Wiley & Sons, 2015.

[163] J.-W. Han, D.-I. Moon, and M. Meyyappan, “Nanoscale Vacuum Channel Transistor,” *Nano Lett.*, vol. 17, no. 4, pp. 2146–2151, Apr. 2017, doi: 10.1021/acs.nanolett.6b04363.

[164] G. Cao *et al.*, “A dynamic micro-CT scanner based on a carbon nanotube field emission x-ray source,” *Phys. Med. Biol.*, vol. 54, no. 8, pp. 2323–2340, Mar. 2009, doi: 10.1088/0031-9155/54/8/005.

[165] K. L. Jensen, “Field emitter arrays for plasma and microwave source applications,” *Phys. Plasmas*, vol. 6, no. 5, pp. 2241–2253, Apr. 1999, doi: 10.1063/1.873502.

[166] D. Shiffler, T. K. Statom, T. W. Hussey, O. Zhou, and P. Mardahl, “High-power microwave sources,” *Modern Microwave and Millimeter-Wave Power Electronics*, pp. 691–730, 2005.

[167] D. Shiffler *et al.*, “Emission uniformity and emission area of explosive field emission cathodes,” *Appl. Phys. Lett.*, vol. 79, no. 18, pp. 2871–2873, Oct. 2001, doi: 10.1063/1.1415408.

[168] W. Tang, D. Shiffler, K. Golby, M. LaCour, and T. Knowles, “Field enhancement for fiber emitters in linear and rectangular arrays,” *J. Vac. Sci. Technol. B*, vol. 32, no. 5, p. 052202, Sep. 2014, doi: 10.1116/1.4891928.

[169] P. Zhang, S. B. Fairchild, T. C. Back, and Y. Luo, “Field emission from carbon nanotube fibers in varying anode-cathode gap with the consideration of contact resistance,” *AIP Adv.*, vol. 7, no. 12, p. 125203, Dec. 2017, doi: 10.1063/1.5008995.

[170] P. Zhang *et al.*, “Temperature comparison of looped and vertical Carbon Nanotube Fibers during field emission,” *Appl. Sci.*, vol. 8, no. 7, Art. no. 7, Jul. 2018, doi: 10.3390/app8071175.

[171] S. B. Fairchild *et al.*, “Carbon nanotube fiber field emission array cathodes,” *IEEE Trans. Plasma Sci.*, vol. 47, no. 5, pp. 2032–2038, May 2019, doi: 10.1109/TPS.2019.2900219.

[172] P. Wong, P. Zhang, and J. Luginsland, “Recent theory of traveling-wave tubes: a tutorial-review,” *Plasma Res. Express*, vol. 2, no. 2, p. 023001, Jun. 2020, doi: 10.1088/2516-1067/ab9730.

[173] J.-M. Bonard, J.-P. Salvetat, T. Stöckli, L. Forró, and A. Châtelain, “Field emission from carbon nanotubes: perspectives for applications and clues to the emission mechanism,” *Appl. Phys. A*, vol. 69, no. 3, pp. 245–254, Sep. 1999, doi: 10.1007/s003390050998.

[174] S. Yamamoto, “Fundamental physics of vacuum electron sources,” *Rep. Prog. Phys.*, vol. 69, no. 1, pp. 181–232, Nov. 2005, doi: 10.1088/0034-4885/69/1/R04.

[175] L. W. Swanson and G. A. Schwind, “Chapter 2 A Review of the Cold-Field Electron Cathode,” in *Advances in Imaging and Electron Physics*, vol. 159, Elsevier, 2009, pp. 63–100. doi: 10.1016/S1076-5670(09)59002-7.

[176] X. Shao, A. Srinivasan, W. K. Ang, and A. Khursheed, “A high-brightness large-diameter graphene coated point cathode field emission electron source,” *Nat. Commun.*, vol. 9, no. 1, p. 1288, Dec. 2018, doi: 10.1038/s41467-018-03721-y.

[177] D. Ye, S. Moussa, J. D. Ferguson, A. A. Baski, and M. S. El-Shall, “Highly efficient electron field emission from graphene oxide sheets supported by Nickel nanotip arrays,” *Nano Lett.*, vol. 12, no. 3, pp. 1265–1268, Mar. 2012, doi: 10.1021/nl203742s.

[178] A. T. T. Koh, Y. M. Foong, Z. Yusop, M. Tanemura, and D. H. C. Chua, “Low temperature direct of graphene onto metal nano-spindt tip with applications in electron emission,” *Adv. Mater. Interfaces*, vol. 1, no. 5, p. 1300147, 2014, doi: 10.1002/admi.201300147.

[179] C. Henkel *et al.*, “Resonant tunneling induced enhancement of electron field emission by ultra-thin coatings,” *Sci. Rep.*, vol. 9, no. 1, Art. no. 1, May 2019, doi: 10.1038/s41598-019-43149-y.

[180] L. W. Swanson and R. W. Strayer, “Field-electron-microscopy studies of Cesium layers on various refractory metals: work function change,” *J. Chem. Phys.*, vol. 48, no. 6, pp. 2421–2442, Mar. 1968, doi: 10.1063/1.1669464.

[181] S. B. Fairchild, T. C. Back, P. T. Murray, M. M. Cahay, and D. A. Shiffler, “Low work function CsI coatings for enhanced field emission properties,” *J. Vac. Sci. Technol. A*, vol. 29, no. 3, p. 031402, Apr. 2011, doi: 10.1116/1.3581058.

[182] M. Morita and T. Ohmi, “Characterization and control of native oxide on silicon,” *Jpn. J. Appl. Phys.*, vol. 33, no. 1S, p. 370, Jan. 1994, doi: 10.1143/JJAP.33.370.

[183] Q. Huang, “Instability of field emission from silicon covered with a thin oxide due to electron trapping,” *J. Appl. Phys.*, vol. 79, no. 7, pp. 3703–3707, Apr. 1996, doi: 10.1063/1.361202.

[184] P. D. Keathley, A. Sell, W. P. Putnam, S. Guerrera, L. Velásquez-García, and F. X. Kärtner, “Strong-field photoemission from silicon field emitter arrays,” *Ann. Phys. (Berlin)*, vol. 525, no. 1–2, pp. 144–150, 2013, doi: 10.1002/andp.201200189.

[185] W. W. Lui and M. Fukuma, “Exact solution of the Schrodinger equation across an arbitrary one-dimensional piecewise-linear potential barrier,” *J. Appl. Phys.*, vol. 60, no. 5, pp. 1555–1559, Sep. 1986, doi: 10.1063/1.337788.

[186] K. F. Brennan and C. J. Summers, “Theory of resonant tunneling in a variably spaced multiquantum well structure: An Airy function approach,” *J. Appl. Phys.*, vol. 61, no. 2, pp. 614–623, Jan. 1987, doi: 10.1063/1.338213.

[187] P. Zhang and T. Pan, “Exact analytical theory for inverse tunneling of free vacuum electrons into a solid,” *AIP Adv.*, vol. 7, no. 6, p. 065307, Jun. 2017, doi: 10.1063/1.4986220.

[188] K. L. Jensen *et al.*, “A photoemission moments model using density functional and transfer matrix methods applied to coating layers on surfaces: Theory,” *J. Appl. Phys.*, vol. 123, no. 4, p. 045301, Jan. 2018, doi: 10.1063/1.5008600.

[189] J. Maserjian and N. Zamani, “Behavior of the Si/SiO2 interface observed by Fowler-Nordheim tunneling,” *J. Appl. Phys.*, vol. 53, no. 1, pp. 559–567, Jan. 1982, doi: 10.1063/1.329919.

[190] L. L. Chang, L. Esaki, and R. Tsu, “Resonant tunneling in semiconductor double barriers,” *Appl. Phys. Lett.*, vol. 24, no. 12, pp. 593–595, Jun. 1974, doi: 10.1063/1.1655067.

[191] X. Tan, P. Rumbach, N. Griggs, K. L. Jensen, and D. B. Go, “Theoretical analysis of 1D resonant tunneling behavior in ion-enhanced cold field and thermo-field emission,” *J. Appl. Phys.*, vol. 120, no. 21, p. 213301, Dec. 2016, doi: 10.1063/1.4971263.

[192] R.-Z. Wang, W. Zhao, and H. Yan, “Generalized mechanism of field emission from nanostructured semiconductor film cathodes,” *Sci. Rep.*, vol. 7, Mar. 2017, doi: 10.1038/srep43625.

[193] J. W. Gadzuk and E. W. Plummer, “Field emission energy distribution (FEED),” *Rev. Mod. Phys.*, vol. 45, no. 3, pp. 487–548, Jul. 1973, doi: 10.1103/RevModPhys.45.487.

[194] N. A. Moody, K. L. Jensen, D. W. Feldman, E. J. Montgomery, and P. G. O’Shea, “Factors affecting performance of dispenser photocathodes,” *J. Appl. Phys.*, vol. 102, no. 10, p. 104901, Nov. 2007, doi: 10.1063/1.2805653.

[195] X. Xiong, J.-B. You, P. Bai, C. E. Png, Z.-K. Zhou, and L. Wu, “Ultrastrong coupling in single plexcitonic nanocubes,” *Nanophotonics*, vol. 9, no. 2, pp. 257–266, Feb. 2020, doi: 10.1515/nanoph-2019-0333.

[196] M. Hentschel, L. Wu, M. Schäferling, P. Bai, E. P. Li, and H. Giessen, “Optical properties of chiral three-dimensional plasmonic oligomers at the onset of charge-transfer plasmons,” *ACS Nano*, vol. 6, no. 11, pp. 10355–10365, Nov. 2012, doi: 10.1021/nn304283y.

[197] L. Wu, H. Duan, P. Bai, M. Bosman, J. K. W. Yang, and E. Li, “Fowler–Nordheim tunneling induced charge transfer plasmons between nearly touching nanoparticles,” *ACS Nano*, vol. 7, no. 1, pp. 707–716, Jan. 2013, doi: 10.1021/nn304970v.

[198] Y. Huang, L. Wu, X. Chen, P. Bai, and D.-H. Kim, “Synthesis of anisotropic concave Gold nanocuboids with distinctive plasmonic properties,” *Chem. Mater.*, vol. 25, no. 12, pp. 2470–2475, Jun. 2013, doi: 10.1021/cm400765b.

[199] T. J. Davis, D. E. Gómez, and A. Roberts, “Plasmonic circuits for manipulating optical information,” *Nanophotonics*, vol. 6, no. 3, pp. 543–559, May 2017, doi: 10.1515/nanoph-2016-0131.

[200] D. Bohm, *Quantum theory*. Courier Corporation, 2012.

[201] J. Binney and D. Skinner, *The physics of quantum mechanics*. Oxford University Press, 2013.

[202] V. W. Ballarotto, M. Breban, K. Siegrist, R. J. Phaneuf, and E. D. Williams, "Photoelectron emission microscopy of ultrathin oxide covered devices," *J. Vac. Sci. Technol. B: Microelectron Nanometer Struct. Process. Meas. Phenom.*, vol. 20, no. 6, pp. 2514–2518, Nov. 2002, doi: 10.1116/1.1525007.

[203] Q. Huang, "Field emission from a silicon surface potential well through a thin oxide," *J. Appl. Phys.*, vol. 78, no. 11, pp. 6770–6774, Dec. 1995, doi: 10.1063/1.360501.

[204] X. Xie *et al.*, "Attosecond probe of valence-electron wave packets by subcycle sculpted laser fields," *Phys. Rev. Lett.*, vol. 108, no. 19, p. 193004, May 2012, doi: 10.1103/PhysRevLett.108.193004.

[205] V. Gruson *et al.*, "Attosecond dynamics through a Fano resonance: Monitoring the birth of a photoelectron," *Science*, vol. 354, no. 6313, pp. 734–738, Nov. 2016, doi: 10.1126/science.aah5188.

[206] S. K. Cushing, "Plasmonic hot carriers skip out in femtoseconds," *Nat. Photonics*, vol. 11, no. 12, pp. 748–749, Dec. 2017, doi: 10.1038/s41566-017-0059-2.

[207] Y. Luo and P. Zhang, "Ultrafast optical-field-induced photoelectron emission in a vacuum nanoscale gap: An exact analytical formulation," *Appl. Phys. Lett.*, vol. 119, no. 19, p. 194101, Nov. 2021, doi: 10.1063/5.0061914.

[208] A. G. Joly, P. Z. El-Khoury, and W. P. Hess, "Spatiotemporal imaging of surface plasmons using two-color photoemission electron microscopy," *J. Phys. Chem. C*, vol. 122, no. 36, pp. 20981–20988, Sep. 2018, doi: 10.1021/acs.jpcc.8b05849.

[209] Z. Zhao *et al.*, "Distinct spatiotemporal imaging of femtosecond surface plasmon polaritons assisted with the opening of the two-color quantum pathway effect," *Opt. Express*, vol. 28, no. 13, pp. 19023–19033, Jun. 2020, doi: 10.1364/OE.397526.

[210] T. Paschen, C. Nauk, P. Dienstbier, and P. Hommelhoff, "Strong-field spectra and optical near-field enhancement at aluminium needle tips," *J. Phys. B: At. Mol. Opt. Phys.*, vol. 54, no. 14, p. 144006, Jul. 2021, doi: 10.1088/1361-6455/ac13ff.

[211] J. Tan *et al.*, "Determination of the ionization time using attosecond photoelectron interferometry," *Phys. Rev. Lett.*, vol. 121, no. 25, p. 253203, Dec. 2018, doi: 10.1103/PhysRevLett.121.253203.

[212] C. Pellegrini, "X-ray free-electron lasers: from dreams to reality," *Phys. Scr.*, vol. T169, p. 014004, Dec. 2016, doi: 10.1088/1402-4896/aa5281.

[213] P. Lang *et al.*, "Ultrafast switching of photoemission electron through quantum pathways interference in metallic nanostructure," *Opt. Lett.*, vol. 43, no. 23, pp. 5721–5724, Dec. 2018, doi: 10.1364/OL.43.005721.

[214] W. Cheng-Wei Huang, M. Becker, J. Beck, and H. Batelaan, "Two-color multiphoton emission from nanotips," *New J. Phys.*, vol. 19, no. 2, p. 023011, Feb. 2017, doi: 10.1088/1367-2630/aa58bb.

[215] S. Zafar *et al.*, "Thickness and effective electron mass measurements for thin silicon dioxide films using tunneling current oscillations," *Appl. Phys. Lett.*, vol. 67, no. 7, pp. 1031–1033, Aug. 1995, doi: 10.1063/1.114720.

[216] S. O. Kasap, *Principles of electronic materials and devices*, vol. 2. McGraw-Hill New York, 2006.

[217] B. Brar, G. D. Wilk, and A. C. Seabaugh, "Direct extraction of the electron tunneling effective mass in ultrathin SiO2," *Appl. Phys. Lett.*, vol. 69, no. 18, pp. 2728–2730, Oct. 1996, doi: 10.1063/1.117692.

[218] K. P. Ghatak, S. Bhattacharya, S. K. Biswas, A. Dey, and A. K. Dasgupta, "A simple theoretical analysis of the effective electron mass in III–V, ternary and quaternary materials in the presence of light waves," *Phys. Scr.*, vol. 75, no. 6, p. 820, May 2007, doi: 10.1088/0031-8949/75/6/012.

[219] P. K. Bose *et al.*, "Influence of light waves on the effective electron mass in quantum wells, wires, inversion layers and superlattices," *Quantum Matter*, vol. 1, no. 2, pp. 89–126, Dec. 2012, doi: 10.1166/qm.2012.1009.

[220] G. Zhang, M.-B. Yu, C.-H. Tung, and G.-Q. Lo, "Quantum size effects on dielectric constants and optical absorption of ultrathin Silicon films," *IEEE Electron Device Lett.*, vol. 29, no. 12, pp. 1302–1305, Dec. 2008, doi: 10.1109/LED.2008.2005651.

[221] H. G. Yoo and P. M. Fauchet, "Dielectric constant reduction in silicon nanostructures," *Phys. Rev. B*, vol. 77, no. 11, p. 115355, Mar. 2008, doi: 10.1103/PhysRevB.77.115355.

[222] E. H. Nicollian and J. R. Brews, *MOS (Metal Oxide Semiconductor) Physics and Technology*. John Wiley & Sons, 2002.

[223] F. W. Schmidlin, "Enhanced tunneling through dielectric films due to ionic defects," *J. Appl. Phys.*, vol. 37, no. 7, pp. 2823–2832, Jun. 1966, doi: 10.1063/1.1782131.

[224] C. Chua, Y. S. Ang, and L. K. Ang, "Tunneling injection to trap-limited space-charge conduction for metal-insulator junction," *Appl. Phys. Lett.*, vol. 121, no. 19, p. 192109, Nov. 2022, doi: 10.1063/5.0124748.

[225] Y. S. Ang, Y. Chen, C. Tan, and L. K. Ang, "Generalized high-energy thermionic electron injection at graphene interface," *Phys. Rev. Applied*, vol. 12, no. 1, p. 014057, Jul. 2019, doi: 10.1103/PhysRevApplied.12.014057.

[226] P. Zhang, L. K. Ang, and A. Gover, "Enhancement of coherent Smith-Purcell radiation at terahertz frequency by optimized grating, prebunched beams, and open cavity," *Phys. Rev. ST Accel. Beams*, vol. 18, no. 2, p. 020702, Feb. 2015, doi: 10.1103/PhysRevSTAB.18.020702.

[227] M. A. Faisal and P. Zhang, "Grating optimization for Smith–Purcell radiation: direct correlation between spatial growth rate and starting current," *IEEE Trans. Electron Devices*, pp. 1–4, 2022, doi: 10.1109/TED.2022.3208846.

[228] Y. Luo and P. Zhang, "Optical-field-induced electron emission in a dc-biased nanogap," *Phys. Rev. Applied*, vol. 17, no. 4, p. 044008, Apr. 2022, doi: 10.1103/PhysRevApplied.17.044008.

[229] S. Banerjee, J. Luginsland, and P. Zhang, “A two dimensional tunneling resistance transmission line model for nanoscale parallel electrical contacts,” *Sci. Rep.*, vol. 9, no. 1, Art. no. 1, Oct. 2019, doi: 10.1038/s41598-019-50934-2.

[230] S. Banerjee, L. Cao, Y. S. Ang, L. K. Ang, and P. Zhang, “Reducing contact resistance in two-dimensional-material-based electrical contacts by roughness engineering,” *Phys. Rev. Applied*, vol. 13, no. 6, p. 064021, Jun. 2020, doi: 10.1103/PhysRevApplied.13.064021.

[231] S. Banerjee, J. Luginsland, and P. Zhang, “Interface engineering of electrical contacts,” *Phys. Rev. Applied*, vol. 15, no. 6, p. 064048, Jun. 2021, doi: 10.1103/PhysRevApplied.15.064048.

[232] S. Banerjee and P. Zhang, “Review of recent studies on nanoscale electrical junctions and contacts: Quantum tunneling, current crowding, and interface engineering,” *J. Vac. Sci. Technol. A*, vol. 40, no. 3, p. 030802, May 2022, doi: 10.1116/6.0001724.

[233] S. Banerjee and P. Zhang, “Scaling of Time-Dependent Tunneling Current in Terahertz Scanning Tunneling Microscopes,” *Phys. Rev. Applied*, vol. 18, no. 2, p. 024011, Aug. 2022, doi: 10.1103/PhysRevApplied.18.024011.

[234] M. M. El-Gomati, “A new high performance electron source for electron microscopes,” *Microsc. Microanal.*, vol. 18, no. S2, pp. 1208–1209, Jul. 2012, doi: 10.1017/S1431927612007891.